Classical and quantum ballistic-transport anomalies in microjunctions

Harold U. Baranger
AT&T Bell Laboratories 1D-230, Murray Hill, New Jersey 07974-0636

David P. DiVincenzo
IBM Research Division, Thomas J. Watson Research Center, Yorktown Heights, New York 10598

Rodolfo A. Jalabert and A. Douglas Stone
Applied Physics, Yale University, New Haven, Connecticut 06520
(Received 3 April 1991)

We have performed quantum-mechanical and classical calculations of the magnetotransport behavior of two-dimensional four-terminal junctions in the ballistic regime. Experimentally, these systems exhibit magnetotransport anomalies at small fields, suppression ("quenching") of the Hall resistance, and enhanced bend resistance, which we have reproduced with our model calculations. Because the structures are ballistic, scattering from geometric features of the junction are responsible for the anomalous transport behavior. We study several different kinds of junction (including those with soft and hard walls) and find that their Hall and bend resistances are extremely sensitive to the geometry of the junction. Analysis of our results leads to three major conclusions. (1) In all cases where quenching or inversion of the Hall resistance occurs, or where there is a large bend resistance at zero magnetic field, collimation of the injected electrons is important. Collimation means that the momentum distribution of injected electrons is weighted towards large parallel momentum due to a gradual widening of the wires near the junction. (2) The resistances obtained from the classical and quantum calculations differ substantially. First, the quantum result at zero temperature is strikingly different from the classical result because of large fluctuations caused by interference between long paths. Such effects are suppressed by temperatures of order 1 K and have been treated elsewhere. In this work we focus on the *average* quantum behavior, which we extract by two different averaging procedures. The classical and quantum results are in good *qualitative* agreement; however, we find substantial *quantitative* differences that persist well into the many-channel (classical) limit. (3) We analyze the classical results in terms of the type of electron trajectory that contributes to the Hall or bend resistance and find that the ballistic anomalies are caused by short trajectories. In particular, we find that long "scrambling" trajectories are not important in producing these anomalies. These conclusions are reinforced and illustrated by quantum calculations of local transport quantities: the charge density, the current density, and the Wigner and Husimi distributions. The collimation of the injected electrons and the importance of specific short trajectories are particularly clear in the Wigner and Husimi distributions.

I. INTRODUCTION

Transport in microstructures has been intensively investigated in the last decade.[1] Several length scales are important in defining the character of transport in these systems at low temperature: the elastic mean free path caused by impurity scattering, the Fermi wavelength controlled by the density, and the phase-coherence length—the distance over which electrons retain phase information and therefore the distance over which quantum interference effects can occur. By using the high-mobility two-dimensional electron gas formed at the interface between GaAs and $Al_xGa_{1-x}As$ as a basis for making wires, one can now make junctions between wires whose size is less than the mean free path.[1] Transport through such junctions is then ballistic. In addition, at low temperature, the phase coherence length is larger than the size of the junction which can be of order the Fermi wavelength. In this regime, then, the electrons are coherent and ballistic, and the microjunctions act like electron waveguides with a rather complex shape. Many interesting magnetoresistance effects have been observed in various structures in the ballistic regime.[1]

In this paper, we concentrate on two ballistic magnetoresistance effects which are observed in single junctions: the suppression, or "quenching," of the Hall resistance at low magnetic field and the existence of a "bend resistance" at $B=0$ which decays as the magnetic field is raised. The Hall resistance R_H for a junction is proportional to the voltage difference between the two side probes when current is passed straight through (inset to Fig. 1). R_H is, of course, produced by the Lorentz force in the junction region, and in a macroscopic sample it is linear in the magnetic field: $R_H = (1/nec)B$ in two dimensions where n is the electron density. Quenching of the Hall resistance is surprising and was not anticipated. The bend resistance R_B is proportional to the voltage difference between two adjacent probes when current flows between the two opposite adjacent probes [inset to Fig. 6(b)]. In a macroscopic Ohmic structure, two wires at-

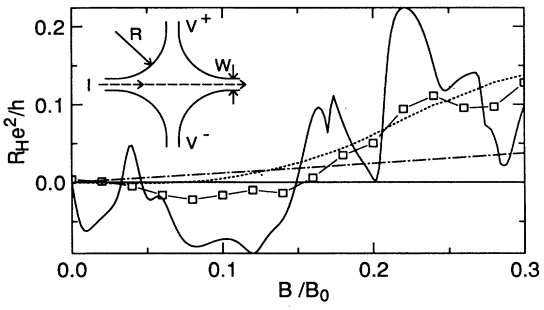

FIG. 1. Hall resistance for four-disk junction with R/W=4. The quantum calculation for a ballistic structure at T=0 (solid line for $k_F W/\pi = 3.5$) shows fluctuations not present in either the classical (dotted) or quantum square-corner junction (R/W=0, dash-dotted) cases. The quantum fluctuations are removed by a weak impurity and energy average; the resulting average quantum trace (squares) shows enhanced quenching compared to the classical result. The inset shows both the structure and the lead configuration which defines the Hall resistance. $B_0 = mcv_F/eW$.

tached to the same point on the current path measure nearly the same voltage so $R_B \approx 0$; however, we will see that in the ballistic regime, R_B can be large.

We consider several models for these two effects and, in particular, compare classical[2] and quantum[3] calculations. Typically the zero-temperature resistance fluctuates strongly as a function of either magnetic field or Fermi energy, and this necessitates the definition of an *average* resistance in order to compare to experiments at $T \sim 1$ K *even in the ballistic regime.* The classical model itself, introduced in this context by Beenakker and van Houten,[2] provides one natural definition of the average resistance. In particular, although the classical model fails completely to reproduce the low-temperature fluctuations (which come from interference), it does yield the correct qualitative behavior of the high-temperature resistance. Nonetheless we expect effects due to mode quantization and diffraction of the electron waves to be substantial in this few-mode regime, and this leads us to attempt to define a quantum average resistance for these systems. Much of this paper is devoted to defining two types of quantum averages and studying their behavior, which we find does differ substantially from the classical results for the same structures.

Figure 1 summarizes our main results by showing four calculations of $R_H(B)$ (at a particular Fermi energy) described in detail below. The nearly straight line (dash-dotted) is the result for a simple square-corner junction (Fig. 2) and is nearly equal to the two-dimensional linear behavior. The smooth dotted line is the classical behavior of a four-disk junction (inset to Fig. 1) which shows quenching at small magnetic fields and enhancement of R_H at larger fields. The remaining two calculations are the full quantum behavior (solid line) and the average quantum behavior (squares). The deviations of all three calculations for the four-disk structure from that for the square-corner structure shows the strong influence of geometry in these ballistic structures. Both the large fluctuations in the full quantum behavior and the fact that the average quantum behavior shows enhanced quenching compared to the classical result are evident from these results.

In order to describe transport in the ballistic regime, it seems reasonable to neglect scattering from impurities completely and to view the transport properties in terms of scattering from the geometry of the junction. Thus it is natural to use the approach advocated and developed by Landauer[4] and Büttiker[5] in which one expresses the resistance of the system in terms of its transmission properties between reservoirs attached to leads. In particular, Büttiker showed[5] that in a multiprobe structure, the current in any lead j, I_j, is related to the voltages applied by reservoirs to the other leads n, V_n, through the transmission probability to go from lead n to lead j, T_{jn},

$$I_j = \frac{e^2}{h} \sum_{n=1}^{N} T_{jn}(V_n - V_j) \ . \tag{1}$$

This equation has formed the basis for nearly all of the theoretical discussion of ballistic magnetotransport

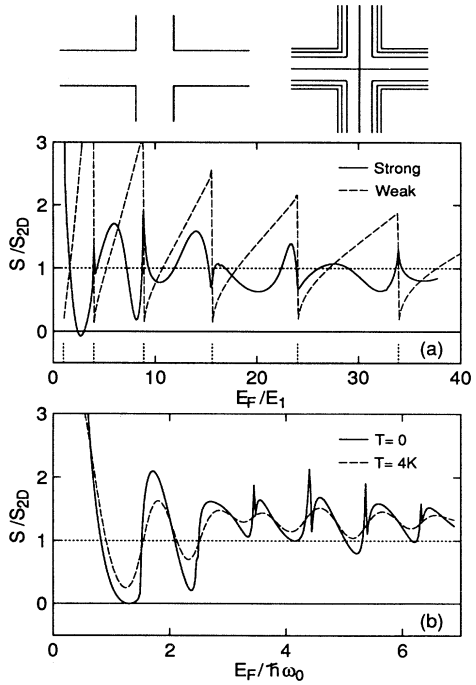

FIG. 2. The slope of the Hall resistance at B=0 normalized to its two-dimensional value as a function of Fermi energy for various square-corner junctions. (a) Infinite hard-wall barriers (structure at top left) with either four identical leads (solid) or weakly coupled voltage leads (dashed). The dotted ticks mark subband thresholds in the wires where E_1 is the threshold of the lowest subband. (b) Harmonic confining potential (contour plot at top right with spacing of $3\hbar\omega_0$) for two different temperatures. The lack of quenching for $N_M \geq 3$ shows that these square-corner models cannot explain the quenching seen in many experiments.

anomalies. It can also be derived from the more familiar Kubo-type linear-response theory in an arbitrary magnetic field.[6–9]

After applying the appropriate boundary conditions—one lead used to supply the current, another used to sink the current, and zero current in the voltage leads—Eq. (1) can be solved for the four-point resistance, defined as the voltage difference between two leads divided by the current. If one measures the voltage between leads j and n when a current goes from lead m to lead k, the general expression for the resistance, $R_{mk,jn}$, is

$$R_{mk,jn} = (h/e^2)(T_{jm}T_{nk} - T_{jk}T_{nm})/D \ , \tag{2}$$

where D is any cofactor of the matrix $g_{jn} = T_{jn} - N\delta_{jn}$. In this paper we restrict ourselves to the case of four identical leads so that the junction has fourfold symmetry. Using this symmetry in the general expression Eq. (2), one finds that the Hall resistance and bend resistance are

$$R_H = (h/e^2)(T_R^2 - T_L^2)/D \ , \tag{3}$$

$$R_B = (h/e^2)(T_F^2 - T_L T_R)/D \ , \tag{4}$$

where

$$D = (T_R + T_L)[2T_F(T_F + T_R + T_L) + T_L^2 + T_R^2] \ , \tag{5}$$

T_F is the forward transmission, T_R is the probability to turn right, and T_L is the probability to turn left. It will be useful in the discussion below to rewrite R_H in terms of the relative asymmetry between left-turning and right-turning electrons $\alpha = (T_R - T_L)/(T_R + T_L)$, the total probability to turn a corner $T_{RL} = T_R + T_L$, and $\tilde{D} \equiv (e^2/h)D/T_{RL} = (e^2/h)[2T_F(T_F + T_{RL}) + T_{RL}^2(1+\alpha^2)/2]$:

$$R_H = \alpha T_{RL}/\tilde{D} \ . \tag{6}$$

We emphasize that these expressions for the resistance are those appropriate to a transport measurement in which currents are applied and the chemical potential of reservoirs is measured;[5] the behavior of the electrostatic potential in the microstructure (the Hall field, for instance) is a separate topic on which we comment briefly in discussing recent work below.

A. Early work

The first observation of quenching of the Hall resistance was made by Roukes *et al.*[10] and this was followed by a study by Ford *et al.*[11] These two papers established that quenching exists in a variety of differently fabricated structures and persists over a sizable range of density and magnetic field (~100 mT). The first observation of a bend resistance by Timp *et al.*[12] established that R_B is large in the ballistic regime at zero magnetic field (~1 kΩ) and decays over a characteristic magnetic field scale (~100 mT). It was noted that the bend resistance is substantial even when the leads are misaligned—the bend resistance is nonlocal.

Initially, it was unclear whether quenching of the Hall resistance is an intrinsic property of narrow wires or a property which depends in more detail on the way in which leads are attached to the wire. By an intrinsic property we mean, for instance, one which depends only on the quasi-one-dimensional nature of the wires or on a comparison of the width to a magnetic length, and several intrinsic quantum-mechanical mechanisms were initially proposed.[10,13] To investigate this, R_H was calculated for a current-carrying wire with two weakly coupled voltage leads—leads with a tunnel barrier between the current channel and the voltage lead. Quantum calculations of the resistance from the general formula Eq. (2) to lowest order in the coupling (and within the independent particle approximation) did not show quenching.[14,15] Thus it was demonstrated that quenching is not intrinsic to narrow wires.

Other theorists then considered junctions with strongly coupled voltage probes—ones, in fact, with identical voltage and current probes—in which the corners were square.[16,17,3] By a square-corner junction we mean one in which the equipotential lines make right angles at the junction; two examples are shown in Fig. 2, one for hard-wall confinement and the other for harmonic confinement. While the quantum magnetotransport properties of square-corner junctions were found to exhibit rich structure including quenching at certain specific densities,[16,17,3] square junctions do not exhibit the quenching over a wide range of densities seen in the experiments. In Fig. 2 we show the slope of $R_H(B)$ at B=0 as a function of energy (electron density) for two square-corner junctions.[3,18] For these square corner junctions, $R_H(B)$ is smooth—a typical trace is shown in Fig. 1—so that the slope at B=0 is both well defined and a meaningful characterization of the low-B behavior. The rich structure in the curves in Fig. 2 is connected to the sequence of allowed transverse modes in the quantum wires which, naturally, act like electron waveguides. Note that large deviations from the two-dimensional slope are obtained only in a narrow region of energy for both confinement potentials. The results for weakly coupled voltage probes[19] shown in panel (a) confirm that no quenching is obtained in this limit, though the curve shows considerable structure not anticipated in the early work.[14] Thus, quenching of the Hall resistance is not intrinsic to narrow wires and does not occur in square-corner junctions over a broad range of density.

The initial theory of the bend resistance was more successful than that of the Hall resistance. In fact, calculations on a square-corner junction give the correct order of magnitude for the bend resistance and the correct global dependence on energy for zero magnetic field.[12] The presence of a bend resistance in the ballistic regime was attributed to the preferential transmission straight through the junction as opposed to around the corner. Subsequent calculations in square-corner junctions showed sharp features in R_B at the threshold for the transverse modes of the wire,[20,18] investigated the decay of the bend resistance with applied magnetic field,[17] and studied filtering and nonlocality in double-junction structures.[21]

A second generation of experiments demonstrated the importance of the geometry of the junction in producing

magnetoresistance anomalies. Ford *et al.*[22] found that the incorporation of flattened corners into their otherwise normal junction produced a Hall resistance which was strongly negative. This "inversion" went away when a nonconducting dot was made in the middle of the junction. They argued that this behavior is caused by the contribution of special paths to the Hall resistance, namely the "rebound" trajectories which reflect from the flattened corners (discussed further below). Chang, Chang, and Baranger[23] studied the Hall resistance of structures rather different from the usual intersecting-wire junction: pinches were patterned onto the leads of junctions made with relatively wide wires. They found that quenching did occur in such a system when all four wires had pinches but not for fewer pinches. Finally, Takagaki *et al.*[24] showed the large magnitude of the bend resistance in the simple single junction geometry [Fig. 6(b)]. Subsequently, a thorough characterization of the bend resistance as a function of junction width, field, temperature, and misalignment of the leads (nonlocality) was performed.[24,25] The main conclusion of this second generation of experiments was that the magnetotransport properties of microstructures are extremely sensitive to the geometry of the structure.

B. Collimation

Quenching at a wide range of energies was obtained theoretically by Baranger and Stone,[3] who also showed the importance of geometry. They calculated the Hall resistance quantum mechanically for a junction in which the wires gradually widen approaching the junction and found that $R_H(B)$ has nearly zero slope for all energies studied. They argued that the gradually widened wires simulated the effect of rounded corners at the junction which were likely to be present in the experimental structures because of depletion. Subsequently, it was shown that quenching exists in structures with other kinds of rounding: Fig. 1 shows calculated results for a structure with circularly rounded corners which we call a four-disk junction. The underlying reason for quenching was proposed to be the collimation of the electrons by the gradually widened wire or rounded corners.[3,18]

Since *collimation* plays a crucial role in our understanding of these magnetotransport anomalies, we explain this concept at some length from both classical and quantum-mechanical points of view using Fig. 3. Collimation is closely related to the idea of adiabatic transport introduced by Glazman *et al.*[26] in discussing the quantized point contact conductance, and the importance of collimation in ballistic point contacts has been discussed by Beenakker and van Houten[27] and by Imry.[28] Classically,[27] a particle injected into the rounded-corner structure of Fig. 3 with a large transverse momentum $k_\perp$ has its **k** vector rotated by the gradual widening of the wire so that it is injected into the junction region with a large component of its **k** vector parallel to the injecting lead, $k_\parallel$ [see the trajectory in Fig. 3(a)]. Thus particles injected with a hemispheric distribution function far from the junction reach the junction collimated into a forward cone [Fig. 3(c)]: graded wires produce a collimated electron beam. Quantum mechanically,[3] suppose one injects a wave packet from the left in the horizontal arm; what is the behavior of this wave packet at later times? We show in Fig. 3(b) the thresholds for the transverse subbands at the two points x_1 and x_2 assuming infinite strips of the same width as the graded wire at those points. Since at x_1 the wire is narrow, the transverse subbands are widely spaced, while at x_2, the subbands are much closer together. If the widening of the wire is gradual, the electrons will travel adiabatically from point 1 to 2, and thus will conserve their transverse-mode number.[26] That is, the injected wave packet sees a time-varying confinement potential $U(y,t) \approx U(y, x_1 + v_g t)$ for short times. In general this will generate transitions between the subbands; however, if the time variation is slow enough, the wave packet will largely remain in the subband in which it is injected (adiabatic behavior). Thus, particles injected from a reservoir such that the current is evenly distributed across all the subbands below E_F [solid lines at x_1 in Fig. 3(b)] end up in the low-lying transverse subbands as they approach the junction (solid lines at x_2). Thus, arguing either classically or quantum mechanically, we find that a nonequilibrium momentum distribution is created in the junction region. *It is this structure in the momentum distribution that we refer to as collimation.*

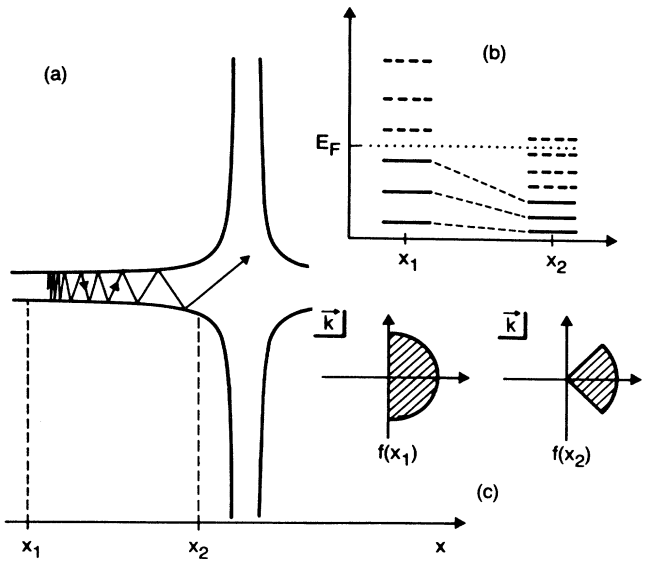

FIG. 3. Schematic of the physics of collimation in a junction with rounded corners as shown in panel (a). (b) The threshold energy of the transverse subbands at two places in the structure. For gradual grading, the injected electrons conserve their mode number (dotted lines). Current initially injected in all modes below the Fermi energy (solid lines at x_1) is carried only by low-lying modes near the junction. (c) Distribution functions of classical particles at two places in the structure. The grading rotates the **k** vector of the classical particles into the forward direction, as indicated by the trajectory in part (a). Thus particles injected with a hemispheric distribution of **k** vectors emerge collimated into a cone.

Experimentally, the presence of collimation in microstructures has been demonstrated by Molenkamp *et*

al.[29] They consider a point contact, which acts like a single gradually widened narrow wire, connected to a large two-dimensional region with a second point contact on the other side. A magnetic field is used to sweep the electrons emitted from the first point contact across the second and show that the distribution of the electrons in angle is smaller than expected from a diffusive source, hence demonstrating collimation.

Collimation influences the magnetotransport properties because the scattering properties of the junction [the T_{jn} in Eq. (1)] depend on the momentum distribution in the junction. Near the junction, the adiabatic approximation breaks down since the equipotential contours must turn through 90°. Here the wave packet is scattered into different modes and into the different probes. The fact that the scattering properties of a junction are very different for the different modes[12,21] implies that the physical result of injecting a nonequilibrium momentum distribution could be quite different from injecting the current in all the modes. Indeed, by analyzing the transmission properties of a square-corner junction, Baranger and Stone found that the low-lying modes make a much smaller contribution to R_H than the high-lying modes.[3] The nonequilibrium momentum distribution caused by the graded wires generates quenching.

The possible effects of collimation on R_H can be made clear by expressing R_H in terms of the asymmetry between left- and right-turning probabilities and the total turning probability as in Eq. (6). R_H can be suppressed either by (1) decreasing the asymmetry while the total turning probability remains large ($\alpha \rightarrow 0$ while $T_{RL} \approx$ const) or by (2) decreasing the total turning probability quite apart from the asymmetry ($T_{RL} \rightarrow 0$ while $\alpha \approx$ const). It is clear that collimation, and hence grading, may reduce T_{RL} simply because more classical trajectories will impinge on the opposite lead relative to the adjacent lead when collimation is present. The effect of grading or collimation on the asymmetry is less clear *a priori*. An analysis of the early results showed that *both* of these suppression effects are present.[3]

The possible effects of collimation on R_B can be derived directly from the original explanation for the large ballistic bend resistance: enhancement of the forward transmission at the expense of turning transmission. Collimation may contribute, of course, by directly enhancing the forward transmission.[2,25] In addition, sufficient collimation implies that the injection cone in one lead does not overlap with the acceptance cone of the adjacent lead so that direct turning paths are eliminated, decreasing the turning probability.[2,32]

Motivated by the experiments of Ford *et al.*[22] and of Chang, Chang, and Baranger[23] the calculations were extended to investigate the effect of various geometries on the low-field Hall resistance.[30] For structures patterned after those used in the experiments, qualitatively similar results were obtained, including "inversion" of R_H in structures with flattened corners and the necessity of having four pinches to produce quenching.

Since collimation is clearly a classical concept, a classical approach ought to give qualitatively similar results. Indeed, Beenakker and van Houten[2] performed a classical calculation of the transmission coefficients through a junction (a "billiard ball" approach described in more detail below). They obtained both quenching and inversion of R_H in appropriate geometries, as well as a plateau in R_H (which was previously dubbed the "last plateau"[10]) caused by guiding of the electrons around the rounded corner by the magnetic field. They showed that the bend resistance decayed as a function of magnetic field in qualitative agreement with the experiments. Because of the nature of the classical calculation, the authors were able to look at the distribution of particles close to the junction and show that the injected particles are collimated in the geometries they considered.

The mechanism connecting collimation to quenching remains controversial: classically, how does collimation cause deviations from two-dimensional behavior, or quantum mechanically, why do low-lying modes contribute less to R_H than high-lying modes? A useful way of thinking about the different proposed mechanisms is by classifying the important types of classical trajectories, as indicated schematically in Fig. 4. One proposal discussed above is that the forward-directed paths lead to a suppression of the total probability for turning the corner either to the right or left [Fig. 4(a)].[3] We call this mechanism the total-turning suppression mechanism or more generally the "magnitude effect" since the absolute magnitude of the transmission probabilities are involved rather than the relative magnitude of turning right to turning left. A second proposal is that the asymmetry between turning left or right is reduced by simple trajectories in the junction region such as the "rebound" trajectory thought to cause inversion shown in Fig. 4(b).[22] Collimation is important in this proposal in order to emphasize particular anomalous trajectories. For instance, in the case of the rebound trajectories, there are also trajectories which reflect into the left-hand probe at $B=0$ and which bend into the right-hand probe at nonzero field yielding an extra large contribution to R_H of the correct sign; collimation emphasizes the rebound trajectories at the expense of this latter set. We call this mechanism the asymmetry suppression mechanism, or simply the asymmetry effect. Finally, the complicated scattering in the junction region produces long "scrambling" trajectories [Fig. 4(c)] which may tend to equalize the left-turning and right-turning probabilities and hence produce quenching, as introduced in Ref. 2. Collimation is important in the scrambling mechanism because it eliminates the possibility of directly turning the corner

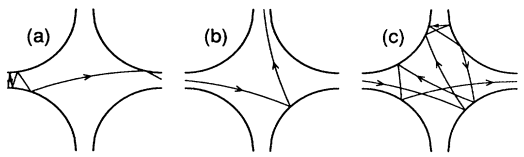

FIG. 4. Schematic of the proposed explanations of quenching. Collimation emphasizes the importance of (a) short forward-directed paths, (b) short paths which diminish the asymmetry between turning right or left (a "rebound" trajectory is shown as suggested in Ref. 22), or (c) long scrambling trajectories.

and therefore enhances the complexity of those trajectories which do turn the corner.[2] Reference 2 emphasizes that a scrambling mechanism can be effective only when the injection cone on one lead does not overlap with the acceptance cone on the adjacent lead, a situation produced by collimation. The implication in Ref. 2, and indeed in the term "scrambling" itself, is that an average over many long trajectories is involved in the scrambling mechanism of quenching, though this is not stated explicitly. Here we will use the term "scrambling" to refer to long complex trajectories as distinct from short simple trajectories such as the rebound trajectories. Thus the two central questions concerning the mechanism of quenching are the following: do short trajectories or long trajectories produce quenching, and is reduction of asymmetry or total-turning probability more important?

C. Recent work

Recent experiments have emphasized a careful characterization of the different magnetotransport anomalies. Timp *et al.*[31] showed that there is a correlation between the Hall resistance and the bend resistance and that both change in character as the density or width changes. In their structures, the quenching region becomes much smaller while the width of the bend resistance remains approximately constant as the number of subbands increases. Roukes, Scherer, and Van der Gaag[32] studied a series of structures with different amounts of rounding and interpreted their results in terms of the classical model with disorder effects. This was the first explicit study of the role of scattering in the experiments; the authors emphasize[32,33] that scattering cuts off the length of the ballistic trajectories that can contribute to the resistance. Because these experiments probe the degree of ballistic behavior needed to see the transport anomalies, they have a direct bearing on our discussion of the mechanisms for quenching, and we will return to discuss this work below (Sec. III B). Most recently, Behringer *et al.*[34] have observed large quantum effects in the *average* bend resistance of a junction and confirmed these observations with calculations.

The more recent theoretical work has addressed a number of related issues. First, the question of the intrinsic Hall effect in narrow wires and the nature of the electrostatic potential has been revisited with the self-consistent field of the electrons included.[35] Extending previous work within the independent-particle approximation[36] or at high magnetic fields,[37] the authors show that the intrinsic Hall effect is not quenched at low magnetic field in quasi-one-dimensional wires within the self-consistent field approximation. Second, structures in which the classical scattering is chaotic have been studied both with regard to characterizing the classical behavior[33] and with regard to connecting the large quantum fluctuations to the classical chaos.[38] Third, while most of the theoretical work to date has been on strictly ballistic junctions, it has recently been shown[39] that disordered leads attached to a ballistic junction modify the injection distribution which in turn affects the magnetotransport properties.[33,39,40] Finally, Hall and bend resistances have been calculated for perfectly adiabatic leads attached to a square-corner nonadiabatic region by combining the scattering matrices of the different parts of the structure.[41] While one cannot study specific geometrical effects with this approach, one can study general properties of R_H and R_B in an especially simple way. Of particular interest is the fact that phase breaking can be introduced in the junction region by combining transmission intensities rather than transmission amplitudes.[41]

D. Overview

In this paper we address four issues which are central to the current understanding of both quenching and bend resistances. First, we emphasize that the geometry of the junction has a large effect on the magnetotransport properties. We calculate both the bend resistance and the Hall resistance for a variety of structures—circular rounding and linear widening of the wires, soft- and hard-wall potentials, and junctions with a cavity. A gradual widening of the wires or rounding of the junction corners is essential to produce quenching over a wide range of energies. The magnitude of the bend resistance and decay as a function of magnetic field depends sensitively on the junction geometry. We emphasize that all of our results can be understood in terms of structure in the momentum distribution of the injected electrons, that is, in terms of collimation.

Second, we investigate the relationship between the classical and quantum results. The most apparent difference, evident from Fig. 1, is that the classical resistance is much smoother as a function of field than the quantum resistance: quantum fluctuations in $R_H(B)$ are large. These fluctuations result from the interference among the many complicated trajectories [Fig. 4(c)] trapped in the junction region as discussed by Jalabert, Baranger, and Stone.[38] In comparing with experiments, we are concerned with measurements at $T \approx 4$ K in this paper since most of the quenching and bend resistance studies have been done in this regime. Fluctuations are not evident in these experimental results presumably because the phase-breaking rate is sufficient at these temperatures to remove the interference effects of the relatively long trajectories involved. The experiments done at low temperature ($T \approx 300$ mK) in the ballistic regime[11,31,42] do show fluctuations which may well be caused by junction scattering as in our calculations. The relation between the fluctuations and the classical dynamics is itself a fascinating problem,[38] but here we wish to concentrate on comparing the classical results to the "average" quantum results, quantum results with the fluctuations caused by long trapped trajectories taken out. Thus, we need to find appropriate ways of extracting the quantum average.

The most straightforward way to perform this average would be to include a phase-breaking process as in the experiments. However, though partially phase-coherent transport has received considerable attention recently, calculations for only the simplest structures have been carried out.[43] Thus, we prefer to use the approach developed in discussing diffusive systems of averaging over the energy, the magnetic field, and the impurity config-

uration. We use two types of averages both of which are physically motivated. In the first technique, we perform an energy average by convolving the transmission coefficients with the derivative of the Fermi function [the appropriate generalization of Eq. (1)] and then average the resulting resistances over a magnetic-field interval. We call this the field-energy average. The average over energy accounts for the thermal smearing present in the experimental structures while the average over magnetic field is used to extract the "typical" low-field behavior. In the second technique, we average over a distribution of very weak random impurities as well as a small energy window. From a semiclassical point of view, the weak impurity average (the mean free path is kept larger than the size of the junction) "dephases" the long trajectories while retaining the coherence of the short paths: the small phase shifts from individual impurities accrue over the trajectory, and the subsequent average over an ensemble of impurities removes interference effects of those trajectories whose total phase shift is $\sim \pi$ while retaining interference effects of short trajectories. We call this the impurity-energy average and use it to calculate the resistances as function of magnetic field. The average over impurities is a crude way of including some phase randomization while the average over energy incorporates finite-temperature effects. The agreement between the two averaging techniques is very good.

Using both of these averaging techniques, we compare the classical results to the average quantum results. We find that there are substantial differences in the regime of several subbands (≈ 6) and deviations in some structures at even higher energies. Deviations are, of course, expected in the few-subband limit ($\approx$1–2) but survive to surprisingly large energies. Compared to the classical results, the quantum results show substantially enhanced quenching, slower decay of the bend resistance as a function of field, strong variation on an energy scale less than the subband spacing, and periodic oscillations as a function of field in certain structures. While more details about both averaging methods are given below, we recall at this point the typical results discussed earlier: Fig. 1 shows a classical calculation, an unaveraged quantum calculation, an impurity-energy averaged trace, and a trace for the simple square-corner structure. Note that the averaging does indeed remove most of the quantum fluctuations while retaining the typical behavior, and that the quantum average is substantially different from the classical case.

The third issue we address in this paper is the mechanism for quenching of the Hall resistance. By analyzing classical results in terms of trajectories, we show that the Hall-resistance quenching and bend-resistance anomalies are both short trajectory effects. Thus we rule out "scrambling" by long trajectories suggested in Ref. 2 as a mechanism for quenching. We analyze both the classical and quantum results in terms of the asymmetry and total turning transmission as discussed above in connection with Ref. 3. The relative importance of these two mechanisms depends on the geometry: in the four-disk junction, the magnitude effect (suppression of total-turning transmission) is small while in the linearly graded structures it is large.

Fourth, we discuss the local properties of the junction, especially in the coherent regime. By local properties we mean the charge density, current density, and momentum distribution of particles inside or near the junction. While this has received some attention in the classical case[2] or in simple quantum structures,[44] this is the first work on such properties in these rounded junctions. We find that the charge density and current density are highly structured because of quantum interference. We illustrate collimation directly in the momentum distribution and indirectly in the current density pattern. The importance of "rebound" trajectories in flattened-corner structures[22] is evident in the standing-wave pattern in the charge density and in the momentum distribution near the reflecting wall.

The organization of the rest of the paper is as follows. We explain our methods of calculation, both classical and quantum, in Sec. II. The classical results—resistance traces, analysis in terms of trajectory length, and asymmetry analysis—are presented in Sec. III. Section IV covers the quantum results using the field-energy averaging technique and emphasizes the general properties of the different geometries as well as deviations from expectations in specific structures. The impurity-energy averaged results are in Sec. V in which the emphasis is on differences between the classical and quantum results. Finally, the local properties of the junction are discussed in Sec. VI. Concluding remarks and a discussion of the implications of our results for previous interpretations of magnetotransport anomalies are in Sec. VII. The appendixes contain further information on recursive Green-function methods for multiprobe structures and attaining the classical results from the semiclassical limit of the quantum calculation.

II. METHODS OF CALCULATION

A. Quantum transmission

In order to calculate the resistance according to Eqs. (2)–(4), we must evaluate the probability of transmission between all pairs of leads. Because all of the scattering occurs in the junction region, the leads act as electron waveguides in the quantum regime. It is natural to introduce a set of transverse wave functions, or modes, $\chi_a(y_n)$ which are a function of the transverse coordinate in lead n, y_n. The quantum scattering problem, then, consists of finding all the transmission amplitudes, $t_{jn,ba}$, from mode a in lead n to mode b in lead j. The total transmission is then $T_{jn} = \sum_{a,b} |t_{jn,ba}|^2$. The assumption in using this expression for T_{jn} in the relation between currents and voltages, Eq. (1), is that the reservoir feeds equal current into each mode. This results from the well-known cancellation between the Fermi velocity and the density of states in one dimension and from assuming that the connection between the reservoir and the wire is reflectionless.[4,5,45] There are three essential ingredients to our method of calculating the amplitudes: the relation of transmission amplitudes to the Green function,[7–9] the

discretization of the continuum problem to obtain a tight-binding Hamiltonian, and the recursive calculation of the discrete Green function.[46]

The first ingredient is to obtain an expression for the transmission amplitudes in terms of the Green function for the quantum scattering problem. The scattering wave states provide a complete orthonormal basis:[47] $\psi^{\dagger}_{n,a,k}$ is the state with an incoming wave with wave vector k in lead n and mode a. The behavior of the scattering-wave states far from the junction is simply related to the transmission amplitudes and transverse wave functions.[8,9] The retarded Green function in the spectral representation is[48]

$$G^{+}_{\varepsilon}(\mathbf{x},\mathbf{x}') = \int d\alpha\, \psi^{\dagger}_{\alpha}(\mathbf{x})\psi^{\dagger *}_{\alpha}(\mathbf{x}')/(\varepsilon - \varepsilon_{\alpha} + i\eta)\ , \tag{7}$$

where α represents all the quantum numbers, n, a, k. The asymptotic behavior of the Green function in terms of the transverse wave functions and transmission coefficients can be evaluated by a contour integration. In the absence of a magnetic field, the transmission amplitude is simply the projection of the Green function onto the transverse wave functions,[7,8]

$$|t_{jn,ba}| = \hbar\sqrt{v_b v_a}\left| \int dy_j \int dy'_n \chi_b(y_j)\chi_a(y'_n) \times G^{+}_{\varepsilon}(\mathbf{x}_j,\mathbf{x}'_n)\right|\ , \tag{8}$$

where v_a is the longitudinal velocity of mode a (at the Fermi surface). In fact, this projection can be done at any point in the lead outside the scattering region since the population of the various transverse states will not change in the ideal lead. In all of the calculations performed here, the projections are done in zero magnetic field; the magnetic field is graded from the value in the junction to zero in the leads. For the low-field properties discussed here, we expect that this approximation should be accurate and checked in several cases that the rate of the grading did not affect the results. For high-field calculations, the full relation between the amplitudes and the Green function[9] should be used.

Next, in order to calculate the Green function numerically, one needs to discretize the continuum problem. We use the usual tight-binding Hamiltonian on a square lattice:[46]

$$H = \sum_{i,j}\varepsilon_{i,j}|i,j\rangle\langle i,j| - \sum_{i,j}(V^{x}_{i,j}|i,j\rangle\langle i+1,j| + \text{H.c.}) - \sum_{i,j}(V^{y}_{i,j}|i,j\rangle\langle i,j+1| + \text{H.c.})\ , \tag{9}$$

where i and j label the sites in the lattice. In the absence of a magnetic field, the hopping matrix elements are constant, and Eq. (9) is the lowest-order finite difference approximation to the continuum Schrödinger equation. The connectivity of the structure can be varied by setting the hopping matrix element equal to zero between select sites. In a magnetic field, we use the Peierls substitution[49] $V^{x}_{i,j} = \exp(ieA^{x}_{i,j}/\hbar c)$ and $V^{y}_{i,j} = \exp(ieA^{y}_{i,j}/\hbar c)$ to relate the hopping matrix element to the vector potential. In all of our calculations, the flux per unit cell of the lattice is small ($\leq 0.01hc/e$) so we expect this to be a good approximation to the continuum problem. The single-site energy $\varepsilon_{i,j}$ in the Hamiltonian can be chosen at will; in particular, it can be chosen to follow the potential confining the particles to the microstructure. The ability to choose the single-site energies and the hopping matrix elements is central to our work since it allows one to study different junction geometries and to vary the connectivity of the structure.

Finally, the Green function for the discrete problem must be evaluated. We use a standard approach[46] based on Dyson's equation[48] which relates the Green function G of a system in the presence of a perturbation U to the Green function G_0 in the absence of U:

$$G = G_0 + G_0UG = G_0 + GUG_0\ . \tag{10}$$

Here and throughout much of this paper, we drop the + sign on the Green function since we shall only deal with retarded Green functions. By judiciously choosing the unperturbed system and the perturbation, one can derive recursive relations for the Green functions needed.[46] We review the two-probe case—an infinite strip containing a finite scattering region—in this section to illustrate the method. For multilead junctions, we derive new recursion relations using the same basic idea; these somewhat more complicated relations are presented in detail in Appendix A.

In the simplest case of an infinite strip, one can use a semi-infinite half-strip plus a disconnected column as the unperturbed system and the hopping matrix elements connecting these two as the perturbation.[46] Let the matrix $\underline{G}^{L}_{n}$ be the Green function of the left half-strip terminated at column n and $\underline{g}_{n+1}$ be the Green function of the isolated column $n+1$. $\underline{G}^{L}_{n}$ can be calculated exactly if the cross section of the half-strip is uniform, as it is outside the scattering region. Furthermore, let $\underline{G}^{L}_{n}(n,n)$ be the part of $\underline{G}^{L}_{n}$ that connects column n to n and $\underline{U}(n,n+1)$ be the hopping matrix element that connects column n to $n+1$. Taking matrix elements of Eq. (10) between column $n+1$ and $n+1$, one obtains the exact relation

$$\underline{G}^{L}_{n+1}(n+1,n+1) = [\underline{I} - \underline{g}_{n+1}\underline{U}(n+1,n)\underline{G}^{L}_{n}(n,n)\underline{U}(n,n+1)]^{-1}\underline{g}_{n+1}\ . \tag{11}$$

Here $\underline{I}$ is the identity matrix. Using this equation, then, one can start with a perfect left half-strip and work across the scattering region. In order to attach a perfect right half-strip to obtain the full Green function for the strip, take $\underline{G}_0 = \underline{G}^{L}_{n} + \underline{G}^{R}_{n+2} + \underline{g}_{n+1}$ where R denotes a right half-strip and use Eq. (10) with $\underline{U}$ connecting column $n+1$ to both the left and the right:

$$\underline{G}(n+1,n+1) = \{\underline{I} - \underline{g}_{n+1}[\underline{U}(n+1,n)\underline{G}^L_n(n,n)\underline{U}(n,n+1) + \underline{U}(n+1,n+2)\underline{G}^R_{n+2}(n+2,n+2)\underline{U}(n+2,n+1)]\}^{-1}\underline{g}_{n+1} . \quad (12)$$

This Green function provides the reflection coefficient from the right via Eq. (8) from which one obtains the conductance. In the case of a junction, we use these relations to move down each lead individually with the matching at the junction done as a single step in the recursion; details are in Appendix A. An important advantage of this recursive technique is its numerical stability; naive transfer matrix techniques, for instance, are unstable for these problems.[46,50]

B. Classical transmission

The arguments given for the relation between transport and transmission probabilities, Eq. (1), have been made explicitly for the quantum regime.[4,5] However, it seems reasonable that the expressions for the resistance, Eqs. (2)–(4), should remain valid in the classical regime with the understanding that the transmission coefficients must be evaluated for classical ballistic particles. Taking this point of view, Beenakker and van Houten[2] calculated the classical resistance of ballistic junctions through an intuitive Monte Carlo evaluation of the transmission probabilities: they traced ballistic trajectories among the leads and counted how many went between each pair of leads. We use the same basic method in calculating classical resistances.

A crucial quantity in carrying out this procedure is the probability for injecting a particle into the junction with a given transverse coordinate and wave vector. Since one is interested in the transmission of current in a transport experiment, we will call this the "current injection distribution." Beenakker and van Houten argued based on classical kinetic theory that the current injection distribution in a hard-wall lead in zero magnetic field is uniform across the lead and varies as the cosine of the injection angle. They were unable to give analytically the current injection distribution either for soft-wall confinement or in a magnetic field but obtained the distribution numerically in these two cases.

Using two different arguments, we give a formal justification for this intuitively appealing classical approach; indeed, these two arguments amount to a derivation of the relation between current and voltage through transmission probabilities, Eq. (1), in the classical regime. First, the classical approach has been derived[21] from a Boltzmann equation in which Fermi-Dirac statistics is assumed but the particles are otherwise treated classically. This method gives an explicit prescription for calculating the current injection distribution in any case of interest. Second, we show that a semiclassical form of the Green function used in the expression for the quantum transmission coupled with a further classical approximation produces the same classical approach. We now briefly summarize these two arguments.

In the Boltzmann-equation approach,[21,51] the basic quantity is the distribution function $f(\mathbf{r},\mathbf{k})$ which is *not* equivalent to the current injection distribution. One assumes, as in the quantum case,[4,5,45] that each lead of the junction is attached in a reflectionless way to a (two-dimensional) reservoir characterized by a chemical potential. The Boltzmann equation coupled with "reservoir" boundary conditions—that the limit of f down a lead away from the junction be the Fermi distribution characterized by the appropriate chemical potential—is a well-posed differential equation for $f(\mathbf{r},\mathbf{k})$. In the absence of a scattering term as in a ballistic problem, the solution of this equation is that the distribution function be constant along any classical trajectory. The prescription for $f(\mathbf{r},\mathbf{k})$, then, is to follow each trajectory at $\mathbf{r}$, characterized by $\mathbf{k}$, backwards in time until it is clear from which reservoir the particle came, say n; this direction in $\mathbf{k}$ space at $\mathbf{r}$ is therefore filled to energy $\varepsilon_k = \mu_n$.

Using this general prescription, we derive, first, the distribution function at injection and, second, the current injection distribution, in three simple cases of interest in this paper. (1) In a straight wire with hard walls and zero magnetic field, all the particles moving towards the junction, $v_\parallel > 0$, came from the reservoir attached to that lead. Thus all the trajectories moving towards the junction are filled to the chemical potential of the injecting reservoir: the distribution function of particles going into the junction region is uniform in angle and independent of transverse coordinate. Because the current for this distribution function is equally distributed across all transverse wave vectors, this distribution corresponds to the quantum injection condition of equal current in each mode used in Landauer-type arguments.[4,5,45] In order to find the injected current from this distribution function, one must multiply by $v_\parallel$ which is proportional to the cosine of the injection angle and integrate over the transverse coordinate. Thus, the current injection distribution is uniform across the lead and varies as the cosine of the injection angle, as introduced[2] by Beenakker and van Houten. (2) In a wire with soft walls and B=0, again all the particles with $v_\parallel > 0$ in lead n came from reservoir n, so that these trajectories are filled to μ_n. Because the density of states in two dimensions is constant, the change in injected density caused by a change in chemical potential $\delta\mu_n$ is independent of transverse coordinate. Thus, the distribution function of particles going into the junction region is uniform in angle and independent of transverse coordinate, as before. The injected current is again given by multiplying by $v_\parallel$ and integrating over the lead. Because the velocity depends on the transverse coordinate y, the current injection distribution is no longer uniform across the lead but rather is proportional to $v_F(y) = \{2[E_F - U(y)]/m\}^{1/2}$, peaked in the center of the lead. The distribution in angle varies as the cosine of the injection angle, as before. (3) Finally, in a hard-wall wire of width W with a nonzero magnetic field, it is no longer true that all the particles with $v_\parallel > 0$ in lead n came from reservoir n; in fact, if the

cyclotron radius ℓ_c is smaller than $W/2$, some trajectories are not connected to any reservoir and do not contribute to transport. However, following the general prescription for finding f, we find the injection distribution function for particles moving to the right with clockwise cyclotron orbits: if the transverse coordinate y measured from the bottom side and the angle measured from the horizontal, θ, satisfy

$$|\theta| < \pi/2 + \arcsin[1 - y/\ell_c], \quad y < 2\ell_c < W ,$$
$$|\theta| < \pi/2 + \arcsin[(W/2 - y)/\ell_c], \quad W < 2\ell_c , \tag{13}$$

the trajectory originates from the reservoir at the left characterized by μ. These trajectories, then, are filled to μ and this constitutes the injection distribution function. Multiplying by $v_\parallel$ and integrating over y, we find that the current injection distribution has the same spatial distribution as given in Eq. (13) but has an additional factor of $\cos\theta$ superposed on the angular distribution. In carrying out a Monte Carlo simulation in this case, note in addition that care must be taken to avoid double counting of those trajectories which traverse the given cross section twice before hitting one of the walls.

For simplicity, in the magnetic-field calculations done in this paper, we neglect the effect of the magnetic field on the distribution function at injection. Thus we use a distribution function which is uniform in angle and uniform across the wire. In several cases, we added a constant or adiabatically increasing magnetic field in the leads and checked that this made no difference in the results. We expect all the results shown here to be insensitive to this approximation because we work exclusively at small fields.

An alternative derivation of the classical transmission method can be given starting from the semiclassical WKB expression for the transmission amplitude; this approach makes the relationship to the quantum amplitude somewhat clearer. We briefly summarize the argument here; details are given in Appendix B for the hard-wall case and Appendix C for the soft-wall case. In order to arrive at a classical approximation to the quantum transmission, Eq. (8), we start by using a WKB expression for the Green function in terms of a sum over classical paths.[52] By neglecting interference among the different classical paths and taking the number of transverse modes to infinity, we obtain the same classical current injection distribution as by the Boltzmann equation argument, e.g., uniform across the lead and varying as cosine of the injection angle for the hard-wall case. This calculation shows explicitly, then, that the usual quantum injection condition—equal current in each incoming mode—yields the now familiar classical current injection distribution. Finally, we note that in deriving these results we have neglected the fluctuation effects which are so prominent in the quantum calculations (see Fig. 1). Our numerical studies of the dependence of these fluctuations on the number of modes N suggest that the classical results are *not* approached as $N \to \infty$ at zero temperature.[53] In fact, in Appendix B we show that the classical results for the transmission coefficients are obtained from the semiclassical expression when $N \to \infty$ *and* an average of the transmission coefficient is performed over an infinite range of energies. Of course, the structures that we study in this paper and those of experimental interest do not have $N \gg 1$ and do not offer a very large energy window for averaging, suggesting that there may be differences between the average quantum and classical transmission as we find in Secs. IV B. and V B.

C. Local quantum properties

To obtain the charge density, current density, or momentum distribution of the particles, it is necessary to compute the full scattering wave function for states at the Fermi energy. The calculation of the transmission coefficients does not permit us to obtain this wave function without further computation. This is most easily seen by considering the relationship between the Green function and the scattering wave function:[9]

$$\psi^\dagger_{n,a}(\mathbf{x}) = -\frac{\hbar^2}{2m}\int_{C_n} dy'_n G^+_\varepsilon(\mathbf{x},\mathbf{x}'_n)(\mathbf{D}'\cdot\hat{\mathbf{x}}_n) \times\chi_a(y'_j)e^{ikx'_m} . \tag{14}$$

Here $\mathbf{D}'$ is a gauge-invariant gradient operator acting on the primed variables.[9,54] The important feature of this equation is its dependence on G^+_ε, the retarded Green function at energy ε. Its second space argument is confined to a surface C_n deep inside lead n (which is integrated over), but its first argument can be anywhere in the interior of the sample.

However, the calculation of the transmission coefficients requires only $G^+_\varepsilon(\mathbf{x}_m,\mathbf{x}'_n)$, the Green function with *both* its space variables deep into the leads [see Eq. (8)]. So, additional calculations must be done. Of course, it is not necessary to obtain $G^+_\varepsilon(\mathbf{x},\mathbf{x}'_m)$ to get ψ, and in fact we compute the scattering wave function directly from our knowledge of the asymptotic Green function $G^+_\varepsilon(\mathbf{x}_m,\mathbf{x}'_n)$. The scheme is as follows: (1) Obtain the asymptotic scattering wave function $\psi^\dagger_{n,a}(\mathbf{x}_m)$ in all leads m using Eq. (14) and the Green functions used previously in Eq. (8). (2) Solve the Schrödinger equation with this as a boundary condition.

It is worthwhile here to say a few words about the numerical implementation of this procedure. As described above, we approximate the free-electron motion in the ballistic cross geometry using a lattice Hamiltonian defined on a square lattice with sites labeled by i and j, Eq. (9). The set of equations to be solved to obtain the scattering wave function is most easily written down by first considering the Hamiltonian of the system with all the hopping interactions (i.e., the V's) set to zero across the lead surface [C_n's of Eq. (14)]; call it $H^{\rm iso}$. Then the set of equations to be solved for the scattering wave-function amplitudes $\psi^\dagger_{n,a}(\mathbf{x}) = \psi^\dagger_{n,a}(i,j)$ is

$$\sum_{i',j'}\langle i,j|(H^{\rm iso}-\varepsilon)|i',j'\rangle\psi^\dagger_{n,a}(i',j') = (\delta_{in}+\delta_{jn})V\psi^\dagger_{n,a}(\mathbf{x}_n) . \tag{15}$$

Equation (15) has the form of a set of sparse inhomogeneous linear equations, and we have used a standard conjugate-gradient technique to solve them.[55]

This formulation of the solution has the difficulty that if the Hamiltonian of the isolated system $H^{\rm iso}$ happens to have a bound state at energy ε, then Eq. (15) will have a homogeneous solution as well, the wave function will not be unique, and the numerical calculation will fail. This problem could be avoided by matching to the asymptotic solutions along two rows of lattice points along the lead surfaces C_m; however, in practice we found it better to continue to do the matching along just one row as Eq. (15) prescribes and add a small imaginary part $i\eta$ to the energy ε. This eliminates spurious bound-state solutions, and we found that we can set η to be on the order of 10^{-5} of the bandwidth of the system, which adequately stabilizes the conjugate gradient calculation and causes no significant changes in the results described below.

We now give a description of the computation of the current density $\mathbf{j}(\mathbf{x})$ and the charge density $n(\mathbf{x})$. The density $n(\mathbf{x}) = n(i,j)$ is very simply obtained; within our lattice Hamiltonian the density is most naturally defined on the sites of the lattice, and is computed as matrix elements of the (purely local) density operator $n_{\rm op}(i,j) = |i,j\rangle\langle i,j|$ between the scattering states described above. $n(\mathbf{x})$ is presented in contour plots in the figures below.

The current density $\mathbf{j}(\mathbf{x})$ in our lattice model is most naturally described as flowing along the nearest-neighbor bonds of the lattice. The natural operator expression for current flowing along the bond between site i,j and site $i+1,j$ is

$$J(i,j \to i+1,j) = \frac{e}{i\hbar}\left(V^x_{i,j}|i,j\rangle\langle i+1,j| - V^{x*}_{i,j}|i+1,j\rangle\langle i,j|\right) . \tag{16}$$

This expression is given in units where the lattice spacing is unity. There is a similar expression for vertical-bond current, i.e., between site i,j and site $i,j+1$.

There is a technical subtlety involved in defining a current operator whose real-space representation is the bond operator of Eq. (16). The standard expression for the current density operator for the continuum Schrödinger equation is

$$\begin{aligned}\mathbf{j}(\mathbf{x}) &= e[n_{\rm op}(\mathbf{x})\mathbf{v}_{\rm op} + \mathbf{v}_{\rm op}n_{\rm op}(\mathbf{x})]/2 \\ &= \frac{e}{2i\hbar}\{n_{\rm op}(\mathbf{x})[\mathbf{x}_{\rm op},H] + [\mathbf{x}_{\rm op},H]n_{\rm op}(\mathbf{x})\}. \end{aligned}\tag{17}$$

We have used the commutator expression for the velocity operator $\mathbf{v}_{\rm op}$, and $\mathbf{x}_{\rm op} = \sum_{i,j}\mathbf{x}(i,j)|i,j\rangle\langle i,j|$ is the position operator. However taking matrix elements of the operator in Eq. (17) in our lattice Hilbert space will not produce the bond current of Eq. (16); instead it yields a site current operator which can be thought of as the average of the bond current on adjacent links.

The bond current operator can be obtained from the following definition. In a discrete Hilbert space it is always possible to define a new pair of Hermitian operators by the following procedure: decompose the Hamiltonian operator into three parts, $H = H^D + H^A + H^B$. This denotes that the Hamiltonian matrix should be split up into a diagonal (D) piece, a piece which is only nonzero above (A) the diagonal, and a piece that is only nonzero below (B) the diagonal. Then using the commutator definition, it is natural to split the velocity operator into $\mathbf{v}^A_{\rm op}$ and $\mathbf{v}^B_{\rm op}$ ($[\mathbf{x}_{\rm op}, H^D] = 0$). With these, the current density operator can be split into two separate Hermitian operators:

$$\begin{aligned}\mathbf{j}^A(\mathbf{x}) &= e[n_{\rm op}(\mathbf{x})\mathbf{v}^A_{\rm op} + \mathbf{v}^B_{\rm op}n_{\rm op}(\mathbf{x})]/2 , \\ \mathbf{j}^B(\mathbf{x}) &= e[n_{\rm op}(\mathbf{x})\mathbf{v}^B_{\rm op} + \mathbf{v}^A_{\rm op}n_{\rm op}(\mathbf{x})]/2 .\end{aligned}\tag{18}$$

These are Hermitian because $\mathbf{v}^{A\dagger}_{\rm op} = \mathbf{v}^B_{\rm op}$. The bond current operator of Eq. (16) is obtained from these operators, using the lattice definitions for $n_{\rm op}$ and $\mathbf{x}_{\rm op}$.

Thus, the current density is obtained as a current pattern on a grid analogous to a resistor network. To calculate the current streamlines as shown in the figures, one more piece of general theory is useful: Given a two-dimensional (2D) vector field $\mathbf{j}(\mathbf{x})$ which is divergenceless, it is easy to show that the vector field $\hat{\mathbf{z}} \times \mathbf{j}(\mathbf{x})$ is curl-free. Such a vector field can be written as the gradient of a scalar field:

$$\nabla\phi(\mathbf{x}) = \hat{\mathbf{z}} \times \mathbf{j}(\mathbf{x}) . \tag{19}$$

Then the contours of $\phi(\mathbf{x})$ are the streamlines of $\mathbf{j}(\mathbf{x})$. To compute ϕ on the lattice from Eq. (19), we set up a discrete version of the line integral, noting that $\phi(\mathbf{x})$ is most naturally defined on the *plaquettes* of the original lattice.

III. CLASSICAL RESULTS

Because of the absence of interference and the resulting fluctuations, and the absence of effects due to modal quantization, the classical results are smoother and cleaner than those of the quantum calculation. We start by presenting these classical results in order to establish the general characteristics of the various structures that we study. As emphasized in the Introduction, while the qualitative behavior of the classical and quantum results agrees, there are substantial differences between the two which will be studied in Secs. IV and V.

A. Resistance traces

We start by presenting our results for the Hall resistance and bend resistance from the classical billiard-ball model and use this to introduce the four classes of structures that we have studied.[56] Three of these classes involve confinement by infinite hard-wall barriers. For these cases, the Fermi energy enters the classical problem only in determining the speed of the particles and can easily be scaled out[2] to yield curves appropriate for all energies. For free electrons (parabolic dispersion) in a structure where the leads have width W (independent of energy for hard walls), we measure resistance in units of $R_0 = (h/e^2)\pi/k_F W$ and use $B/B_0 \equiv \omega_c W/v_F = W/\ell_c$ for the magnetic field, where ω_c (ℓ_c) is the cyclotron frequency (length) and k_F (v_F) is the Fermi wave vector (velocity). In these units, the classical two-dimensional

result is $R_H/R_0 = (2/\pi)B/B_0$. To compare our curves with experimental results, R/R_0 should be multiplied by the number of modes contributing, $k_F W/\pi$, which is convenient since this is experimentally accessible. For a typical experiment with four transverse modes each of which has a spin degeneracy of two, $R_0 \approx 3.3$ kΩ. For the field scale, an estimate of the width of the wire and the density of electrons is needed; $W \approx 200$ nm and $n_{2D} \approx 3 \times 10^{11}$ cm^{-2} yields $B_0 \approx 460$ mT.

Our first class of structures consists of junctions formed by four hard-wall disks: junctions in which the corners are circularly rounded as in the inset to Fig. 5.[33,57] The Hall resistance and bend resistance in Fig. 5 show a variety of deviations from the two-dimensional behavior even in this simple geometry. As the radius of curvature increases, the low-field Hall resistance ($B/B_0 < 0.1$) shows a progression from enhancement ($R_H > R_{2D}$, $R/W = 2$) to quenching ($R_H \approx 0$, $R/W = 4$) to inversion ($R_H < 0$, $R/W = 6$). The deviations are larger in the more gradually rounded structure, in agreement with the collimation idea. The magnitude of the bend resistance at $B = 0$ is about twice the square-corner value for these structures.[33] The enhancement of R_B in rounded corner geometries seems intuitively reasonable since it ought to be harder to force the current around the corner (the appropriate boundary conditions for a bend resistance) when the junction is guiding the current in the forward direction. This picture is confirmed by the striking current density plots presented in Sec. VI (see Fig. 32). The guiding of the electrons around the rounded corner determines the decay of the bend resistance as a function of field;[2] hence, the width of the bend resistance anomaly varies inversely with the turning radius. Note the sign reversal in R_B at fields where R_H is rapidly rising due to incomplete guiding, while R_B is small when R_H reaches the "last plateau" caused by complete guiding.[2] The curves in Fig. 5 certainly illustrate the dependence of the ballistic anomalies on geometry; in fact, the curves are so sensitive to the geometry that quenching behavior is not particularly robust or generic in these structures,[57] representing merely one point in a progression from enhancement to inversion as R/W increases.

The second class of structures we study has hard-wall confinement but linear widening of the wires near the junction. The rate of widening can be varied, yielding either an abruptly widened structure in which the slope of the widening is 1, or a gradually widened structure with slope $\frac{1}{4}$ (insets to Fig. 6). The gradually widened structure shows quenching of the Hall resistance and an especially large value of the bend resistance, in contrast to the abruptly widened structure. Both the quenching and the enhanced bend resistance are consistent with the presence of collimation in the gradually widened structure. In the last part of this section, we will see that the forward-enhancement mechanism is substantial in this structure; this forward enhancement explains why the bend resistance is larger in this structure than in any other structure we study. Note also the weak periodic structure produced presumably by skipping orbit "resonances."[2] In contrast to the case for the four-disk structures, the quenching behavior of the gradually widened structures is relatively robust as discussed in connection with our

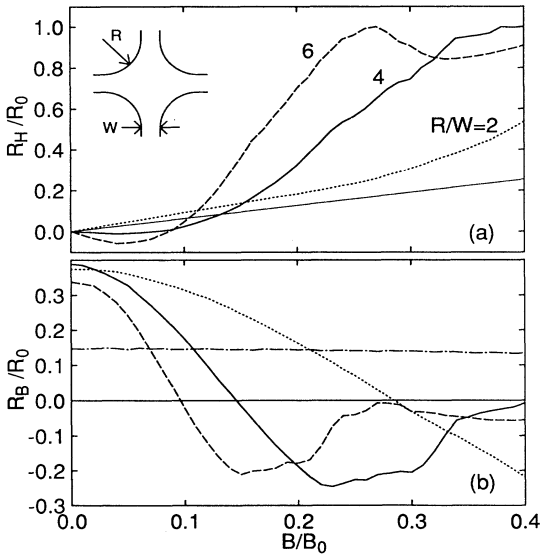

FIG. 5. (a) Hall resistance and (b) bend resistance calculated classically as a function of magnetic field for three four-disk structures (inset). R/W=2 (dotted), 4 (solid), and 6 (dashed) produce linear, quenched, or inverted Hall behavior, respectively, compared to the two-dimensional result (fine solid). The bend resistance decays much more rapidly than that for the square hard-walled junction (dash-dotted). $R_0 = (h/e^2)(\pi/k_F W)$, $B_0 = mcv_F/eW$.

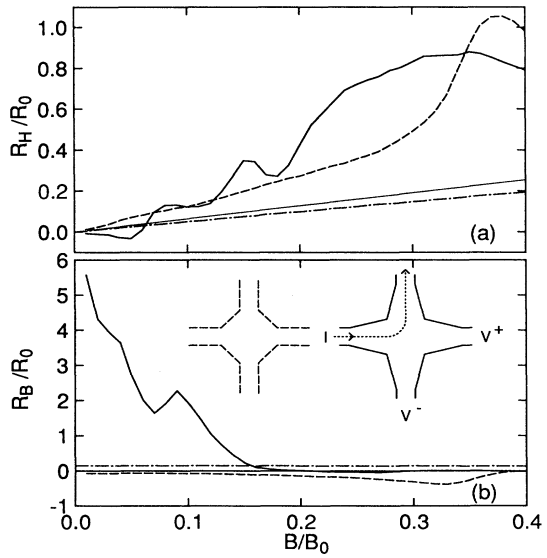

FIG. 6. (a) Hall resistance and (b) bend resistance calculated classically as a function of magnetic field for two hard-wall linearly widened structures. The gradually widened junction (solid) shows quenching and a very large bend resistance compared to both the abruptly widened case (dashed) and a square-corner hard-walled junction (dash-dotted). The inset to (b) shows the two structures—gradually widened (solid) and abruptly widened (dashed)—as well as the lead configuration which defines the bend resistance.

quantum results below.

For our third class, we study structures in which the trajectories are unquestionably very complicated but for which collimation is definitely absent: concave cavities formed by removing a quarter circle from each corner of the junction (inset to Fig. 7). This structure is similar to the stadium billiard, an intensively studied fully chaotic billiard.[58] Nonetheless, both the Hall resistance and the bend resistance, Fig. 7, are close to the two-dimensional values in all three structures despite the complex classical dynamics of the system. This shows clearly that chaotic dynamics alone is not sufficient to cause anomalies in the classical transport coefficients; it also strongly supports our view that collimation is essential for the appearance of all the anomalies.

Fourth, we consider a class of potentials with soft rather than hard walls. We let the potential in the junction region have the form $x^n y^n$ (n=2, 4, and 6) and match this onto a form x^n in the leads [Figs. 8(c)–8(e)]. The strength of the potential is chosen so that the equipotential contour at the highest energy considered widens by a factor of 2 in going from the lead to the interior of the junction. Notice the equipotentials have the same form for all three structures; only the steepness of the confining wall varies with n. In these soft-wall structures, the energy of the particles can no longer be scaled out. We continue to remove the trivial effect of changes in energy by scaling the resistance by the injected flux and using an effective wire width to scale the magnetic field so that the two-dimensional slope remains $2/\pi$.[59] As in the hard-wall structures, to obtain resistance in real units multiply by h/e^2 divided by the number of modes; the magnetic field must be converted using an approximate width of the wires.

Figure 8 shows that quenching does occur in these structures and is enhanced by soft-wall confinement. As in the four-disk class, we see the strong influence of geometry—the behavior of R_H changes from linear (n=6) to quenching (n=4) to inversion (n=2). While the sensitivity to geometry is somewhat less than in the four-disk case, the character of the anomaly in R_H, and in particular quenching, is still not robust. This qualitative conclusion is valid for other energies, though the details of the resistance traces change slightly. In particular, the relative width of the anomalies in R_H and R_B changes with energy: at lower energy for n=2 (dash-dotted lines) the field at which R_H becomes positive is approximately equal to that at which R_B becomes negative, but at higher energy (solid line) the bend resistance is more than a factor of 2 wider. This curious energy dependence has been noted experimentally.[31]

In summary, from our classical resistance calculations, we find that (1) gradual widening is essential for quenching (four-disk and linearly widened structures), (2) complicated dynamics is not sufficient to produce magneto-

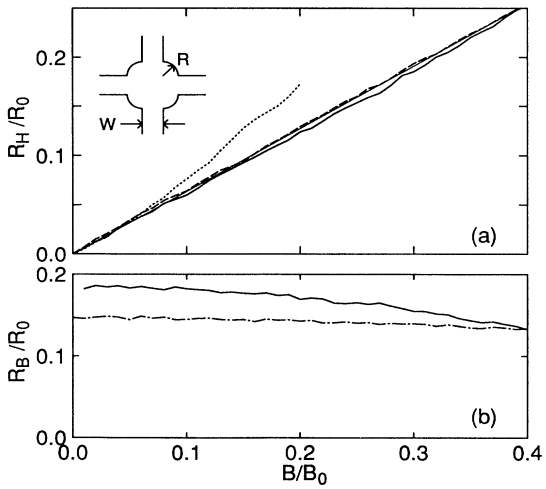

FIG. 7. (a) Hall resistance and (b) bend resistance calculated classically as a function of magnetic field for three concave-cavity structures. R/W=0.7 [solid, inset to (a)], 1.0 (dashed), and 4.0 (dotted). Though many scrambling trajectories are present, R_H and R_B are close to the two-dimensional [light solid in (a)] and square hard-wall junction [dash-dotted in (b)] behavior.

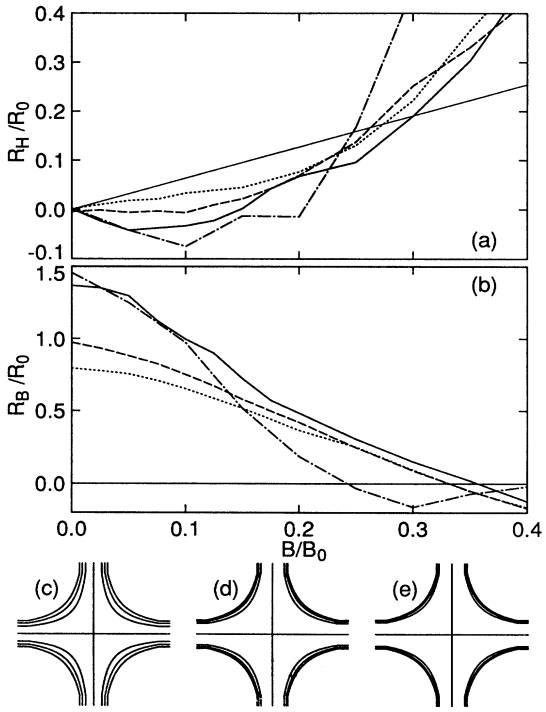

FIG. 8. (a) Hall resistance and (b) bend resistance calculated classically as a function of magnetic field for three soft-wall structures with potential contours in panels (c)–(e). For three traces, the potential has the form $x^n y^n$ with (c) n = 2 (solid), (d) n = 4 (dashed), and (e) n = 6 (dotted) and the energy of the particles is such that the equipotential at E_F widens by a factor of 2 (approximately the highest contour shown). For the fourth trace (dash-dotted), n = 2 and the energy is 0.3 of the energy for the solid curve. A hard wall inhibits quenching and decreases the bend resistance. At the lower energy (dash-dotted) the width of the quenching and bend resistance regions are about the same, but at higher energy (solid) the quenching region is smaller than the region of substantial R_B.

transport anomalies (concave cavity structures), and (3) soft-wall confinement enhances Hall resistance anomalies. The classical results are very sensitive to geometry[57] and rarely produce robust quenching behavior. In this section we have not discussed the role of the amount of widening, as distinguished from the rate, but treat this issue in connection with the quantum results below.

B. Trajectory length analysis

Using the classical results, we now investigate the mechanism producing the Hall and bend resistance anomalies in these structures. As summarized in the Introduction, one aspect of the controversy concerning the quenching of the Hall resistance is whether particles which spend a long time in the junction region are crucial—our interpretation of the "scrambling" mechanism of quenching advocated in Ref. 2. The classical calculations provide a straightforward way of checking the role of scrambling trajectories (see Fig. 4) since one can analyze the Hall and bend resistances in terms of the length of the trajectories. We carry this out by calculating transmission coefficients using only trajectories less than a given length L_T.[33] Using these transmission coefficients to find resistances (note that the current conservation sum rules on the transmission coefficients are still satisfied[60]), we plot R_H and R_B as a function of L_T in Figs. 9–12.[56] The direct straight-through length of the junction, L_D, serves to normalize the trajectory length. An alternate way to perform the analysis is to include all trajectories with fewer than a certain number of collisions

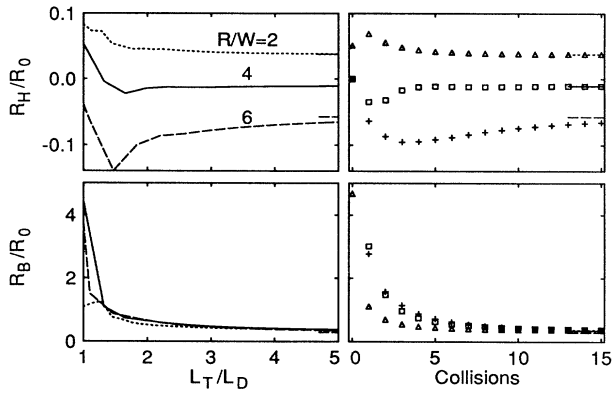

FIG. 9. Hall resistance (upper panels) and bend resistance (lower panels) calculated classically as a function of length of trajectory L_T and number of collisions for three four-disk structures (inset to Fig. 5). For R/W=2 (dotted, triangles), 4 (solid, squares), and 6 (dashed, pluses), the resistances converge quickly to their full value (tick marks on right) showing that short trajectories produce the deviations from two-dimensional behavior. For R_H, $B/B_0 = 0.04$ while for R_B, $B = 0$. Curves are obtained by including all trajectories up to length L_T or having no more than a given number of collisions in the calculation of the transmission coefficients and hence the resistances. L_T is scaled by the direct length, $L_D = 2R + W$, for transmission straight through the structure. $R_0 = (h/e^2)(\pi/k_F W)$, $B_0 = mcv_F/eW$.

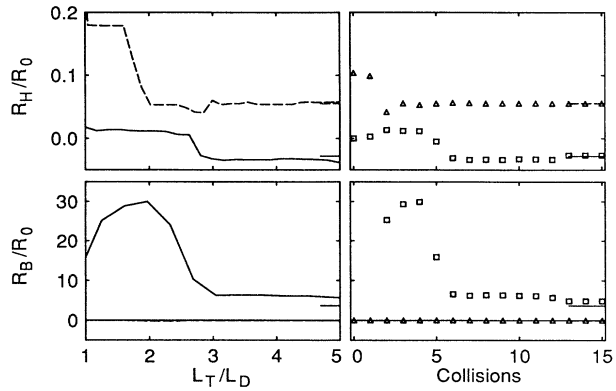

FIG. 10. Hall resistance (upper panels) and bend resistance (lower panels) calculated classically as a function of length of trajectory L_T and number of collisions for two hard-wall linearly widened structures (insets to Fig. 6). The gradually (abruptly) widened case is shown in solid and squares (dashed and triangles). Short trajectories produce the qualitatively different behavior in these two structures. Curves are obtained as in Fig. 9, $B/B_0 = 0.04$ for R_H, and $B = 0$ for R_B.

with the walls in the the transmission coefficients; these results are also shown in the figures. In either case, the value of the resistance converges to its full value as more and more trajectories are included. If long trajectories cause quenching, plots of this type should show lack of quenching for short lengths changing over to quenching as longer and longer trajectories are added to the calculation.

For the four-disk geometry, we show results in Fig. 9 for B/B_0=0.04 at which the behavior of the three different structures is qualitatively different: R_H is enhanced for $R/W = 2$, near zero for $R/W = 4$, and negative for $R/W = 6$. It is clear that this qualitative behavior is well established by including $L_T/L_D < 1.5$ or up to three collisions. For comparison, the mean number of collisions in these structures is approximately 3, 6, and 9 for $R/W = 2$, 4, and 6, respectively. The bend resistance also converges quickly, though not quite as fast as the Hall resistance. Longer trajectories modify the

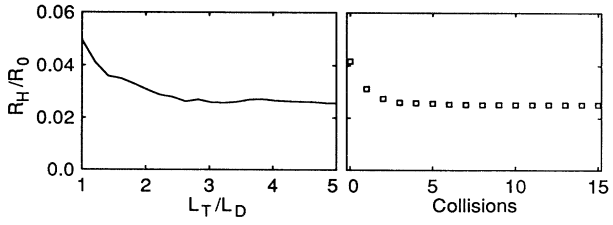

FIG. 11. Hall resistance calculated classically as a function of length of trajectory L_T and number of collisions for a concave-cavity structure (R/W=0.7, inset to Fig. 7). R_H converges quickly showing that short trajectories produce the basic behavior even in this case where there are many scrambling trajectories. Curves are obtained as in Fig. 9, $B/B_0 = 0.04$ for R_H, and $B = 0$ for R_B.

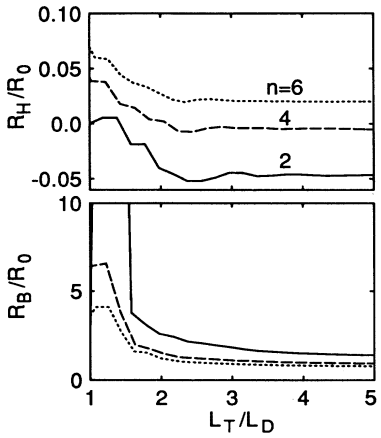

FIG. 12. Hall resistance (upper panel) and bend resistance (lower panel) calculated classically as a function of length of trajectory L_T for three soft-wall structures, $n = 2$ (solid), $n = 4$ (dashed), and $n = 6$ (dotted) [Figs. 8(c)–8(e)]. E_F is chosen so that the equipotential at E_F widens by a factor of 2. While convergence is slower than in the hard-wall cases, short trajectories produce the basic behavior, namely enhanced deviations in softer potentials ($n = 2$). Curves are obtained as in Fig. 9, $B/B_0 = 0.052$ for R_H, and $B = 0$ for R_B.

short-trajectory behavior quantitatively, in the direction of quenching for R_H, but it is clear that quenching in four-disk structures is a short trajectory phenomenon: long scrambling trajectories are not important.

The conclusion from the four-disk structures holds true as well for the linearly widened structures in Fig. 10. Here the convergence is somewhat slower than for the four-disk structures, but the difference between quenching for the gradually widened structure and positive R_H for the abruptly widened structure is established by $L_T/L_D = 2$. Trajectories with more collisions seem to be important in these structures, especially in the bend resistance,[32] perhaps because of trajectories with many collisions in progressing down a given lead.

The concave cavity structure produces many complicated trapped trajectories, and thus one might expect a scrambling mechanism for quenching to be especially effective. However, Fig. 11 shows that the Hall resistance in this geometry ($R/W = 0.7$) converges rapidly as a function of length or number of collisions to its full value.

Finally, we check whether these conclusions hold in soft-wall potentials. It has been suggested that the scrambling mechanism for quenching should be more effective in potentials with soft rather than hard walls.[2] We choose a field ($B/B_0 = 0.052$) for which R_H in the $x^n y^n$ potentials is qualitatively different for n=2, 4, or 6. Figure 12 shows that this qualitative difference is established by $L_T/L_D = 2$ and practically converged by $L_T/L_D = 3$. While this is a somewhat slower convergence than for the four-disk structures, clearly it is short trajectories, not scrambling trajectories, that are determining the qualitative behavior of these structures. We find no evidence for the importance of long scrambling trajectories in any of the structures we have examined.

Recent experiments[32] have addressed the role of scattering in microjunctions by studying the dependence of the ballistic anomalies on density in structures of various shapes. The authors use the variation of the mean free path with density to probe the connection between the resistance anomalies and the degree of ballistic transport. Because the transport mean free path is long in these structures, the implication is that long trajectories are important in causing the anomalies, perhaps through the scrambling mechanism. However, the failure of scrambling to appear as an important mechanism for quenching in any of the structures we have studied reduces the likelihood that it is important in these experiments. We therefore suggest an explanation for the results of Ref. 32 based solely on short trajectories.[61] The important point is that the short-path explanations that we advocate depend on structure in the momentum distribution (collimation) and thus will be degraded by all scattering events rather than just the backscattering events that degrade the current. The fact that the total mean free path is typically[12,32] an order of magnitude less than the transport mean free path in heterostructure devices means that our short-trajectory point of view is completely consistent with the experimental trends as a function of density and the magnitude of the mean free path in Ref. 32.[61]

C. Asymmetry analysis

A second issue in discussing the mechanism for quenching of the Hall resistance is whether a simple enhancement of the forward transmission, a "magnitude effect," or a more subtle suppression of the asymmetry between left- and right-turning trajectories, an "asymmetry effect," is more important. Following the approach of Ref. 3 summarized in the Introduction, we write R_H in terms of the normalized asymmetry α and the total turning probability T_{RL} as in Eq. (6). By combining square-corner and rounded-corner results, we define two quantities designed to evaluate the importance of magnitude or asymmetry effects. $R_1 \equiv \alpha_{\text{rounded}}(T_{RL}/\tilde{D})_{\text{square}}$ includes only the effect of rounded corners on asymmetry and hence evaluates the effectiveness of this mechanism; $R_2 \equiv \alpha_{\text{square}}(T_{RL}/\tilde{D})_{\text{rounded}}$, on the other hand, includes only the effect of rounded corners on the magnitude of T_{RL}. The denominator $\tilde{D}$ is nearly insensitive to where the particles go for the cases studied here. Note that only the normalized asymmetry enters into the expressions for R_1 and R_2 so that these "resistances" correspond to changes in the transmission coefficients which are consistent with the current-continuity constraints. By comparing traces of R_1 and R_2 to the true R_H, one can evaluate the importance of the different mechanisms.

Figure 13 shows traces of R_1 and R_2 for three different structures. In the four-disk structure with $R/W = 4$, R_1 is identical to R_H at low fields; deviations only become apparent in the rapidly rising part. Similar results hold for $R/W = 2, 6$ (not shown). Thus, suppression of asymmetry plays the dominant role in these structures.

In contrast, the traces for the gradually widened structure and the soft-wall $n = 2$ structure show that both the magnitude and asymmetry effects are large. Similar results hold for the n=4 and 6 structures (not shown). The magnitude effects act to moderate the extremely anomalous R_1 traces.

Thus, we conclude that the balance between magnitude effects—mostly enhancement of the forward transmission at the expense of the turning transmission—and asymmetry effects depends on the geometry. In the four-disk systems, where only the asymmetry effect seems to be present, the qualitative behavior is rather sensitive to R/W and the Hall resistance varies continuously from positive to negative with increasing R/W with no substantial interval of nearly zero value at low fields. In contrast, other structures produce quenching that is much less sensitive to geometry changes and persists over a substantial parameter range. Asymmetry effects appear to be essential in producing anomalies, but stable suppression of the Hall resistance over many geometries is greatly aided by the magnitude effects.

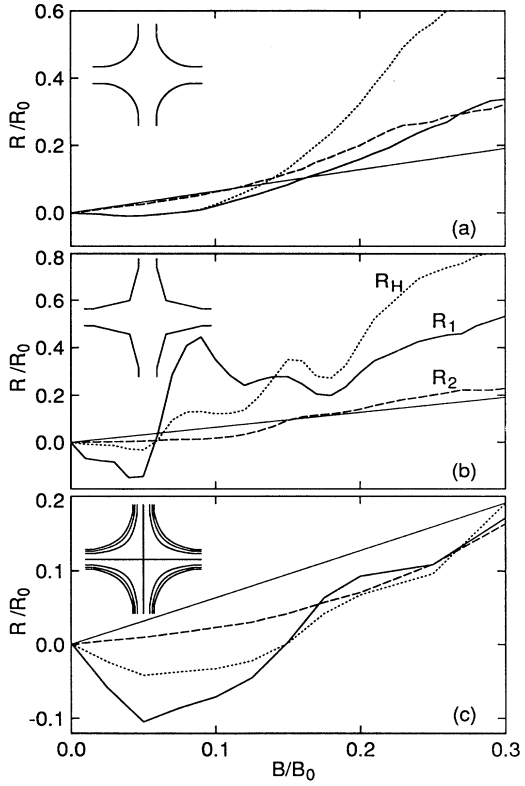

FIG. 13. Classical resistances to analyze asymmetry vs magnitude effects in the Hall resistance for three structures: (a) $R/W = 4$ four-disk structure, (b) gradually widened structure, and (c) $n = 2$ soft-wall structure (with E_F as in Fig. 8). R_1 (solid) uses the asymmetry from the rounded junction with the magnitude from the square junction, R_2 (dashed) is the opposite, the true Hall resistance is the dotted line, and the 2D result is the fine solid line. For the four-disk case, R_1 is a better match to R_H showing that the suppression of asymmetry dominates in these structures, while both R_1 and R_2 play a role in the other two structures. Asymmetry effects appear to be essential, but stable suppression of R_H is aided by suppression of the total-turning probability. $R_0 = (h/e^2)(\pi/k_F W)$, $B_0 = mcv_F/eW$.

IV. QUANTUM RESULTS: FIELD-ENERGY AVERAGING

We study the quantum properties of the same structures that we have studied classically and find similarities in some respects but surprising differences as well. Most important, as discussed in the Introduction, the quantum transmission for all of these structures shows fluctuations as a function of energy or magnetic field caused by interference between trapped trajectories.[38] We average over these fluctuations in order to compare the classical resistances with an "average" quantum resistance. This type of average is well known in connection with disordered systems, and we ask the reader to recall the ergodic hypothesis for such systems:[62] the statistical properties of the resistance fluctuations (mean and variance, for instance) are taken to be independent of the control parameter producing the fluctuations, whether it be energy, magnetic field, or impurity configuration. Thus, averaging over one quantity (field, say) reveals the smooth average behavior as a function of another quantity (energy, say).

In our ballistic structures, it is clear that the ergodic hypothesis does not hold on sufficiently large energy scales. This is illustrated by the plots of the energy dependence of the slope of R_H at $B = 0$ in Fig. 2, which are for "square junctions" in which no trapping and hence no long classical paths are possible. The nonmonotonic structure here is due to the discrete modal structure, and is clearly occurring on scales of order the subband spacing. The scale of the fluctuations in transport coefficients as a function of energy found in graded structures is 1–2 orders of magnitude smaller and is related to the trapping time[38] not modal quantization. Thus we believe that the ergodic hypothesis holds approximately on this more restricted energy scale, and similarly over intervals of magnetic field much less than that needed to produce Hall quantization in these more complex junctions. We use this idea in developing two different averaging techniques in which we average some variables in order to produce the smooth average behavior as a function of another. We note that we do not regard the nonmonotonic structure found in Fig. 2 as fluctuations as they are rather generic (note the similarity between the results for hard-wall and harmonic leads), and instead regard this as part of the quantum average behavior whose analogue should be revealed after averaging in the more complex junctions.

Our first averaging technique, field-energy averaging, consists of convolving the transmission coefficients with the derivative of the Fermi function at temperature T and then averaging the resulting resistances in an interval of magnetic field. The convolution with the Fermi function incorporates some of the effects of a nonzero temperature present in the experiments, while the average over magnetic field is done in the spirit of the ergodic hypothesis and is meant to reveal the typical behavior at a fixed en-

ergy at low field. A typical T=0 trace, $R_H(B)$, shown in Fig. 1 illustrates the character of the magnetic-field fluctuations involved in this average. For the magnetic field, we continue to use the units suggested by the classical calculation in order to remove trivial scaling effects; typically the magnetic-field interval is from $B = 0$ to $B/B_0 \approx 0.1$ or 0.2. For the energy, the quantum problem has a natural unit of energy, namely, the threshold energy of the lowest subband, E_1; T ranges from values less than E_1 to several E_1 depending on whether we are concentrating on specific or general behavior. We first illustrate the dependence of the Hall resistance averaged in this way, $\overline{R}_H$, on geometry in the quantum case and then discuss how the quantum results differ from the classical results.

A. Geometry dependence

The average Hall resistance for the four classes of structures is shown in Figs. 14, 16–18 as a function of energy for relatively high temperature.[63] $\overline{R}_H(E)$ is normalized to the two-dimensional value to clearly show the geometry dependence.

For the linearly widened structures, Fig. 14, the qualitative results are that the gradually widened structure shows a very robust quenching region while the abruptly widened structure does not, as in the classical calculation. In addition we show the results for a square cavity (no Hall-effect quenching) and a structure with gradually widened leads and flattened corners—a strongly inverted (i.e., negative) Hall resistance. This latter structure, which we shall call the "adiabatic-rebound structure,"

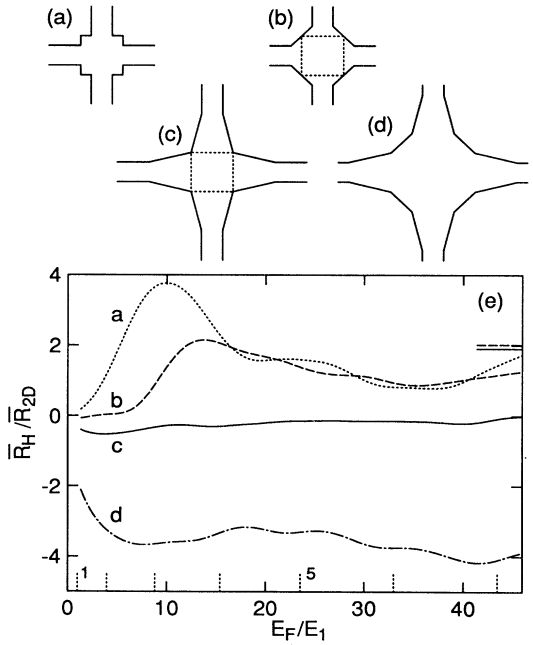

FIG. 14. Average quantum R_H near $B = 0$ normalized to the 2D value as a function of energy for the four structures shown. Gradual widening produces large deviations from the 2D behavior. The dotted ticks mark subband thresholds in the narrow region where E_1 is the threshold of the lowest subband. Curves are obtained by convolving with $(-\partial f/\partial\varepsilon)$ for a temperature of $2E_1$ (which corresponds to 3.2 K for W=200 nm) and then averaging $R_H(B)$ in the range $B/B_0 \leq 0.15$. Ticks on the right mark the classical result averaged in the same interval for structures (b) and (c). The dotted lines in (b) and (c) show an inscribed square whose side is twice the width of the leads.

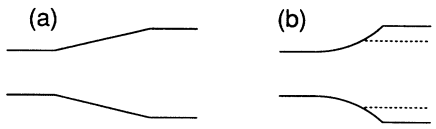

FIG. 15. Schematic of the horn used in testing the adiabaticity of (a) the gradually widened junction and (b) the R/W=2 four-disk junction. In (b), the dotted lines indicate widening of a factor of 1.5 while the solid lines show the full widening of about 2.2.

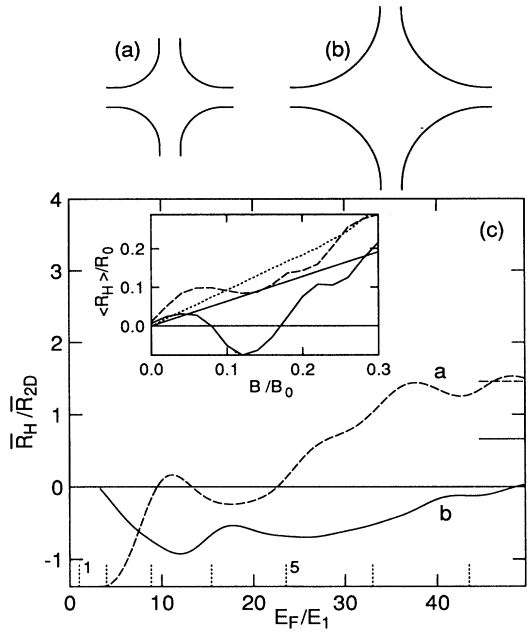

FIG. 16. Average quantum R_H near $B = 0$ normalized to the 2D value as a function of energy for the four-disk structures shown [R/W=2 in (a), R/W=4 in (b)]. The more gradually widened case, (b), shows robust quenching behavior while the more abrupt structure, (a), shows deviations at low energies but 2D behavior at higher energies. The dotted ticks mark subband thresholds in the narrow region where E_1 is the threshold of the lowest subband. Curves are obtained as in Fig. 14. Ticks on the right mark the classical result averaged in the same interval. The inset shows $\langle R_H(B) \rangle$ obtained by a weak impurity average for structure (a) at $E_F/E_1 = 19.5$ (solid) and 35 (dashed). The dotted line is the classical result, and the straight solid line is the 2D result. Comparing these traces to $\overline{R}_H$ at the appropriate energy in the main figure, we see that both averaging methods give the same behavior. The traces indicate that the deviations from 2D behavior are caused by distinct oscillations. $R_0 = (h/e^2)(\pi/k_F W)(mv_F/\hbar k_F)$, $B_0 = mcv_F/eW$.

is patterned after the experimental structures of Ford *et al.*;[22] note that *both* a gradual widening and flattened corners are essential in producing inversion. These results are consistent with the underlying importance of collimation in producing quenching: trapping or widening at the junction is insufficient in itself, sufficiently gradual widening being the key. In fact, the presence of collimation in this structure is directly demonstrated in the quantum regime in Sec. VI. In any transport measurement a distribution of particles is injected. From a classical point of view, the role of collimation in the adiabatic-rebound structure is to enhance the contribution of those special trajectories[22] which "rebound" into the wrong lead [see Fig. 4(b)]. Such trajectories are also present in the abruptly widened structure, but other trajectories (not present with gradual widening) render the rebound trajectories ineffective. For instance, a particle from the left which rebounds at $B=0$ into the upper lead but is bent into the lower lead at $B \neq 0$ is certainly present in the abruptly widened case but may not be present once gradual widening has produced collimation.

In the linearly widened structures, it is straightforward to study the effects of the rate of widening and the total amount of widening. In Fig. 14, the total amount of widening for both the gradually and abruptly widened structures is a factor of 2: the side of a square inscribed in the junction is twice the width of the wire. Keeping this total amount of widening constant, we varied the slope and found that while some suppression is present for a slope of $\frac{1}{2}$, quenching requires a slope of $\frac{1}{3}$ and is only robust for slopes approaching $\frac{1}{4}$ as in the gradually widened structure shown. For a constant slope of $\frac{1}{4}$ to ensure good collimation, we varied the total amount of widening and found that quenching requires widening by greater than a factor of about 1.5. This is plausible since direct transmission around a bend is suppressed[2] if the injection cone in $\mathbf{k}$ space of the collimated particles does not overlap in $\mathbf{k}$ space with the acceptance cone of the perpendicular lead. Lack of overlap requires a beam of angular width $\pi/2$ (or less) which occurs for a total widening of $\sqrt{2}$ in the adiabatic approximation, close to our observed 1.5.

In order to characterize the degree of collimation in the quantum calculations, we look at the transmission through a single widening lead connecting two wires of different widths, as shown in Fig. 15. Since collimation is equivalent to a selective population of the low-lying modes in the wide region for transmission from the narrow to the wide region, the amount of current carried by the low-lying modes in the wide region compared to either the amount for a perfectly adiabatic horn or the amount for equipartition among the modes provides a measure of the degree of collimation. To be precise, we calculate

$$f = \frac{\sum_{a=1}^{M_N}\sum_{b=1}^{M_N} T_{ba} - M_N^2/M_W}{M_N - M_N^2/M_W}, \tag{20}$$

where M_N (M_W) is the number of modes in the narrow (wide) wire and the indices on T_{ba} label mode number. This quantity is then averaged over energies for which 3–6 subbands are contributing.[64] For a perfectly adiabatic horn, $f=1$, while for a horn which completely mixes the particles so that the current is distributed equally in all the output modes, $f=0$. For the linearly widened structures with a total widening of 2, $\overline{f}=0.88$, 0.70, and 0.33 for slopes of $\frac{1}{4}$, $\frac{1}{2}$, and 1, respectively, showing that collimation is present in the structure with quenching. In fact for all our structures, we have seen quenching if and only if $\overline{f} \geq 0.85$ for a widening of 1.5 or greater. In some recent experimental work,[32] the junctions do not have this minimum amount of widening yet anomalous behavior in R_H is observed. We emphasize that if the experimental junctions do not include widening by at least a factor of 1.5, none of the conceptual models discussed in this paper will explain the anomalous behavior. Some evidence for such anomalies occurs in two of our structures and will be discussed in the next subsection.

The results for the four-disk structures shown in Fig. 16 are that at energies where there are several subbands, the $R/W = 4$ structure shows quenching while the $R/W = 2$ structure does not, as in the classical regime. While the total amount of widening for $R/W = 2$ is 2.2 so that collimation is in principle possible, the rate of widening is such that the adiabatic part is quite short. We remind the reader that the entire junction cannot be adiabatic as the wall of the structure turns through 90°. In fact, $\overline{f} = 0.59$ for a horn using the full lead of this structure (see Fig. 15); if the lead is cut at a widening of 1.5 so that collimation is tested only up to this point, $\overline{f} = 0.81$ which is still insufficient (barely). For $R/W = 4$ the total widening is very large—3.3—and the extent of the adia-

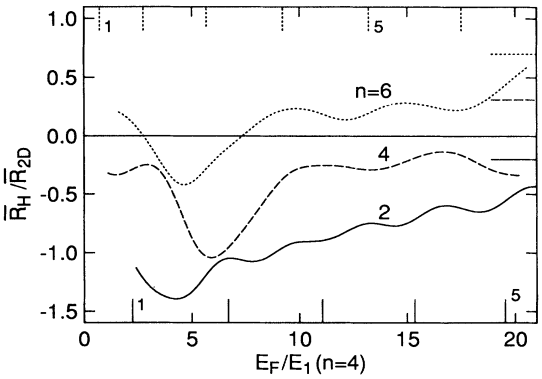

FIG. 17. Average quantum R_H near $B=0$ normalized to the 2D value as a function of energy for three soft-wall structures shown in Fig. 8 ($U \sim x^n y^n$ in the junction). As in the classical results, a soft potential enhances quenching. The solid ticks mark subband thresholds in the $n = 2$ wire while the dotted ticks mark those for $n = 6$. The energy is scaled by the threshold of the lowest subband for $n = 4$. Curves are obtained by convolving with $(-\partial f/\partial \varepsilon)$ for a temperature of $\approx E_1(n = 4) \approx 0.4E_1(n = 2)$ (which corresponds to 4.2 K for W=200 nm at the threshold for the fourth mode in the $n = 4$ case) and then averaging $R_H(B)$ in the range $B/B_0 \leq 0.18$. Ticks on the right mark the classical result averaged in the same interval.

batic region is large enough to produce good collimation. While $\bar{f} = 0.46$ for the full lead, $\bar{f} = 0.86$ if the lead is cut at a widening of 1.5.

As in the classical calculations, a soft-wall potential enhances quenching. Figure 17 shows the results for the $x^n y^n$ potentials with the $n = 2$ results being considerably more anomalous than the $n = 6$ results.[59] The strength of the confinement potential is chosen so that the total widening is about 2 for the highest energies considered. The values of $\bar{f}$ are consistent with collimation: for the total widening $\bar{f}$=0.95, 0.86, and 0.81 for n=2, 4, and 6, respectively.

B. Comparison of quantum and classical results

While at the broadest qualitative level, our quantum and classical results agree, there are important discrepancies between them. First, the region of anomalous behavior (compared to the two-dimensional result) is substantially larger in magnetic field in the quantum calculations and lasts to surprisingly high energies. The magnetic-field window used in the quantum average is from 0 to 0.15 or 0.20, yet the classical region of anomalous behavior is only about 0.1. To show this quantitatively, the classical average Hall resistances (averaged in exactly the same way as the quantum results) appears as ticks on the right axis of Figs. 14–18. In all cases, the classical result averaged in this way lies substantially above the quantum value, in some cases predicting no average quenching when the quantum results are strongly quenched (i.e., in the gradually widened and $R/W = 4$ four-disk geometries). While quantum deviations from the classical results are expected in the extreme quantum limit—one or two modes in the leads—it is surprising that such deviations persist undiminished when five or six modes are contributing, unlike the deviations in the square-corner junctions (see Fig. 2), for instance, which are large only in the regime of one or two modes. In fact, for the gradually widened structure, we performed calculations up to the threshold for the eleventh mode and saw no decrease in the discrepancy between the quantum and classical results. On the other hand, the argument in Appendix B shows that as the number of modes becomes very large and all interference effects are eliminated, the quantum result reduces to the classical one. Our numerical results show, therefore, that average quantum effects remain surprisingly important in the many mode regime in this structure.

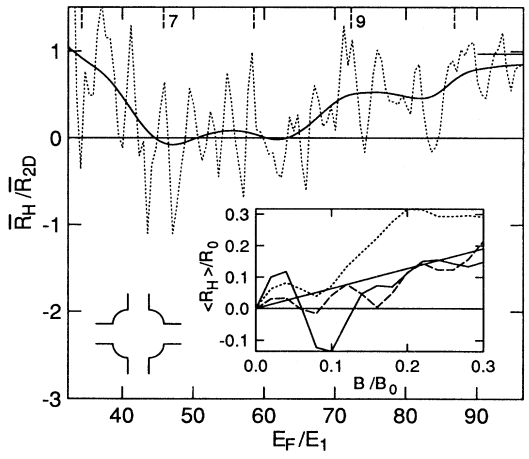

FIG. 18. Average quantum R_H near B=0 normalized to the 2D value as a function of energy for a concave cavity (R/W=0.7, see Fig. 7) at two temperatures: $k_BT = 2E_1$ (solid) and $T = 0$ (dotted). Note the striking deviations from 2D behavior at a relatively high energy (7-8 subbands contributing). The dashed ticks mark subband thresholds in the narrow region where the energy threshold of the lowest subband is E_1. Curves are obtained as in Fig. 14. The tick on the right marks the classical result averaged in the same interval. The inset shows $\langle R_H(B) \rangle$ obtained by a weak impurity average at $E_F/E_1 = 20$ (dotted), 52 (solid), and 80 (dashed). The traces show that the deviations from 2D behavior are caused by oscillations of a distinct period.

A second type of discrepancy between the quantum and classical results are large deviations that occur only in a fixed energy window in certain structures. The two examples of this are the $R/W = 2$ four-disk structure (Fig. 16) and the concave cavity (Fig. 18). Denoting the threshold of the nth mode E_n, we find that the Hall resistance in Fig. 16 is suppressed for energies below E_5 but is close to the classical value for energies above E_6. While the discrepancy is not limited to the extreme quantum limit, it does occur at low energy where quantum effects are expected to be larger. In contrast, the discrepancy in the concave cavity consists of a suppression in the energy range E_7 to E_9 bordered by regular behavior on each side. This feature may be related to anomalous behavior seen in experiments on nominally square-corner junctions.[32] When we discuss the impurity-energy averaged results in the next section, we will see that this feature, as well as that in the $R/W = 2$ four-disk structure, is connected to periodic oscillations in R_H (insets to Figs. 16 and 18) with a periodicity of a quantum of flux through the cavity.

Finally, several structures exhibit discrepancies on a small energy scale, of the order of the subband separation. To demonstrate this effect we use a smaller temperature in the results of Fig. 19 and 20 and show the T=0 results in addition (which are field averaged only).[63] Note the fluctuating T=0 results in all three structures which are especially large in the extreme quantum limit, $E_F < E_3$. For the gradually widened structure [Fig. 19(a)], the energy averaged trace (solid line) has a striking oscillating component up to E_5 and perhaps beyond. This is not a statistical effect from averaging the T=0 fluctuations (increasing the number of energy points produces no change in the amplitude of the oscillations) but rather is fine structure in the *average* quantum resistance. Such fine structure depends sensitively on the geometry: for the $R/W = 4$ four-disk structure in panel (b), there is only one small dip between E_3 and E_4, the other structure being statistically insignificant. Perhaps, the longer trapping time and more random scattering in the $R/W = 4$ four-disk structure obscures the subband effects. The behavior of the $n = 4$ soft-wall structure in

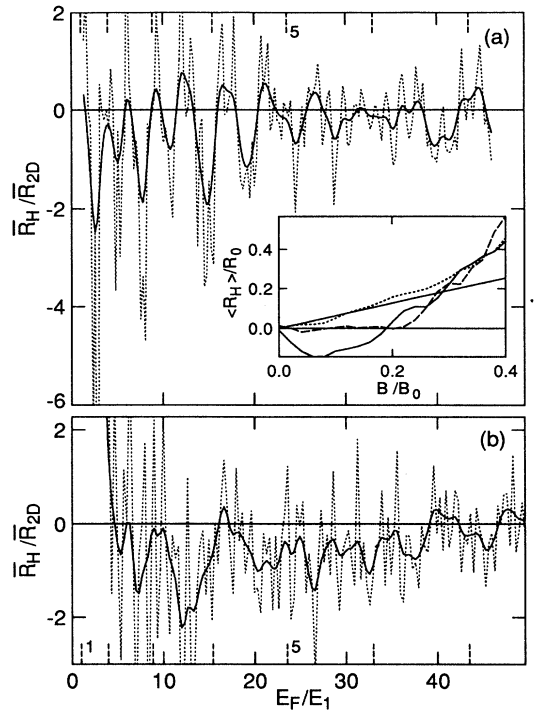

FIG. 19. Average quantum R_H near B=0 normalized to the 2D value as a function of energy for (a) the gradually widened structure [Fig. 14(c)] and (b) the four-disk structure with R/W=4 [Fig. 16(b)]. Two temperatures are shown: $k_BT = E_1/3$ (solid, which corresponds to 0.5 K for W=200 nm) and T=0 (dotted). In the finite temperature traces, pronounced structure within a subband is evident in panel (a) but weaker in (b). The dashed ticks mark subband thresholds in the narrow region where the energy threshold of the lowest subband is E_1. Curves are obtained as in Fig. 14. The inset to (a) shows $\langle R_H(B) \rangle$ obtained by a weak impurity average at $E_F/E_1 = 9.5$ (dotted), 15 (solid), and 23 (dashed). The traces confirm the variation of the Hall resistance behavior within a subband seen in the main figure.

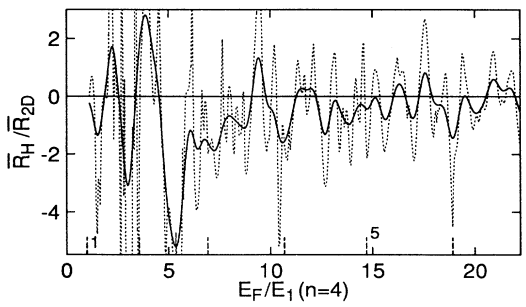

FIG. 20. Average quantum R_H near B=0 normalized to the 2D value as a function of energy for the $n = 4$ soft-wall structure [Fig. 8(d)] at two temperatures [$k_BT = 0.16E_1$ (solid) and $T = 0$ (dotted)]. The dashed ticks mark subband thresholds in the narrow region where the energy threshold of the lowest subband is E_1. Curves are obtained as in Fig. 17.

Fig. 20 is intermediate between these two: there is some very large structure for energies less than E_3 but weak structure for larger energies. The large features at low energy have recently been observed in experiments.[34]

While our calculations of the average quantum resistance clearly show deviations from the classical resistance, we have not been able to identify precisely which paths cause these deviations. As an example of when one can make such an identification, in a disordered system the average quantum resistance differs from the classical resistance through the interference of time-reversed paths, an effect known as weak localization.[65] For the ballistic junctions studied here, since the interference among long paths is eliminated by the averaging, interference on short length scales is certainly responsible. The relation between the classical and average quantum resistance is illuminated by the calculation in Appendix B which is based on the semiclassical expression for the Green function as a sum over classical paths with phase factors. In Appendix B we show that the classical results are obtained when the number of modes tends to infinity ($N \to \infty$) *and* an average of the transmission coefficient is performed over an infinite range of energies.[66] The fact that our calculation is done for a finite number of modes and a restricted interval of energy may explain the deviations from the classical behavior that we see. However, because the size of the entire scattering region is only several wavelengths, a description of the quantum deviations in terms of interference along classical paths may not be possible in this regime.

In summary, we note three types of quantum deviations of R_H in these field-energy averaged results in comparison to the classical results. (1) There is a general enhancement of quenching and anomalous behavior in terms of both magnetic field and energy range. (2) Certain structures exhibit large deviations in a fixed energy window in the middle of a regular region. (3) In some structures, the average Hall resistance shows oscillations as a function of energy on a scale of the order of the subband separation.

V. QUANTUM RESULTS: IMPURITY-ENERGY AVERAGING

While the field-energy averaging used in the last section gives many useful results, one would like to compare directly the magnetic-field dependence of the quantum case to the classical case. In order to extract average quantum traces, we introduce an impurity-averaging method since energy averaging alone is simply not enough. This approach is again motivated by the ergodic hypothesis discussed at the beginning of the last section: the hypothesis is that an average over impurity configurations will establish the mean behavior at a fixed magnetic field, allowing one to study the mean behavior as a function of field. This hypothesis is certainly not true for all parameter ranges since we are interested in ballistic effects which are degraded by impurity scattering, but we empirically show below that this ergodic hypothesis is valid for sufficiently weak impurities.

As discussed in the Introduction, we introduce weak

short-range elastic scattering sites into the junction region (but not the leads). The basic idea is that weak impurity scattering will introduce a sufficient phase change along long trajectories to eliminate the interference effects of these long trajectories after an ensemble average over impurities. On the other hand, the interference between short paths is retained since the total phase change caused by impurities along these short paths is small for all impurity configurations. The impurity average, then, is meant to mimic the phase-breaking processes occurring in experimental structures. Of course, the structures are no longer completely ballistic, and the average resistance of the structure will be modified by an impurity strength that is too large. It is important to establish, then, if an impurity strength exists which will average the fluctuations but not change the typical ballistic behavior. In addition, a small amount of energy averaging serves to smooth the traces further and is physically sensible in terms of incorporating some of the effects of a nonzero temperature.

A. Justification of the method

An example of the results of this averaging technique is given in Fig. 21 which compares ballistic traces at five closely spaced energies to an impurity-energy averaged trace for the $R/W = 4$ four-disk structure [Fig. 16(b)].[63] Since our calculation is always performed on a lattice, it is trivial to include impurity scattering within the Anderson model of disorder: the on-site energies are chosen uniformly from the interval $[-W_D, W_D]$. Such impurities are placed throughout the entire junction, i.e., the region where the walls of the leads are not parallel. These impurities are certainly not meant to be a realistic representation of the impurity potential in these structures but rather a tool for extracting the average quantum behavior. The energy averaging was done using the five energies for which ballistic traces are shown; $W_D = 0.13$ for which the mean free path[21] in the junction in terms of the direct transit length is $\approx 17 L_D$ (averaged over energy).[67] For both the bend resistance and Hall resistance shown, the average trace lies in the middle of the five ballistic traces at all fields. This confirms that the averaging suppresses the large quantum fluctuations while yielding a faithful representation of the typical behavior.

In the absence of energy averaging, we found that quantum fluctuations remained for this impurity strength: the average over disorder was insufficient to bring out the true average behavior. However, for larger impurity strengths, the average trace clearly did not represent the typical ballistic behavior. Thus, an energy average over a narrow interval—one in which the resistance fluctuates but much less than the subband spacing—is essential in revealing the average quantum behavior. On the other hand, similarly smooth traces from only energy averaging require a larger energy window and hence the

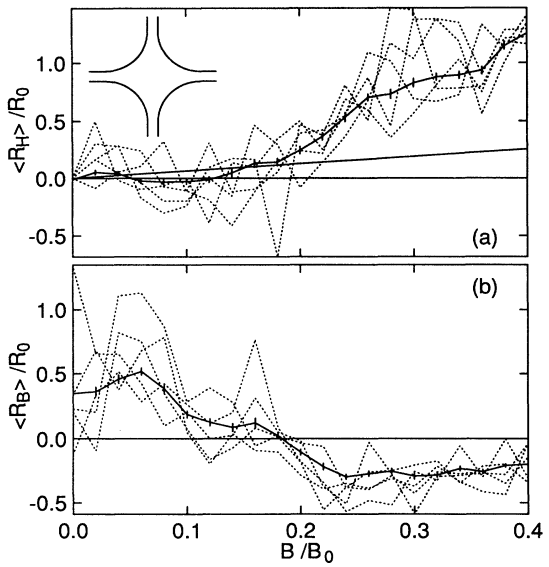

FIG. 21. Quantum calculation of (a) Hall resistance and (b) bend resistance as a function of magnetic field in a four-disk junction with R/W=4 (inset). The solid line results from an average over both weak disorder ($W_D = 0.13$) and $k_F W/\pi$ in the range [4.44,4.56]; the error bars represent the statistical standard deviation. The dotted lines are results without disorder at specific energies in the same range and the light solid line is the 2D result. The averaging suppresses the fluctuations in the ballistic traces and produces a trace showing the typical behavior of the set of ballistic results. $R_0 = (h/e^2)(\pi/k_F W)(m v_F/\hbar k_F)$, $B_0 = m c v_F/eW$.

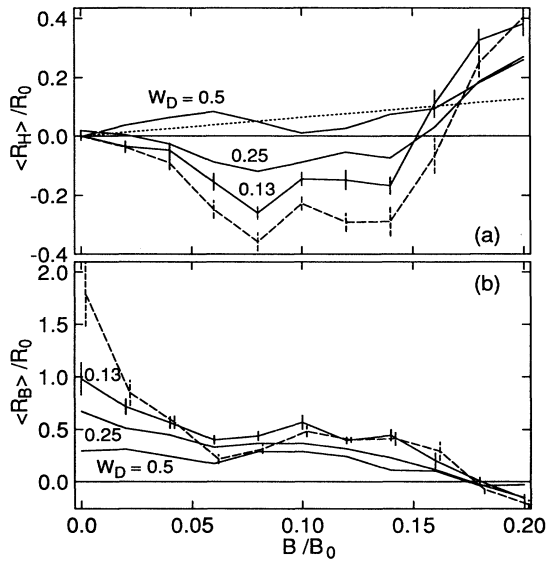

FIG. 22. Quantum calculation of (a) Hall resistance and (b) bend resistance as a function of magnetic field in a four-disk junction with R/W=4. Impurity-energy averaged results (solid lines) using three different strengths of disorder ($W_D = 0.13, 0.25, 0.5$, bottom to top in R_H and top to bottom in R_B) are compared to an energy average without disorder (dashed). For clarity, statistical error bars are shown on only one solid line; the others have comparable errors. The range of energies is $k_F W/\pi \in [4.44, 4.56]$ and the light solid line is the 2D result. Stronger impurity scattering suppresses both the quenching and the bend resistance.

sacrifice of energy resolution. The impurity-energy averaging that we use provides a smooth magnetic-field trace at a relatively well-defined energy; we average over about $\frac{1}{6}$ of the subband spacing in the results shown here.

Figure 22 shows the effect of different impurity strengths: impurity-energy averaged traces for three different strengths are compared to a pure energy averaged trace. Stronger impurity scattering eliminates the transport anomalies:[32] the quenching of the Hall resistance and the magnitude of the bend resistance are both suppressed. The mean free paths for the three cases shown are ≈ 1.2, 4.4, and $17L_D$ for $W_D = 0.5$, 0.25, and 0.13, respectively.[67] The quantum fluctuations and impurity effects are particularly strong for the bend resistance. While weak impurity scattering has a larger effect on R_B than R_H, R_B seems more robust to strong impurity scattering, as indicated in experiments.[32] For the weakest impurity strength, the impurity-energy averaged traces are in qualitative agreement with the purely energy averaged ones.

B. Quantum magnetic-field traces

Figures 23–25 show impurity-energy averaged quantum traces, $\langle R_H(B)\rangle$ and $\langle R_B(B)\rangle$, and classical traces for three of the structures studied in this paper:[63] the $R/W = 4$ four-disk structure (Fig. 23), the gradually widened structure (Fig. 24), and the $n = 4$ soft-wall structure[59] (Fig. 25). The quantum traces mostly show the same qualitative behavior as the classical traces, including, for instance, the very large magnitude of R_B in the gradually widened structure. However, these traces show explicitly the large quantitative differences between the classical and quantum results: the quenching width is substantially larger in both the four-disk structure and the soft-wall structure, and the traces are very different for the gradually widened structure.

In these three figures, quantum traces at three different energies show how the quenching and bend resistance change as the number of modes contributing changes from 3 to 4 to 6. For the four-disk structure (Fig. 23), the bend resistance is largely unaffected while there is a slight narrowing of the quenching region. The linearly widened structure (Fig. 24) is very sensitive to energy, as we noted in connection with Fig. 19 above, showing inversion, quenching, and normal linear behavior of the Hall resistance at these three energies. The bend resistance for this structure is especially large. Finally, for the soft-wall structure, Fig. 25 shows that the quenching region in the Hall resistance becomes narrower (in reduced units) as the energy increases while the bend resistance remains roughly unchanged. This change in the relative width of the ballistic anomaly in R_H and R_B as energy changes is observed in some experimental traces.[31]

The impurity-energy averaged traces provide confirmation for some of the more unusual results obtained using field-energy averaging in the last section. First, the traces $\langle R_H(B)\rangle$ for the gradually widened structure are in good agreement with $\overline{R}_H(E)$ (Fig. 19) at the six energies shown in Fig. 24 and the inset to Fig. 19. Thus the large variation of the quantum average on an energy scale of order the subband spacing is present in both averages. Second, the deviations on a larger energy scale seen in the $R/W = 2$ four-disk structure and the concave cavity are confirmed by the traces in the insets to Figs. 16 and 18, respectively. In both cases, $\langle R_H(B)\rangle$ shows oscillations of a definite periodicity, suggesting that the deviations result from interference of special paths. In the concave cavity, the period is approximately a flux quantum through the area of the cavity. This result is easily understood if one assumes coupling to a single "quantum dot" state, but why such coupling should be particularly effective in the energy range E_7 to E_9 at such low fields remains a mystery.

Using the quantum average traces, we perform the same kind of asymmetry analysis as for the classical results (Sec. III C) in order to determine whether the ballistic anomalies are caused by a decrease of the total-turning probability, which we have been calling a magnitude effect, or by the suppression of the left-right asymmetry. Recall that we write the Hall re-

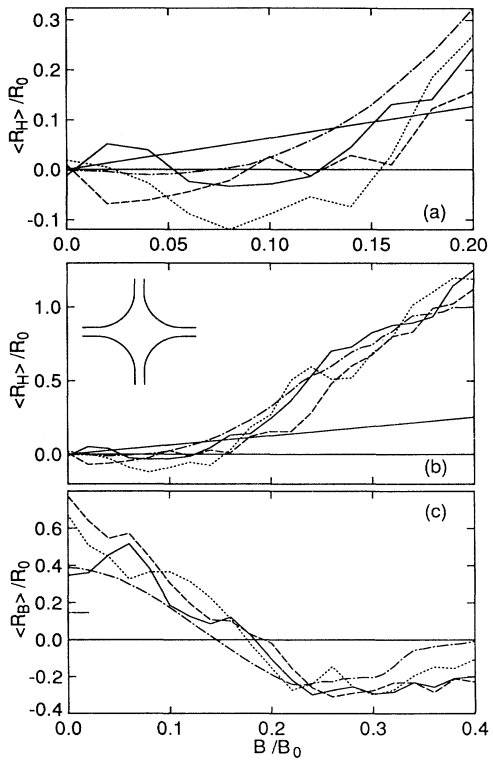

FIG. 23. Quantum calculation of (a), (b) Hall resistance (on two different scales) and (c) bend resistance as a function of magnetic field in a four-disk junction with R/W=4. Impurity-energy averaged results ($W_D = 0.13$) at three energies [$k_F W/\pi = 3.5$ (dotted), 4.5 (solid), and 6.5 (dashed)] are compared to the classical result (dash-dotted) and the 2D result (solid straight line). The region of anomalous behavior is larger in the quantum results than in the classical trace. There is little variation with energy after using reduced units. The solid tick mark in (c) is the value of R_B in a square-corner junction.

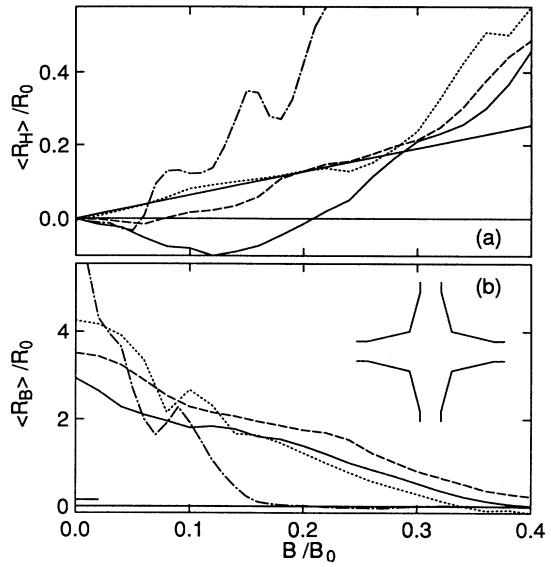

FIG. 24. Quantum calculation of (a) Hall resistance and (b) bend resistance as a function of magnetic field in the gradually widened structure [Fig. 14(c)]. Impurity-energy averaged results ($W_D = 0.13$) at three energies [$k_F W/\pi = 3.5$ (dotted), 4.5 (solid), and 6.5 (dashed)] are compared to the classical result (dash-dotted) and the 2D result (solid straight line). The quantum results are strikingly different from the classical trace and vary substantially with energy (see also Fig. 19). The solid tick mark in (b) is the value of R_B in a square-corner junction.

sistance in terms of the normalized asymmetry and the total-turning probability, Eq. (6), and then combine square-corner and rounded-corner results in defining $R_1 \equiv \alpha_{\text{rounded}}(T_{RL}/\tilde{D})_{\text{square}}$, which includes only the effect of rounded corners on asymmetry, and $R_2 \equiv \alpha_{\text{square}}(T_{RL}/\tilde{D})_{\text{rounded}}$, which includes only the effect of rounded corners on the magnitude of T_{RL}. By comparing traces of R_1 and R_2 to the true R_H, one can evaluate the importance of the different mechanisms.

Figure 26 shows traces of R_1 and R_2 for three different structures. As in the classical calculations (Fig. 13), the suppression of asymmetry dominates in the four-disk structure ($R/W = 4$), the magnitude effect being very small. In contrast, the magnitude effect is substantial in both the gradually widened structure and the $n = 2$ soft-wall structure, also in agreement with the classical results. Similar results hold for all three energies studied ($k_F W/\pi = 3.5$, 4.5, and 6.5, only one shown). It is particularly interesting that the quantum-mechanical effects simply enhance the mechanism which produces the classical ballistic anomalies rather than introducing a different mechanism for the ballistic anomalies.

In summary, we have used the quantum magnetic-field traces $\langle R(B) \rangle$ to make three points about the *average* quantum behavior of these ballistic junctions. (1) The ballistic anomalies in both R_H and R_B are enhanced in the quantum regime compared to the classical regime. (2) The quantum traces vary with energy, quite dramatically for the gradually widened structure and in agreement with experiments for the soft-wall potential. (3) The quantum anomalies are caused by the same balance between asymmetry and magnitude effects as the classical anomalies: asymmetry effects appear to be essential in producing anomalies, but stable suppression of the Hall resistance over many geometries is greatly aided by the magnitude effects.

VI. LOCAL QUANTUM PROPERTIES OF JUNCTIONS

In this section, we present results for the current density $\mathbf{j}(\mathbf{r})$, the charge density $n(\mathbf{r})$, and the quantum phase-space distribution functions $W(\mathbf{r},\mathbf{p})$ (the "Wigner distribution") and $H(\mathbf{r},\mathbf{p})$ (the "Husimi distribution"), to be explained shortly, for the states at the Fermi energy in the types of ballistic cross geometries described above. These functions are primarily tools for visualization; they allow us to understand the spatial structure of electron transport which is responsible for the properties discussed above: the pseudorandom structure

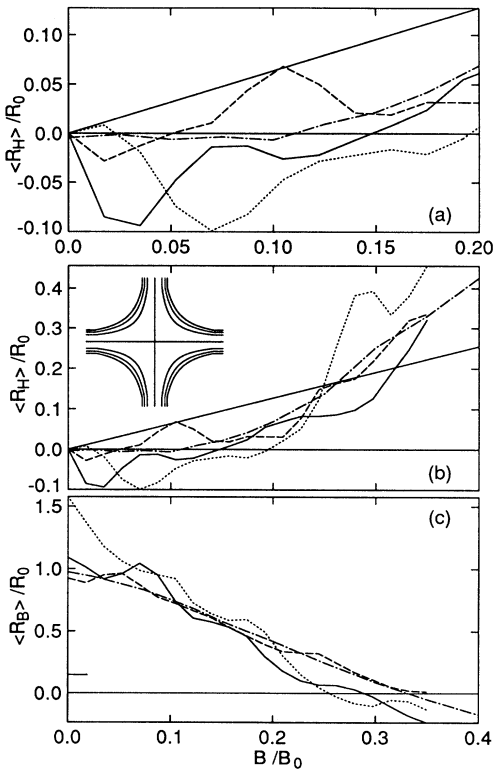

FIG. 25. Quantum calculation of (a), (b) Hall resistance (on two different scales) and (c) bend resistance as a function of magnetic field in the $n = 4$ soft-wall structure. Impurity-energy averaged results ($W_D = 0.13$) at three energies [$k_F W/\pi = 3.5$ (dotted), 4.5 (solid), and 6.5 (dashed)] are compared to the classical result (dash-dotted) and the 2D result (solid straight line). The region of quenching in R_H is substantially larger than in the classical trace and is enhanced at lower energy. The solid tick mark in (c) is the value of R_B in a square-corner junction. $R_0 = (h/e^2)(\pi/k_F W)(mv_F/\hbar k_F)$, $B_0 = mcv_F/eW$.

of the transport coefficients as a function of energy and magnetic field, and the essentially classical phenomena of Hall resistance inversion and quenching. We find that the structure of the scattering states for these low-magnetic-field phenomena is useful in building intuition for the transport problem in the same way that the structure of the edge states has been useful for an intuitive understanding of high-field phenomena (i.e., the integer quantum Hall effect).

To obtain the above quantities, it is necessary to compute the full scattering wave function for states at the Fermi energy. The method of computation of the wave function and the construction of the charge and current densities was discussed earlier in Sec. II C. We want to emphasize the manner in which these charge densities and current densities are to be interpreted. They provide information about the scattering states at the Fermi energy; however, they do *not necessarily* give the correct changes of the local currents and charge densities. The results presented below are an incoherent sum of the current densities (and charge densities) contributed by the scattering states $|n,a\rangle$ for all the propagating modes a at the Fermi energy incident from one of the leads n (call it lead $n=1$):

$$\mathbf{j}(\mathbf{x}) = \mathrm{Tr}[\delta\rho \mathbf{j}_{\mathrm{op}}(\mathbf{x})] \ , \tag{21}$$

$$\delta\rho = (-\partial f/\partial\varepsilon)\sum_a |1,a\rangle\langle 1,a| \ , \tag{22}$$

and similarly for the charge density. $\delta\rho$ is the change in the density matrix when flux is injected into lead 1 at the Fermi energy. The current density of Eq. (21) has a direct physical interpretation in that the integral of this current over the cross section of lead n ($n \neq 1$) is proportional to T_{n1}, a component of the transmission probability matrix in Eq. (1).

In the Landauer-Büttiker theory of conductance, one argues that Eq. (22) is the correct density matrix in linear response,[68] and our calculated charges and currents are assumed to represent the true transport current and induced charge. We note however that Kubo linear response theory obtains a different expression for the density matrix, which leads to the same expression for the conductance coefficients [the T_{jn}'s of Eq. (1)],[6–9] but not, in general, to the same local current charge densities. This is so for two reasons. First, in nonzero magnetic field there is an off-Fermi-surface contribution to the local current density which makes no contribution to the total current through any cross section[9] but would contribute, e.g., to the magnetization. This contribution is definitely absent in our calculations. Second, even at $B=0$, the Kubo and Landauer-Büttiker density matrices differ and we see no obvious reason for both to yield the same local currents and charges (although it has been proved they yield the same total currents). This question requires further study which we will not attempt here; instead we simply use Eq. (22) as a plausible definition which at the very least yields local quantities which provide a good way to visualize the structure of the scattering states at the Fermi energy. These same comments apply as well to the quantum phase-space distribution functions, which we discuss now.

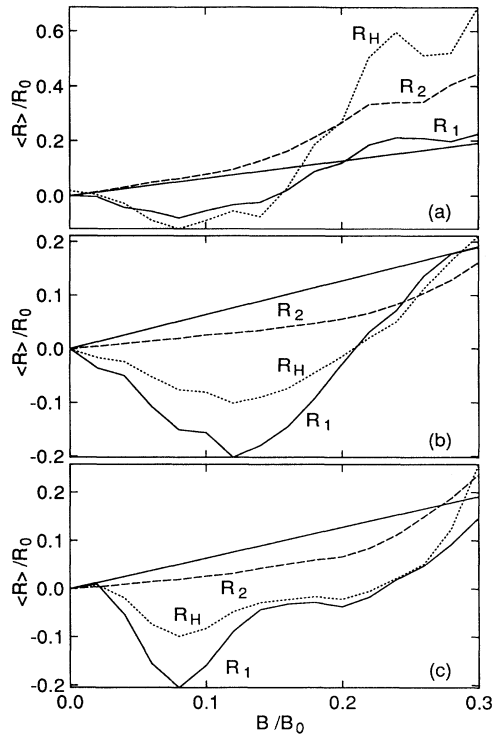

FIG. 26. Quantum resistances to analyze asymmetry vs magnitude effects in the Hall resistance for three structures: (a) R/W=4 four-disk structure, (b) gradually widened structure, and (c) $n=4$ soft-wall structure. R_1 (solid) uses the asymmetry from the rounded junction with the magnitude from the square junction, R_2 (dashed) is the opposite, the true Hall resistance is the dotted line, and the 2D result is the fine solid line. Suppression of asymmetry dominates in the four-disk structure (R_1 is a better match to R_H) but both R_1 and R_2 play a role in the other two structures. Asymmetry effects appear to be essential, but stable suppression of R_H is aided by the magnitude effects. $R_0 = (h/e^2)(\pi/k_F W)(mv_F/\hbar k_F)$, $B_0 = mcv_F/eW$.

A. Quantum phase-space distribution functions

$W(\mathbf{x},\mathbf{p})$ and $H(\mathbf{x},\mathbf{p})$, the Wigner and the Husimi distributions, respectively, are quantum-mechanical constructions which attempt to mimic as much as possible the properties of the distribution function $f(\mathbf{x},\mathbf{p})$ of the classical Boltzmann transport problem.[21] $f(\mathbf{x},\mathbf{p})$ answers the question of how many electrons are moving with momentum between $\mathbf{p}$ and $\mathbf{p}+\Delta\mathbf{p}$ at positions between $\mathbf{x}$ and $\mathbf{x}+\Delta\mathbf{x}$, which is very useful in understanding the details of classical transport in a complicated situation. $f(\mathbf{x},\mathbf{p})$ satisfies some moment conditions relating it to the charge density and current density:

$$e\int f(\mathbf{x},\mathbf{p})d\mathbf{p} = n(\mathbf{x}) \ ,$$
$$\frac{e}{m}\int \mathbf{p}f(\mathbf{x},\mathbf{p})d\mathbf{p} = \mathbf{j}(\mathbf{x}) \ . \tag{23}$$

In quantum mechanics, $\mathbf{x}$ and $\mathbf{p}$ are noncommuting variables, so it is not possible to simultaneously specify their values for a transport electron. However, it is (almost) possible to construct a *distribution* for such electrons, and this is what the Wigner and Husimi functions do. The Wigner function for a wave function ψ is

$$W(\mathbf{x},\mathbf{p}) = \int \exp\left[i\left(\mathbf{p}\cdot\mathbf{x}'/\hbar + e/\hbar c\int_{\mathbf{x}-1/2\mathbf{x}'}^{\mathbf{x}+1/2\mathbf{x}'}\mathbf{A}(\mathbf{x}'')\cdot d\mathbf{x}''\right)\right]\psi^*(\mathbf{x}+1/2\mathbf{x}')\psi(\mathbf{x}-1/2\mathbf{x}')d\mathbf{x}' \ . \tag{24}$$

This is given in a gauge-invariant form, which is not often found in the standard references.[69] The line integral over the vector potential $\mathbf{A}$ can be taken over any path between $\mathbf{x}-1/2\mathbf{x}'$ and $\mathbf{x}+1/2\mathbf{x}'$, but the straight path would be conventional. (In our numerical calculations, we Taylor-expand $\mathbf{A}$ about the point $\mathbf{x}$ and keep only the zeroth-order term in line integral. This is no longer exactly gauge invariant, but it is a very good approximation for our purposes.)

The Wigner function has several important properties in common with the classical distribution function. They satisfy the same moment conditions [Eq. (23)]. In some (very delicate) limit, which may be referred to as "$\hbar \to 0$" the Wigner function goes over to a classical distribution function.[69,70] As we will see below, in a very practical sense the same kind of intuitive information can be gleaned from the Wigner function as from the classical distribution function.

The Wigner function has several undesirable features as well. In general, it is not positive everywhere, so it cannot be directly interpreted as a probability measure. Associated with this is the fact that it also tends to have "ghost" features: structure in phase space which goes away in the classical limit, and requires careful interpretation in the quantum problem. We will point out some examples of ghost structures below.

The Husimi function H(x,p) cures some of the problems of the Wigner function. It is defined as the Wigner function, broadened by a minimum-uncertainty Gaussian function in phase space:

$$H(\mathbf{x},\mathbf{p}) = \int (1/\pi\hbar)e^{-(\mathbf{x}-\mathbf{x}')^2/\alpha}e^{-\alpha(\mathbf{p}-\mathbf{p}')^2/\hbar^2} \times W(\mathbf{x}',\mathbf{p}')d\mathbf{x}'d\mathbf{p}' \ . \tag{25}$$

The parameter α, which apportions the uncertainty between position and momentum, may be taken to have any convenient value. One desirable property of the Husimi function is that $H(\mathbf{x},\mathbf{p}) \geq 0$, which follows from a rewriting of the expression for the Husimi function:[69]

$$H(\mathbf{x},\mathbf{p}) = \left(\frac{1}{2\pi\hbar}\right)\left|\int \phi^C_{\mathbf{x},\mathbf{p}}(\mathbf{x}')\psi^*(\mathbf{x}')d\mathbf{x}'\right|^2 ,$$
$$\phi^C_{\mathbf{x},\mathbf{p}}(\mathbf{x}') = (\pi\alpha)^{-1/4}e^{-(\mathbf{x}'-\mathbf{x})^2/2\alpha}\exp\left[i\left(\mathbf{p}\cdot\mathbf{x}'/\hbar + e/\hbar c\int_{\mathbf{x}}^{\mathbf{x}'}\mathbf{A}(\mathbf{x}'')\cdot d\mathbf{x}''\right)\right] \ . \tag{26}$$

Another advantage of the Husimi function is that it tends not to have the "ghost" structures mentioned above for the Wigner function, so that the classical interpretation of features in the Husimi function tends to be easier. On the other hand, H(x,p) fails to satisfy the moment identities of Eq. (23), although in the cases we are interested in the violation is reasonably small.

B. Results: Four-disk structure

With these tools in hand, we now proceed to present the results of numerical calculations of these local quantities for several ballistic-electron structures. Figure 27 shows the T=0 charge density and current density for the R/W=4 four-disk structure [shown in Fig. 16(b)]. The square-lattice scale of the calculation is quite fine, with about 20 lattice points across the width of the lead. This is a structure which exhibits collimation effects, with an accompanying substantial reduction of the Hall coefficient at low magnetic fields. The scattering states are taken to be incident from the "West" lead and the Fermi energy is chosen such that there are four modes occupied. [Hereafter, we refer to leads as North (N), South (S), East (E), and West (W).] $\mathbf{j}(\mathbf{x})$ and $n(\mathbf{x})$ have reflection symmetry because of the symmetry of the potential and because $B = 0$. Within the Landauer-Büttiker picture, these results correspond to the true transport current density and charge density for a situation where the chemical potential is raised in the W lead, and held at its equilibrium value in all the other leads. In this plot

of the current density and in all subsequent plots, the current streamlines are drawn so that an equal amount of current flows between every pair of streamlines, and between the bounding streamlines and the walls.

While some collimation effects are present in current density in part (b), most such "classical" effects are obscured by the large amount of spatial quantum interference structure. This manifests itself in the frequent, pseudorandom twists and turns of the current streamlines, in vortices in the current field, and in frequent, pseudorandom maxima and minima in the charge density. These features occur on the scale of the Fermi wavelength, which is about $\frac{1}{4}$ of the width of the leads in this case. Not surprisingly, these features change rapidly as the energy or magnetic field are varied, as for R_H and R_B.

Some structure which is more regular can be seen, for example, the bunching up of current density in the E lead, which continues in a regular fashion into the asymptotic region; this structure arises from interference between partial waves of the scattering states exiting in different outgoing modes. This sort of structure tends to persist up to higher temperatures, as we will see below.

The appearance of pseudorandom structure in the charge density and current density are reminiscent of effects which have been seen in previous studies of "quantum chaos." The more-or-less uniform overall amplitude of the density $n(\mathbf{x})$ in the scattering region is similar to the structure of "ergodic" states in closed systems as discussed by Heller.[71] The general semiclassical theory of eigenstates[70,71] predicts that occasionally, the eigenstate should show "scars"—enhanced amplitude of the state in the vicinity of the path of some closed classical particle orbit in the system. Berry's general analysis, although performed for a closed system, seems to be applicable to scattering problems as well. However, we have only rarely seen evidence of such scars in our calculation; when they do occur, the enhancement tends to be comparable to that seen in the charge density of Fig. 27 near the junction with the E lead. Further investigation is needed to determine whether the phenomenology of quantum chaos is applicable to our studies.

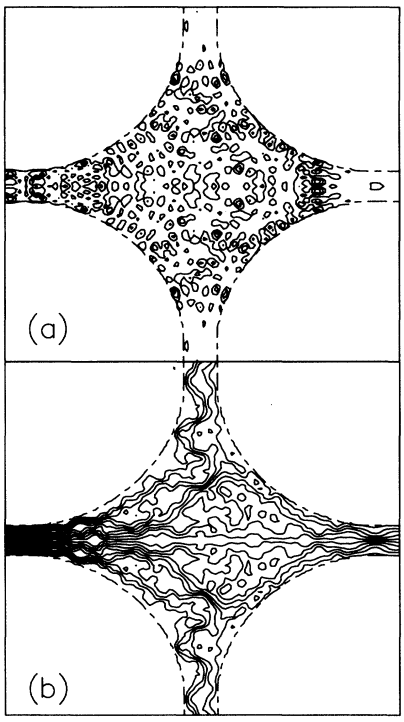

FIG. 27. Quantum-mechanical charge and current densities for scattering states at the Fermi energy in a hard-wall four-disk geometry [R/W=4, Fig. 16(b)]. Incoming waves enter from the left, $E_F = 18E_1$ (four modes occupied), k_BT=0, and B=0. (a) Equally spaced contours of the charge density. (b) Streamlines of the current density. The states have a high degree of spatial structure resulting from spatial wave interference. An equal amount of current flows between each pair of streamlines, and between the last streamlines and the walls.

Figures 28(a) and 28(b) show the same quantities as Fig. 27, but at a temperature corresponding to about one-tenth of the subband spacing. All other physical parameters are kept the same. We now need to do an energy integral as part of the trace of Eq. (21); we find that a 48-point approximation for this integral is adequate.

As we have seen earlier, this amount of energy averaging has a dramatic effect on the transport coefficients, removing most of the quantum interference structure and leaving quantities which vary smoothly with energy and magnetic field. Likewise, most of the spatial interference is removed from $\mathbf{j}(\mathbf{x})$ and $n(\mathbf{x})$, leaving only much more regular (and easily interpretable) features. Two types of features survive this degree of averaging.

The first is a spatial interference effect which is also wave mechanical in origin, has no classical analog, but survives because of its regularity. This shows up in the charge density of Fig. 28(a). $n(\mathbf{x})$ does *not* become uniform in space—it still has considerable variations in amplitude. However, these variations are no longer pseudorandom, but have a very regular, simple pattern. One sees a regular sequence of strips of maxima and minima on both the SE and NE walls inside the junction. These are in fact *standing waves*, which have a wavelength of about λ_F (the Fermi wavelength). They have a simple semiclassical interpretation: they indicate that carriers are undergoing near-normal reflection from these walls, and one thus obtains interference between the incident and reflected wave. Since this effect is not very energy dependent (λ_F varies only slightly in our energy window), it survives up to relatively high temperature. The reflection phenomenon does not produce a noticeable feature in the current density, except that the magnitude of the current is fairly small in this region, suggesting that the total current has canceling (i.e., counterpropagating) contributions. This standing wave is a valuable diagnostic of Hall resistance suppression, as we illustrate below.

The second kind of feature which survives our finite-temperature averaging is related to classical effects. The best example of this is the collimation effect seen in the current density of Fig. 28(b). As the current streamlines leave the W lead, they remain concentrated near the midline of the device and are attenuated near the walls; this

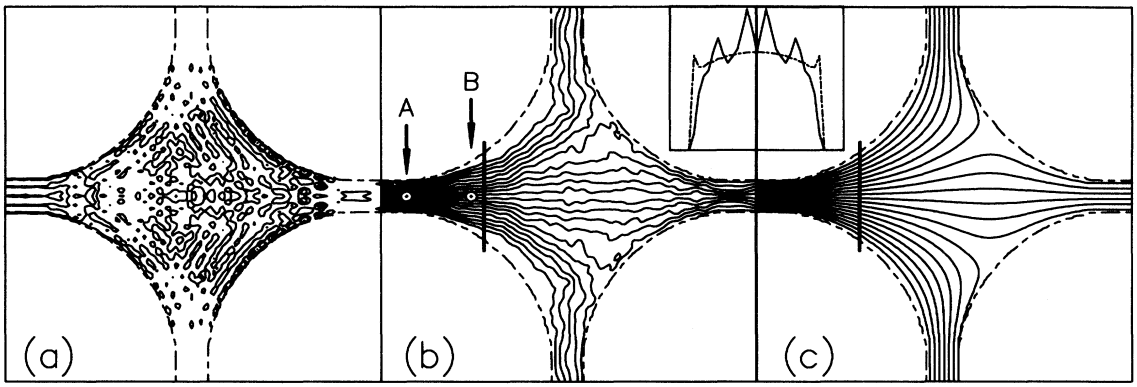

FIG. 28. Quantum and classical results for hard-wall four-disk geometry ($R/W = 4$) for zero magnetic field. (a) Equally spaced contours of charge density for scattering states thermally averaged around the Fermi energy ($E_F \simeq 18E_1$, $k_BT \simeq 0.6E_1$). There are standing-wave patterns on the lower right and upper right walls inside the junction, indicating the presence of some flux of counterpropagating electron waves reflecting off these walls. (b) The same as (a) for the current density streamlines. Note how temperature averaging has removed much of the spatial interference structure in both (a) and (b) compared with the zero-temperature results (Fig. 27). A and B indicate positions where the Wigner distribution function is shown in Fig. 29. (c) Current density streamlines for a classical sheet resistance in the same structure. The inset shows that the quantum current density (solid) is much more concentrated near the midline of the structure than the diffusive-classical current density (dashed), a result of collimation. Here $\mathbf{j}(\mathbf{x})$ is shown for the two cross sections indicated in parts (b) (solid) and (c) (dashed). The classical curve should be completely smooth; the small maxima it exhibits at the edges are a lattice effect.

is the classical effect of increasing the longitudinal momentum at the expense of transverse momentum via collisions with the walls. A good qualitative way to see that collimation is really taking place is to compare the quantum current distribution in Fig. 28(b) with the Drude (i.e., classical diffusive) current distribution in Fig. 28(c). This is simply obtained by solving the Laplace equation on the same quarter-circle cross. The inset shows the current-density profile across the cross sections indicated. The quantum ballistic current is clearly larger near the center and smaller at the walls.

Figure 29 establishes the collimation effect more quantitatively by showing the Wigner distribution for electrons in this part of the device. Obviously, since $W(\mathbf{x},\mathbf{p})$ lives in a four-dimensional phase space, it is not possible to exhibit the behavior of the entire function. Our choice is to fix $\mathbf{x}$ and give contour plots of W as a function of p_x and p_y.

We first show the Wigner function of electrons at the position marked A in Fig. 28(b); since this location is well into the input lead, we expect the momentum distribution to be characteristic of the incident modes. Classically, the incident electrons [recall Fig. 3(c)] would be uniformly distributed on the right-hand side of the Fermi surface (i.e., $p_x > 0$, corresponding to right-moving electrons); the total classical distribution would also have some reflected electrons on the left side of the Fermi sphere, which would be small in this ballistic structure.

Much of the quantum distribution is likewise concentrated near the right half of the Fermi surface. (The Fermi surface is almost a circle as indicated, but it is slightly distorted because of lattice dispersion effects.) The electrons on the Fermi surface have a substantial spread of momentum (much greater than k_BT smearing); this is a quantum-mechanical effect resulting from momentum uncertainty due to spatial confinement of electrons in the lead: this momentum spread Δp is roughly given by $W\Delta p \simeq \hbar$. This transverse confinement has another effect, which is to quantize the allowed transverse momenta: $k_\perp = n\pi/W$ (n is an integer). This is responsible for the four peaks indicated in the figure, which correspond to the four propagating modes at this energy. The other features inside the Fermi surface are interpretable as ghosts due to interference between different wave vectors on the Fermi surface; they can be either positive or negative depending on the relative phases of the Fermi-surface contributions.

Figure 29(b) shows $W(p_x,p_y)$ at the position marked B in Fig. 28(b), where we expect the electron distribution to show marked collimation. Indeed, all the Fermi-surface peaks slide around towards forward momentum, in a way which is consistent with the adiabatic-invariant idea,[26,27] which would predict that the peak positions would vary according to $k_\perp W(y) = \text{const}$, where $W(y)$ is the varying width of the lead as it enters the junction. Of course, it is clear from the figure that this is not precisely what is happening. In fact, the widening is becoming nonadiabatic at about this point in this structure; it is known[72] that there are additional diffraction effects when the widening is rapid, and these tend to merge the distinct peaks in the Wigner distribution together. There is additional structure in the Wigner function at point B, including somewhat increased reflected flux, which has no simple explanation.

C. Results: Adiabatic-rebound structure

We turn now to some calculations which relate more directly to anomalies in the Hall coefficient. Figure 30

shows calculations for the adiabatic-rebound structure: a junction with gradually widened leads and flattened corners. As shown in Fig. 14, this creates a much more pronounced anomaly in the low-field Hall resistance, with a substantial field range in which the sign of the Hall coefficient is opposite the conventional two-dimensional result. The Fermi energy is the same as in the figures above, and we show the results for the same temperature.

Figures 30(b) and 30(c) show the charge and current densities when the magnetic field is fixed such that the Hall coefficient has the maximum anomalous value (tick mark in the inset). The sign of the field is such that the classical Lorentz force sends electrons emerging from the W lead down towards the S lead; nevertheless, more electrons end up flowing into the N lead, as the current density in Fig. 30(c) shows. The charge density indicates that a rebound mechanism[22] is responsible for this reversal. Compare the standing-wave structure in $n(\mathbf{x})$ at finite B with the B=0 result [part (a)]. The standing wave disappears on the NE wall at finite B, and the

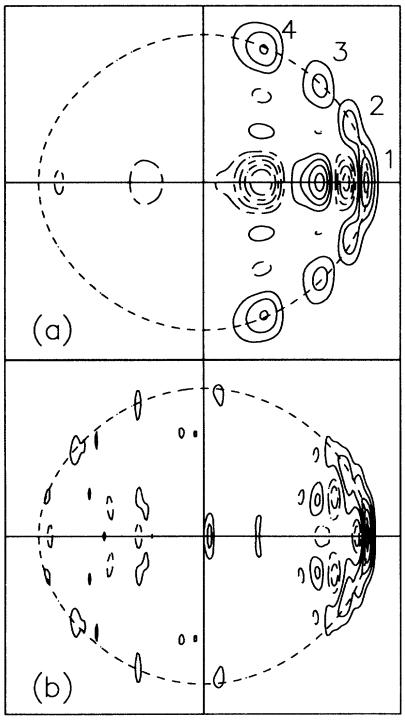

FIG. 29. The Wigner distribution as a function of wave vector for two different positions, for the device and conditions of Fig. 28. The Fermi surface is shown dashed. The contours are equally spaced (except that the zero contour is removed); positive contours are solid, negative contours dashed. (a) The injection distribution at position A in Fig. 28(b). The function is largely concentrated on the Fermi surface, as expected from semiclassical considerations. The four maxima labeled 1–4 correspond to the four incident modes. (b) The distribution in the widened part of the lead, at position B in Fig. 28(b). Note that the main weight of the Wigner function has moved towards the front of the Fermi surface; this is collimation, in which the transverse momentum decreases at the expense of the longitudinal momentum.

λ_F oscillation on the SE wall becomes much more pronounced. The classical interpretation which is implied is that electrons incident from the W lead have a high likelihood of being deflected down by the Lorentz force, missing the NE wall but striking the SE wall and being reflected into the N lead.

This picture is definitively confirmed by the Husimi distributions of Fig. 31. Parts (a) and (b) tell the same story about the incident distribution and its collimation as Fig. 29. As discussed above, the Husimi distribution, compared with the Wigner distribution, is slightly cleaner insofar as the distribution is everywhere positive and shows no ghost features; on the other hand, the features tend to show slightly poorer momentum resolution in $H(\mathbf{x},\mathbf{p})$. Note several small but important changes in Fig. 31(b) compared with the B=0 case. First, the collimated, forward-directed peak is directed slightly downwards by the Lorentz force. Second, a noticeable peak appears on the upper left of the Fermi surface. This signals that the collimated current density in Fig. 30(c) is beginning to deflect upwards as it emerges from the W lead. This effect becomes much more dramatic farther inside the junction.

Figure 31(c) shows $H(p_x,p_y)$ at position C in Fig. 30(b), in the middle of the standing-wave region. The collimated peak (labeled D for "direct") has evolved smoothly from part (b), but has been deflected downward much farther in its cyclotron orbit. A very large new feature (R for "rebound") has emerged, which has the obvious classical interpretation just described. It is evident that from this plot that the current at point C, which is (approximately) the first moment of this distribution, should be quite small since the two peaks almost cancel, and indeed this current is small in Fig. 30(c).

So, it is evident that even the very classical idea of rebounding electron paths has a very quantitative and obvious manifestation even in a fully quantum-mechanical transport calculation.

Finally, we show one example of the current density for different boundary conditions in the adiabatic-rebound structure: those appropriate for the bend resistance—current flowing in the W lead, out S, and zero in N and E—rather than for injection from one lead with the others grounded. Figure 32 shows that the current density for the bend resistance is dramatically different in the quantum ballistic case as compared with the diffusive case. Collimation has a large effect on the current distribution near both the injecting and collecting leads, and the rebound from the NE flat surface has produced a very unusual current density distribution in this quadrant.

VII. CONCLUSIONS

In this paper, we have concentrated on four issues in the theory of ballistic magnetotransport anomalies, as illustrated in the Hall resistance and bend resistance of a single junction. First, we emphasize that the geometry of the junction is crucial in both the classical and quantum results. A gradual widening of the wires or rounding of the junction corners is essential to produce quenching

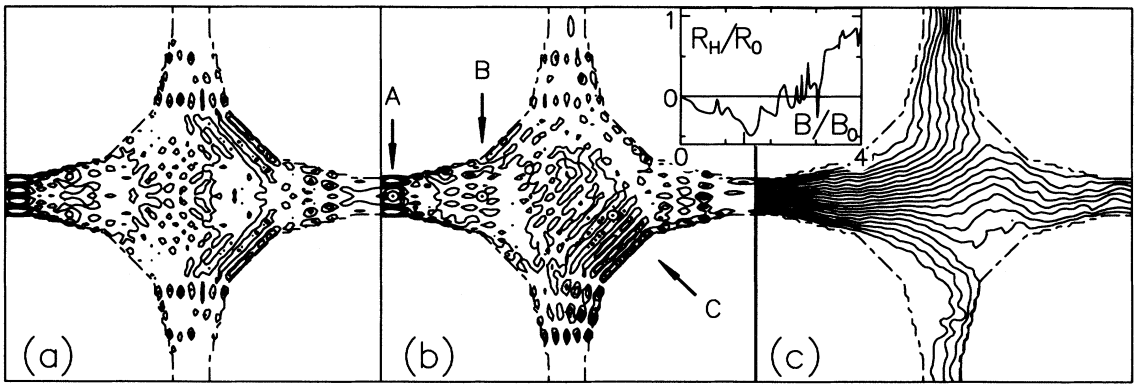

FIG. 30. Quantum results for the adiabatic-rebound geometry [Fig. 14(d)] for $E_F \simeq 18E_1$ and $k_BT \simeq 0.6E_1$. This structure shows a substantial reversal of the Hall resistance at small magnetic field. (a) Contours of charge density for zero magnetic field. Note the standing waves on the lower and upper right walls inside the junction, indicating a "rebound" effect. (b) Contours of charge density for magnetic field corresponding to maximum reversal of the Hall resistance (B/B_0=0.14—the dash in the inset showing the T=0 R_H). The sign of the field is such that the classical cyclotron orbits rotate clockwise. Note the strongly enhanced standing wave on the lower right wall inside the junction, indicating a strong rebound effect at this magnetic field. Figure 31 shows the Husimi function for positions A, B, and C. (c) Same as part (b) for the current density streamlines. The large flux transmitted into the upper lead compared with the lower lead indicates the reversal of the Hall coefficient. An initial collimation is also evident.

of the Hall resistance over a wide range of energies, as seen[10,11,22,23,31,32] in many of the experiments. The magnitude of the bend resistance and its decay as a function of magnetic field depends sensitively on the junction geometry. A soft-wall potential leads to enhanced quenching and substantial energy dependence of the traces. We reproduced the curious experimental behavior[31] of decreased quenching compared to the width of R_B as density increases, indicating indirectly that these experimental wires have rather soft walls.

Our second main result is that the classical and quantum results are qualitatively similar but quantitatively very different. Therefore, one should not expect quantitative agreement between experiments done in the few ($\approx$ 5) subband regime and the classical model. In addition to the obvious large quantum fluctuations (Fig. 1), we find substantial differences between classical resistances and *average* quantum resistances, defined by either a field-energy average or an impurity-energy average. Differences are, of course, expected in the limit of one or two subbands, but we find that they survive to surprisingly large energies—half a dozen subbands in many

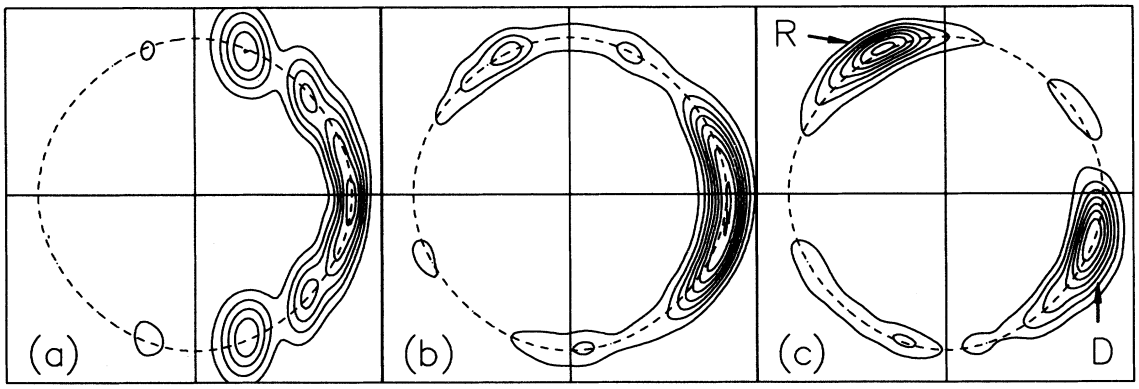

FIG. 31. The Husimi distribution as a function of wave vector for three different positions, for the device and conditions of Fig. 30(b). The Fermi surface is shown dashed. The contours are equally spaced; the function is positive everywhere, as discussed in the text. (a) The injection distribution at position A in Fig. 30(b). This is very similar to Fig. 29(a). (b) The distribution in the widened part of the lead, at position B in Fig. 30(b). This shows the same collimation phenomenon as Fig. 29(b). However, note that the distribution no longer has reflection symmetry, because of the magnetic field. The main weight of the distribution is pushed slightly below the axis because of the Lorentz force. (c) The distribution in the standing-wave region of the structure, position C in Fig. 30(b). The main weight of the distribution in part (b) has been pushed further down by the Lorentz force (the maximum labeled D for direct); a new maximum labeled R (for rebound) appears, resulting from electron waves reflected off the lower right wall inside the junction. This provides further detailed evidence for the importance of "rebound" trajectories in this structure.

cases and up to nine subbands in the concave cavity. The quantum results show substantially enhanced quenching, slower decay of the bend resistance as a function of field, strong variation on an energy scale less than the subband spacing, and periodic oscillations as a function of field in certain structures. Since many of the experiments have been done in the few-subband regime,[10,11,22,23,31] it is likely that the quantum enhancement of quenching has played a substantial role in these experimental results. We believe that the recent claim[2,32] that all observed ballistic junction effects have a classical basis has been overstated.

Third, we analyze the mechanism for quenching of the Hall resistance. From classical results as a function of trajectory length, we show that quenching and bend resistance are both short-trajectory effects. Long complex trajectories play no role in determining the qualitative features of the classical resistance in the structures we have studied and only a small role quantitatively, casting doubt on the "scrambling" mechanism suggested in Ref. 2. We analyze both the classical and quantum results in terms of both the asymmetry for turning left or right and the total magnitude for turning. The relative importance of these two effects depends on the geometry, ranging from a small magnitude effect in the four-disk junction to a large magnitude effect in the linearly graded structures. All of the trends in our results can be understood in terms of *collimation*, by which we mean structure in the momentum distribution of the injected electrons. The magnitude effect is clearly connected to collimation through the enhancement of the forward transmission at the expense of turning probability (the forward-enhancement mechanism). The suppression of left-right asymmetry is caused by "rebound" trajectories[22] in certain structures, where it is crucial that these trajectories are preferentially selected by collimation. Other less obvious trajectories may also contribute to suppression of left-right asymmetry or the magnitude effect.

Fourth, we discuss the local properties of a junction in the coherent regime. We find that the charge density and current density are highly structured because of quantum interference. Collimation is directly evident in the phase-space distribution (the Wigner and Husimi distributions) as is the importance of the "rebound" trajectories. Collimation affects both the current density—current is concentrated more towards the center than in the sheet resistance case used for comparison (particularly clear in the bend resistance boundary conditions of Fig. 32)—and the charge density—the standing wave caused by rebound trajectories. While the underlying classical features of ballistic transport are evident in these local properties, large quantum interference and quantum uncertainty effects are also clear.

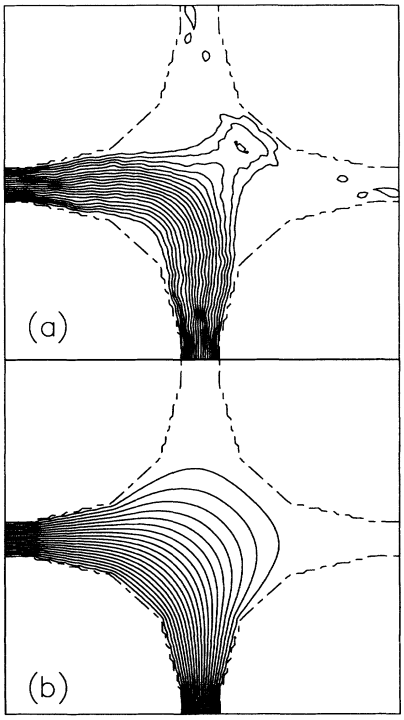

FIG. 32. Current density stream lines for bend resistance boundary conditions, for the adiabatic-rebound geometry. (a) Current density for $E_F \simeq 18E_1$ (four modes occupied), $k_BT \simeq 0.6E_1$, and B=0. Dashed lines indicate the hard walls of the structure. (b) Diffusive classical current calculated assuming a classical sheet resistance. Note that the quantum current density emerges from the lead much more forward-directed than the diffusive-classical current density; this is a consequence of collimation. An equal amount of current flows between each pair of stream lines, and between the last stream lines and the walls.

ACKNOWLEDGMENTS

We thank O. L. Alerhand, M. Büttiker, A. M. Chang, M. Gutzwiller, M. L. Roukes, A. Szafer, G. Timp, and J. Toner for many helpful discussions. Research at Yale University was supported in part by NSF Grant No. DMR-8658135, the IBM Corporation (R.A.J.), and the Alfred P. Sloan Foundation (A.D.S.).

APPENDIX A: MULTILEAD RECURSIVE GREEN-FUNCTION TECHNIQUE

In this appendix we describe the recursive Green-function technique used to find the transmission coefficients in the four-probe junctions discussed in this paper. The method is motivated by the two-probe case reviewed in the text in Sec. II A. The basic idea is to use Dyson's equation [Eq. (10)] with a judiciously chosen perturbation to piece together parts of the structure. In the two-probe case, one adds on one column of the lattice at a time, Eqs. (11) and (12). Here our approach will be to move down one lead towards the junction using the two-probe technique, then add on a cross strip (two leads), and then continue in the fourth lead moving away from the junction. This approach can be easily iterated to add on more than one cross strip and hence to consider six- or eight-probe structures.[21,73] We describe the technique for structures in which all four leads are different, as used in the impurity averaged traces of Sec. V. For structures

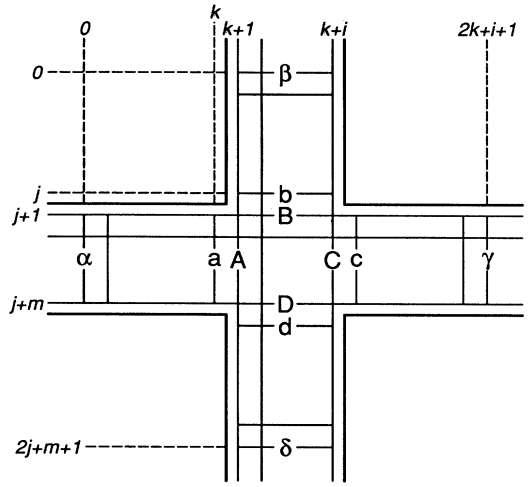

FIG. 33. Diagram of a typical junction showing the hard-wall frame (heavy lines), the lattice (fine lines), and the numbering and identification scheme used in explaining the multiprobe recursive Green function technique.

with four identical leads (Sec. IV), straightforward simplifications based on symmetry save considerable computer time.

To fix our notation, we show a generic four-probe junction in Fig. 33. The heavy lines are the hard walls of the structure, and the fine lines show the lattice. (For the soft-wall cases, the hard walls shown are the "frame" in which the potential-energy surface varies.) The sites are numbered by row (0 to $2j+m+1$) and column (0 to $2k+i+1$) as shown. We will refer to several special sets of sites by the letters a–d, A–D, and α–δ. For example, A consists of the sites in column $k+1$ and rows $j+1$ to $j+m$, i.e., coordinates $([j+1, j+m], k+1)$. Likewise, the coordinates for β are $(0, [k+1, k+i])$ and those for B are $(j+1, [k+1, k+i])$. The arguments for the Green functions will refer either to column numbers as in the main text (lower-case italic letters) or to these special sets of sites.

The discussion of our technique divides naturally into three parts: (1) the recursion along the horizontal strip before the cross strip (columns 1 to k), (2) the addition of the cross strip to the horizontal half strip (up to column $k+i$) and subsequent recursion out probe 3 (up to column $2k+i+1$), and (3) the calculation of the appropriate elements of the Green function of the cross strip.

1. Two-probe recursion

We use the two-probe recursion technique for the horizontal strip for columns $n < k$ and $n > k+i$. In order to calculate the full scattering matrix, one needs several recursive relations in addition to those in the text, Eqs. (11) and (12). In particular, these equations provide only the reflection coefficient from the right; we need in addition both transmission coefficients and the reflection coefficient from the left. Consider the same Dyson equation as for Eq. (11), namely, let the unperturbed system be the left half-strip terminated at column n plus the disconnected column $n+1$, $\underline{G}_0 = \underline{G}^L_n + \underline{g}_{n+1}$, and let the perturbation be the hopping between columns n and $n+1$, $\underline{U} = \underline{U}(n, n+1) + \underline{U}(n+1, n)$. For the transmission coefficient, one takes matrix elements of Dyson's equation [Eq. (10)] between columns 0 and $n+1$ yielding

$$\underline{G}^L_{n+1}(0, n+1) = \underline{G}^L_n(0, n)\underline{U}(n, n+1)\underline{G}^L_{n+1}(n+1, n+1) . \tag{A1}$$

The recursion relation for $\underline{G}^L_{n+1}(n+1, n+1)$, Eq. (11), provides, then, a simple recursion relation for $\underline{G}^L_{n+1}(0, n+1)$; an analogous equation holds for $\underline{G}^L_{n+1}(n+1, 0)$. Similarly, taking matrix elements between columns 0 and 0, one finds

$$\underline{G}^L_{n+1}(0,0) = \underline{G}^L_n(0,0) + \underline{G}^L_{n+1}(0, n+1)\underline{U}(n+1, n)\underline{G}^L_n(n, 0) . \tag{A2}$$

Equations (A1) and (A2) are also valid for attaching the right half-strip after crossing the scattering region, as in Eq. (12), if one replaces $\underline{G}^L_{n+1}$ by the total Green function $\underline{G}$. Thus, these equations combined with those in the text, Eqs. (11) and (12), provide a method for recursive calculation of all the elements of the Green function needed to determine the scattering matrix in a two-probe geometry.

2. Addition of a cross strip

We assume for this section that one knows the Green function for the cross strip, columns $k+1$ to $k+i$ in Fig. 33, disconnected from the horizontal strip. We call this Green function $\underline{\mathcal{G}}$ and discuss how to calculate the required elements in Sec. 3 of this appendix once we know which elements are needed. The problem, then, is to find the Green function for the structure up through column $k+i$, $\underline{G}^L_{k+i}$, in terms of $\underline{\mathcal{G}}$ and $\underline{G}^L_k$. The appropriate perturbation to use, then, is the coupling between sites a and A: $\underline{U} = \underline{U}(\mathrm{a}, \mathrm{A}) + \underline{U}(\mathrm{A}, \mathrm{a})$.

To continue the recursion beyond the cross strip into probe 3, we will need to know $\underline{G}^L_{k+i}(\mathrm{C},\mathrm{C})$. Taking various matrix elements of Dyson's equation, one finds

$$\begin{aligned}
&\underline{G}^L_{k+i}(\mathrm{C},\mathrm{C}) = \underline{\mathcal{G}}(\mathrm{C},\mathrm{C}) + \underline{\mathcal{G}}(\mathrm{C},\mathrm{A})\underline{U}(\mathrm{A},\mathrm{a})\underline{G}^L_{k+i}(\mathrm{a},\mathrm{C}) ,\\
&\underline{G}^L_{k+i}(\mathrm{a},\mathrm{C}) = \underline{G}^L_k(\mathrm{a},\mathrm{a})\underline{U}(\mathrm{a},\mathrm{A})\underline{G}^L_{k+i}(\mathrm{A},\mathrm{C}) ,\\
&\underline{G}^L_{k+i}(\mathrm{A},\mathrm{C}) = [\underline{I} - \underline{\mathcal{G}}(\mathrm{A},\mathrm{A})\underline{U}(\mathrm{A},\mathrm{a})\underline{G}^L_k(\mathrm{a},\mathrm{a})\underline{U}(\mathrm{a},\mathrm{A})]^{-1}\\
&\quad\times\underline{\mathcal{G}}(\mathrm{A},\mathrm{C}) .
\end{aligned} \tag{A3}$$

This is the required expression for $\underline{G}^L_{k+i}(\mathrm{C},\mathrm{C})$ in terms of elements of $\underline{\mathcal{G}}$ and $\underline{G}^L_k$. Starting with $\underline{G}^L_{k+i}(\mathrm{C},\mathrm{C})$, one can use the method of Sec. 1 of this appendix to continue the recursion into lead 3.

In addition to this part of the Green function, we need the elements necessary for ultimately calculating the scattering matrix. Thus, formulas for elements of $\underline{G}^L_{k+i}$ between all combinations of the sites α, β, δ, and C are required. For combinations of the sites β, δ, and C,

the formulas are exactly analogous to Eq. (A3): simply replace the left-hand or right-hand argument C by the desired one. For elements involving sites α, the formulas are slightly modified, and we give two examples. First, for sites α and C,

$$\underline{G}^L_{k+i}(\alpha,\mathrm{C}) = \underline{G}^L_k(\alpha,\mathrm{a})\underline{U}(\mathrm{a},\mathrm{A})\underline{G}^L_{k+i}(\mathrm{A},\mathrm{C}) , \qquad \text{(A4)}$$

where $\underline{G}^L_{k+i}(\mathrm{A},\mathrm{C})$ is given in Eq. (A3). The right-hand argument can clearly be either β or δ in addition to C. Second, for sites α connected to themselves, the transcription $\underline{G}^L_k \leftrightarrow \underline{\mathcal{G}}$, a $\leftrightarrow$ A, and C $\leftrightarrow \alpha$ in Eq. (A3) yields a valid equation. Thus we have given formulas for all the required elements of $\underline{G}^L_{k+i}$.

3. Green function of the cross strip

In the last part, we assumed that the Green function of the disconnected cross strip $\underline{\mathcal{G}}$ was known; now we must state how to calculate the required elements of this Green function. Looking at the equation for attaching the cross strip, Eq. (A3), we see that all elements for combinations of sites β, δ, A, and C are needed. Our basic approach is to obtain these elements through recursion along the vertical strip from top to bottom; for notation we refer to the top part as the left half-strip. First, the elements involving combinations of sites β and δ can be obtained using the recursive formulas of Sec. 1 of this appendix and are therefore trivial.

Second, we consider elements involving combinations of sites β or δ with sites A or C. These elements could be easily obtained if one knew the diagonal elements of $\underline{\mathcal{G}}$ in the junction region: using row numbers to label elements of $\underline{\mathcal{G}}$ (sites β correspond to row 0), one obtains

$$\underline{\mathcal{G}}(0,j+n) = \underline{\mathcal{G}}^L_{j+n-1}(0,j+n-1)\underline{U}(j+n-1,j+n) \times \underline{\mathcal{G}}(j+n,j+n) , \qquad \text{(A5)}$$

where $n \le m$. $\underline{\mathcal{G}}(0,j+n)$ yields two required elements, one for each of $\underline{\mathcal{G}}(\beta,\mathrm{A})$ and $\underline{\mathcal{G}}(\beta,\mathrm{C})$. The diagonal elements of the full Green function $\underline{\mathcal{G}}$ can be obtained from Eq. (12) in the text if one knows the Green function for the right half-strip. Our method, then, is to do two recursive passes, one in the forward direction from row j to $j+m+1$ in which we store $\underline{\mathcal{G}}^L_{j+n}$ and one in the reverse direction between the same rows in which we calculate $\underline{\mathcal{G}}^R_{j+n}$ and hence $\underline{\mathcal{G}}(j+n,j+n)$ from Eq. (12). Equation (A5) and its analogue for row $2j+m+1$ instead of 0, then, gives $\underline{\mathcal{G}}$ between combinations of β or δ and A or C.

Finally, we must find the elements of $\underline{\mathcal{G}}$ between combinations of A and C. To do this we disconnect the square at the intersection of the two strips by breaking the b-B bonds and the d-D bonds (in addition to the a-A and c-C bonds). Call this Green function $\underline{G}'$ and suppose we know its elements between combinations of sites A or C and sites A, B, C, and D. Then, taking the perturbation to be the b-B and d-D bonds, one finds

$$\underline{\mathcal{G}}(\mathrm{A},\mathrm{A}) = \underline{G}'(\mathrm{A},\mathrm{A}) + \underline{G}'(\mathrm{A},\mathrm{B})\underline{U}(\mathrm{B},\mathrm{b})\underline{\mathcal{G}}(\mathrm{b},\mathrm{A}) + \underline{G}'(\mathrm{A},\mathrm{D})\underline{U}(\mathrm{D},\mathrm{d})\underline{\mathcal{G}}(\mathrm{d},\mathrm{A}) , \qquad \text{(A6)}$$

where either argument A can be replaced by C. The elements of $\underline{\mathcal{G}}$ that are required here can be found as in the last paragraph with b and d replacing β and δ, respectively. (These can, of course, be calculated at the same time.) To calculate the elements of $\underline{G}'$, we use very weak bonds (10^{-5} of the usual hopping matrix strength) to attach sites A and C of the square to perfect half-strips (constant cross section). For this (fictitious) horizontal strip, the methods of the last two paragraphs yield elements of $\underline{G}'$ between combinations of sites A or C with sites A, B, C, and D. The purpose of the weak bonding to perfect half-strips is to eliminate singularities in the Green function of the closed square without significantly affecting its typical values. Our results are not sensitive to the strength of these bonds for strengths in the range 10^{-4}–10^{-6}. $\underline{G}'$ calculated in this way yields the desired elements of $\underline{\mathcal{G}}$ through Eq. (A6).

In summary, then, our recursive multilead method consists of several series of recursions to calculate the Green function for elements of the junction followed by a pasting together of these various elements. First, we find the required elements of the Green function of the cross strip $\underline{\mathcal{G}}$ as outlined in Sec. 3 of this appendix. Second, we perform recursion down lead 1 towards the junction as described in Sec. 1 of this appendix. Third, we attach the cross strip to lead 1 using the method of Sec. 2 of this appendix. Finally, we continue the recursion in lead 3 moving away from the junction, basically as in Sec. 1 of this appendix. The scattering matrix $\underline{S}$ is obtained from the Green function by projecting onto the transverse wave functions as in Eq. (8). To check our method we calculate the diagonal elements of $\underline{S}\,\underline{S}^\dagger$ which should each be 1 by unitarity. In the results presented here, the average deviation from this expectation is $\approx 10^{-6}$ and the maximum deviation is $\approx 10^{-4}$. In terms of computational efficiency, this method scales in the same way as the two-probe recursion method, namely as the cube of the width times the length,[46] because only strip recursion is involved; the prefactor is larger because of both the additional passes in the junction region and the connecting of the various segments.

APPENDIX B: CLASSICAL INJECTION DISTRIBUTION FROM THE SEMICLASSICAL GREEN FUNCTION

In this appendix we obtain the expression for the classical transmission coefficients in a ballistic structure from the semiclassical approximation to the quantum Green function and discuss the limiting procedures that lead to the classical results. The starting point is the quantum-mechanical expression for the transmission amplitude in terms of the Green function Eq. (8) coupled with the well-known functional integral expression for the Green function. A stationary phase approximation to the functional integral yields an expression for the Green function in terms of a sum over classical trajectories.[52] For hard-wall leads of width W, Ref. 38 used this expression for the Green function to show that the semiclassical transmission amplitude between two modes a and b at the Fermi energy E is given by

$$t_{ba} = -\frac{(2\pi i\hbar)^{1/2}}{2W} \sum_{s(\bar{a},\bar{b})} \mathrm{sgn}(\bar{a})\mathrm{sgn}(\bar{b})\sqrt{\tilde{D}_s} \times \exp\left(\frac{i}{\hbar}\tilde{S}_s(\bar{b},\bar{a},E) - i\frac{\pi}{2}\nu_s\right) , \tag{B1}$$

where the sum is over trajectories s between two cross sections in the asymptotic regions of the incoming and outgoing leads, with energy E (or momentum $p = \sqrt{2mE}$) and the same transverse momentum as the transverse wave functions in the leads. The initial and final angles are therefore given by $\sin\theta = \bar{a}\pi/kW$ and $\sin\theta' = \bar{b}\pi/kW$ ($\bar{a} = \pm a$, $\bar{b} = \pm b$). Since $\bar{a}, \bar{b}$ are integers we see that the semiclassical approximation yields the intuitive result that only trajectories which enter and exit at discrete angles corresponding to the allowed quantized transverse momenta contribute to transmission. The preexponential factor is

$$\tilde{D} = \frac{1}{mv\cos\theta'}\left|\left(\frac{\partial y}{\partial\theta'}\right)_\theta\right| \tag{B2}$$

and the reduced action (virial) is given by

$$\tilde{S}(\bar{b},\bar{a},E) = S(y_0',y_0,E) + \hbar\pi\bar{a}y_0/W - \hbar\pi\bar{b}y_0'/W , \tag{B3}$$

where y_0 and y_0' are the transverse coordinates (measured from the edge of the wires) of the extreme points of the trajectory. The expression for the Maslov index ν can be found in Ref. 38 but will not be needed in what follows due to the approximations used. To simplify the notation, we are not writing in Eq. (B1) the lead indices, nor the irrelevant phase factor associated with the choice of the positions of the cross sections in the leads.

The transmission coefficient between two given leads is obtained by summing the magnitude squared of the transmission amplitudes for the occupied modes of these leads:

$$T = \sum_{a,b} |\, t_{ba}\,|^2 . \tag{B4}$$

Each term $|\, t_{ba}\,|^2$ is given by the sum over pairs of trajectories with the appropriate incoming and outgoing angles.

Since the momentum (which is a classical quantity) is related to the wave vector by $|p| = \hbar k$, the allowed angles become continuous as $\hbar \to 0$, or equivalently as $N \to \infty$ where $N = kW/\pi$ is the number of modes. Thus to obtain the classical transmission coefficient we first let the mode index in the leads become continuous,[74] convert the sums over a and b to integrals, and then change the integration variables from mode indices to initial and final angles:

$$T \approx \frac{\pi\hbar}{2W^2}\int_0^{kW/\pi} da \int_0^{kW/\pi} db \sum_s\sum_u (-1)^{n(s,u)}\sqrt{\tilde{D}_s\tilde{D}_u}\exp\left(\frac{i}{\hbar}(\tilde{S}_s - \tilde{S}_u) - i\frac{\pi}{2}(\nu_s - \nu_u)\right)$$
$$= \frac{k}{2\pi}\int_0^{\pi/2} d\theta\cos\theta\int_0^{\pi/2} d\theta' \sum_s\sum_u (-1)^{n(s,u)}\left|\left(\frac{\partial y_s}{\partial\theta'}\right)_\theta\left(\frac{\partial y_u}{\partial\theta'}\right)_\theta\right|^{1/2}\exp\left(\frac{i}{\hbar}(\tilde{S}_s - \tilde{S}_u) - i\frac{\pi}{2}(\nu_s - \nu_u)\right) . \tag{B5}$$

The sums are over classical trajectories s and u with initial and final angles $\bar{\theta} = \pm\theta$ and $\bar{\theta}' = \pm\theta'$; $n(s,u) = 0$ if the number of positive angles is even and $n(s,u) = 1$ otherwise.

Second, we neglect interference terms and keep only the terms of Eq. (B5) where the two trajectories s and u are identical, obtaining

$$T_{\mathrm{class}} = \frac{k}{2\pi}\int_0^{\pi/2} d\theta\cos\theta\int_0^{\pi/2} d\theta'\sum_s\left|\left(\frac{\partial y_s}{\partial\theta'}\right)_\theta\right|$$
$$= \frac{kW}{\pi}\int_0^W dy\, P(y)\int_{-\pi/2}^{\pi/2} d\theta\, P(\theta) f(y,\theta) , \tag{B6}$$

where $f(y,\theta) = 1$ if the trajectory with initial conditions y,θ exits by the chosen outgoing lead and $f(y,\theta) = 0$ otherwise. In the last step we have changed variables from θ' to y and introduced the spatial and angular distributions

$$P(y) = \frac{1}{W} , \quad P(\theta) = \tfrac{1}{2}\cos\theta . \tag{B7}$$

Notice that in Eq. (B6) the prefactor $kW/\pi = mvW/\hbar\pi$ is the number of modes in the incoming lead, so that T_{class} scales to infinity as $\hbar \to 0$. The occurrence of $\hbar$ in the expression for T_{class} results from the use of Fermi-Dirac statistics for the classical particles, as shown by the Boltzmann equation argument given in the text (Sec. II B) and in Ref. 21.

The Monte Carlo evaluation of the integral Eq. (B6) consists of generating random values of y and θ (or trajectories) with probability distributions given by Eq. (B7) and counting the number of trajectories which go between the two leads being considered. This is exactly the intuitive Monte Carlo method originally introduced by Beenakker and van Houten[2] and used here to produce our classical results.

An important question at this point is the relationship between the exact $T(k)$ and T_{class}. Intuitively one expects that in the limit $\hbar \to 0$ (which is equivalent to $k \to \infty$ for fixed W), distinct classical trajectories should have arbitrary and rapidly varying phases, allowing one to neglect the interference terms in Eq. (B5) as we have done in deriving T_{class}. To make a more precise mathematical statement we consider an energy (or k) average of Eq. (B5). Since $T_{\mathrm{class}} \propto k$ and scales to infinity as

$k \to \infty$ (or N), it is natural to scale the average by k^{-1} to yield a finite result in this limit.[75] This is particularly convenient when the scattering region is a billiard, for which the trajectories are independent of k and the action takes the simple form $S = \hbar k L$ where L is the path length. We define the average over wave vector by

$$\langle f(k) \rangle \equiv \lim_{q \to \infty} \frac{1}{q} \int_{k_c}^{k_c+q} f(k) dk \ , \tag{B8}$$

where we require the lower cutoff $N_c = k_c W/\pi \gg 1$ in order to make the continuum mode approximation valid. From Eq. (B5) the average of $T(k)/k$ is given by

$$\mathcal{T} \equiv \left\langle \frac{T(k)}{kW/\pi} \right\rangle = \frac{1}{2W} \int_0^{\pi/2} d\theta \cos\theta \int_0^{\pi/2} d\theta' \sum_s \sum_u (-1)^{n(s,u)} \left| \left(\frac{\partial y_s}{\partial \theta'} \right)_\theta \left(\frac{\partial y_u}{\partial \theta'} \right)_\theta \right|^{1/2} \exp\left(-i \frac{\pi}{2} (\nu_s - \nu_u) \right) \langle \exp\left[ik(\tilde{L}_s - \tilde{L}_u) \right] \rangle \ . \tag{B9}$$

In analogy with the reduced action, the reduced length $\tilde{L}_s$ is defined by $\tilde{L}_s = L_s + \sin\bar{\theta}_s y_{0,s} - \sin\bar{\theta}'_s y'_{0,s}$. The average over k gives a Kronecker delta and therefore $\tilde{L}_s = \tilde{L}_u$. Since the number of trajectories entering at angle θ and exiting at θ' is discrete, in the absence of exact symmetries between classical trajectories, the double sum over s and u becomes a single sum over s yielding the strictly diagonal approximation (SDA) of keeping only pairs of *identical* trajectories, Eq. (B6). Thus the quantum $T(k)$ converges to T_{class} when averaged in this way, once $N \gg 1$. Since the numerical energy-averaging results in the text were not obtained for $N \gg 1$, it is not surprising that significant discrepancies remain (see Secs. IV B and V B). Moreover, this argument does not imply that $T(N \to \infty) - T_{\text{class}} \to 0$ since we have neglected terms of order $1/N$ in $\mathcal{T}$ or order one in T. In fact we find numerically that the conductance fluctuations treated in Ref. 38 apparently persist to arbitrarily large k and remain of order unity;[53] so apparently $T(N \to \infty) - T_{\text{class}} \sim 1$ as one finds[62] for the universal conductance fluctuations.

Further interesting questions arise when exact symmetries are present, so that the condition $\tilde{L}_s = \tilde{L}_u$ pairs not only identical trajectories but also symmetry-related trajectories. We call this the quasidiagonal approximation (QDA) in contrast to the strict diagonal approximation (SDA) when only identical trajectories are paired. If, for example, we have mirror reflection symmetry along the direction of the wires (as we do for all the billiards considered in this paper), the condition $\tilde{L}_s = \tilde{L}_u$ for symmetric trajectories s and u implies that $\bar{\theta}_s = \bar{\theta}'_s$. Therefore the QDA gives an extra factor of 2 with respect to the SDA for the $\theta = \theta'$ contribution to the integral in Eq. (B9). Similarly, in the presence of time-reversal symmetry, the QDA gives an extra factor of 2 to the $\theta = \theta'$ contribution to the reflection coefficient. This is the ballistic analogue of the well-known weak-localization backscattering enhancement.[65] Although such symmetry effects are quite interesting, because they only affect diagonal contributions they enter in the total transmission or conductance at order unity; hence they may be neglected to leading order in calculating $\mathcal{T}$. Thus, although strictly speaking only the QDA can be obtained as the average of the quantum transmission coefficient for an infinite k window, in the limit $N \to \infty$ this gives the same prescription, Eq. (B6), as the SDA, that is, $T_{\text{class}} = N\mathcal{T}$.

The effects of the exact symmetries on the semiclassical transmission can be seen more dramatically before summing over modes. First, we consider the individual transmission amplitudes t_{ba}, Eq. (B1). If we consider two trajectories s and u related by mirror reflection symmetry, then $S_s - S_u = 0$ and the difference in reduced actions is $\tilde{S}_s - \tilde{S}_u = \hbar\pi(\bar{a}_s - \bar{b}_s)$. Hence if the modes a and b have different parity we have destructive interference and $t_{ba} = 0$, consistent with the parity selection rules. When the modes have the same parity we get constructive interference. Second, we consider the individual transmission intensities $|\, t_{ba} \,|^2$ and argue that the diagonal approximation is unphysical for this quantity. An immediate result of the behavior of the amplitudes is that the strict diagonal approximation violates parity rules for symmetric structures. Although this problem does not occur if one pairs all trajectories having the same action ($S_s = S_u$), even this approach has the unphysical feature of changing discontinuously under infinitesimal perturbations of a symmetric structure. Within this approximation, if we perturb a structure with mirror symmetry, $|\, t_{ba} \,|^2$ will jump from zero to a finite value for modes with different parity and be reduced by a factor of 2 for modes with the same parity, no matter how small the perturbation is. Thus, because of the parity constraints, we find that both of these naive diagonal approximations are unphysical for the transmission intensities between individual modes.

Turning our attention back to the total transmission summed over modes, Eq. (B4), we immediately conclude that the diagonal approximation is inapplicable in the one-mode limit, since in this case $T = |\, t_{11} \,|^2$. However, if we consider the opposite limit of a continuum number of modes, the extra factor of 2 from parity-allowed pairs exactly compensates the cancellation of parity-forbidden pairs in the coarse grain sum over modes, and we obtain again exactly the same result as the strict diagonal approximation, Eq. (B6). To summarize, we find that the

diagonal approximation to the total transmission, and hence the classical approximation for the conductance, is valid in the limit of a continuum of modes after an average over an infinite energy range and is certainly not valid in the extreme quantum limit.

APPENDIX C: SEMICLASSICAL LIMIT WITH SOFT WALLS

In this appendix we derive the classical transmission coefficients when there is soft-wall confinement in the leads. The calculation will be done in two steps, the first of which is to obtain the semiclassical transmission amplitude between two modes, analogous to Eq. (B1). From this we consider the classical limit and obtain the classical transmission coefficient for the soft-wall case, akin to Eq. (B6). The first step follows closely the procedures of Ref. 38, while the second step is an extension of Appendix B. The main difference between the hard- and soft-wall cases is that in the former we knew the exact transverse wave functions, while we will be using the WKB approximation for the soft-wall confinement.

An exact starting point for the transmission amplitude between modes a and b at the Fermi energy E is[7]

$$t_{ba} = -i\hbar(v_a v_b)^{1/2} \int dy' \int dy\, \chi_b^*(y')\chi_a(y) G(y', y, E) \ , \tag{C1}$$

where v_a (v_b) and χ_a (χ_b) are the longitudinal velocity and transverse wave function for the mode a (b). $E = \hbar^2 k_a^2/2m + \varepsilon_a = \hbar^2 k_b^2/2m + \varepsilon_b$, where the first term is the energy of the longitudinal motion, while ε_a (ε_b) is the eigenenergy of the transverse wave-function χ_a (χ_b) in the confining potential $U(y)$ of leads. In order to simplify the notation we are taking the same confining potential in both leads and we are not writing lead indices. G is the retarded Green function between points (x, y) on the incoming lead and (x', y') on the outgoing lead. We are not writing the irrelevant phase factor dependent on x, x', nor the dependence of the Green function on its longitudinal coordinates. We will maintain this convention of not writing dependences on x and x' since the transverse sections used to define the transmission amplitudes will be fixed.

To approximate t_{ba} we replace G by its semiclassical path integral expression[52]

$$G(y', y, E) = \frac{2\pi}{(2\pi i\hbar)^{3/2}} \sum_{s(y,y')} \sqrt{D_s} \exp\left(\frac{i}{\hbar} S_s(y', y, E) - i\frac{\pi}{2}\mu_s\right) \ , \tag{C2}$$

where S_s is the action integral along a *classical* path s at energy E, $D = (v' \cos\theta'/m)^{-1} \mid (\partial\theta/\partial y')_y \mid$, θ and θ' are the incoming and outgoing angles, and μ is the Maslov index[52] given by the number of constant-energy conjugate points. Consistently with the semiclassical form of the Green function, we will use the WKB approximation for the transverse wave function

$$\chi_a(y) = \frac{1}{\sqrt{T(\varepsilon_a)}} \frac{2\sqrt{m}}{\{2m[\varepsilon_a - U(y)]\}^{1/4}} \cos\left(\frac{1}{\hbar}\int_{y_1}^{y} dz \sqrt{2m[\varepsilon_a - U(z)]} - \frac{\pi}{4}\right) \ . \tag{C3}$$

The allowed energies ε_a are given by the WKB quantization condition

$$\int_{y_1}^{y_2} dz \sqrt{2m[\varepsilon_a - U(z)]} = (a + \tfrac{1}{2})\pi\hbar \ , \tag{C4}$$

where y_1 and y_2 are the classical turning points, $U(y_1) = U(y_2) = \varepsilon_a$. The normalization factor $T(\varepsilon_a)$ is the period of the classical orbit with energy ε_a

$$T(\varepsilon_a) = 2m \int_{y_1}^{y_2} \frac{dz}{\sqrt{2m[\varepsilon_a - U(z)]}} \ . \tag{C5}$$

Breaking up the cosine of the WKB transverse wave function into the sum of two exponentials, the integral over y in Eq. (C1) can be performed by use of the stationary-phase (SP) approximation, valid in the semiclassical limit. The SP condition for the first (second) term is

$$-\left(\frac{\partial S}{\partial y}\right)_{y'} = p_y = mv\sin\theta = \pm\sqrt{2m[\varepsilon_a - U(y)]} \ . \tag{C6}$$

That is, the incident transverse momentum of a contributing classical trajectory p_y equals the momentum at the initial point of the trajectory of a classical particle moving in the confining potential $U(y)$ with an energy ε_a. The incident longitudinal momentum of the classical trajectory is that of the propagating mode a, $\sqrt{2m(E - \varepsilon_a)}$. For convenience in the evaluation of the quadratic displacements around the SP point, we define for the first (second) term an effective angle

$$\varphi = \theta \mp \arcsin\left(\frac{\varepsilon_a - U(y)}{E - U(y)}\right)^{1/2} \pm \arcsin\sqrt{\varepsilon_a/E} \ . \tag{C7}$$

For trajectories satisfying the SP condition $\varphi = \pm\arcsin\sqrt{\varepsilon_a/E} \equiv \bar{\varphi}(\varepsilon_a)$. The SP integration over y then yields

$$t_{ba} = v_b^{1/2}\frac{1}{\sqrt{T(\varepsilon_a)}}\int dy' \chi_b^*(y') \sum_{s(\bar{\varphi},y')} \frac{1}{\{2m[\varepsilon_a - U(y_0)]\}^{1/4}}\sqrt{\bar{D}_s} \times \exp\left(\frac{i}{\hbar}S_s(y', y_0, E) + \frac{i}{\hbar}\mathrm{sgn}(\bar{\varphi})\int_{y_1}^{y_0} dz\sqrt{2m[\varepsilon_a - U(z)]} - i\frac{\pi}{4}\mathrm{sgn}(\bar{\varphi}) - i\frac{\pi}{2}\bar{\mu}_s\right) . \tag{C8}$$

The new prefactor is $\bar{D} = (v'\cos\theta'/m)^{-1} \mid (\partial y/\partial y')_{\varphi} \mid$. The new Maslov index $\bar{\mu}$ is given in terms of the original μ and the sign of the second derivative of the exponent at the SP point. Since we have in mind the diagonal approximation of the classical transmission coefficient the form of the Maslov indices is not important and we will not be writing explicit expressions for them.

The integration over y' in the exiting transverse section can also be carried out in the SP approximation. The SP condition is analogous (up to a minus sign) to Eq. (C6) and with an effective angle φ' defined as in Eq. (C7) the semiclassical transmission amplitude between modes a and b can be written as

$$t_{ba} = (2\pi\hbar)^{1/2}\frac{1}{\sqrt{T(\varepsilon_a)T(\varepsilon_b)}}\sum_{s(\bar{\varphi},\bar{\varphi}')}\left(\frac{1}{4m^2[\varepsilon_a - U(y_0)][\varepsilon_b - U(y_0')]}\right)^{1/4}\sqrt{\tilde{D}_s} \times \exp\left(\frac{i}{\hbar}\tilde{S}_s(\bar{\varphi}', \bar{\varphi}, E) - i\frac{\pi}{4}[\mathrm{sgn}(\bar{\varphi}) - \mathrm{sgn}(\bar{\varphi}')] - i\frac{\pi}{2}\nu_s\right) . \tag{C9}$$

The sum is over trajectories with fixed effective angles $\bar{\varphi}(\varepsilon_a)$ and $\bar{\varphi}'(\varepsilon_b)$. y_0, θ, and ε_a are related by the SP condition (C6) [or in the notation of Eq. (C7), $\varphi = \bar{\varphi}(\varepsilon_a)$], and an analogous relationship holds at the outgoing cross section. The reduced action (virial) is

$$\tilde{S}(\bar{\varphi}', \bar{\varphi}, E) = S(y_0', y_0, E) + \mathrm{sgn}(\bar{\varphi})\int_{y_1}^{y_0} dz\sqrt{2m[\varepsilon_a - U(z)]} - \mathrm{sgn}(\bar{\varphi}')\int_{y_1'}^{y_0'} dz\sqrt{2m[\varepsilon_b - U(z)]} \tag{C10}$$

and the new prefactor is

$$\tilde{D}_s = \frac{m}{v'\cos\theta'}\left|\left(\frac{\partial y}{\partial\varphi'}\right)_{\varphi}\right|_{\varphi=\bar{\varphi},\varphi'=\bar{\varphi}'} . \tag{C11}$$

The expression (C9) for the semiclassical amplitude is analogous to Eq. (B1), with the effective angles $\bar{\varphi}$ and $\bar{\varphi}'$ playing the role of the angles θ and θ' of the hard-wall case. The value of the effective angle for a contributing trajectory is determined by the transverse energy of the mode. As in Appendix B we obtain the classical transmission coefficient by neglecting off-diagonal terms in $\mid t_{ba} \mid^2$ and converting the sum over occupied modes into an integral. In term, this integral can be converted into an integral over transverse eigenenergies since the quantization condition (C4) implies that $d(\hbar a)/d\varepsilon_a = T(\varepsilon_a)/2\pi$. The classical transmission coefficient is then given by

$$T_{\mathrm{class}} = \frac{1}{2\pi\hbar}\int_0^E d\varepsilon_a \int_0^E d\varepsilon_b \sum_{s(\bar{\varphi},\bar{\varphi}')}\frac{\tilde{D}_s}{\sqrt{4m^2[\varepsilon_a - U(y)][(\varepsilon_b - U(y')]}} = \frac{2E^2}{\pi\hbar}\int_{-\pi/2}^{\pi/2} d\bar{\varphi}\cos\bar{\varphi}\sin\bar{\varphi}\int_{-\pi/2}^{\pi/2} d\bar{\varphi}'\cos\bar{\varphi}'\sin\bar{\varphi}'\sum_{s(\bar{\varphi},\bar{\varphi}')}\frac{\tilde{D}_s}{\sin\theta\sin\theta'\sqrt{4m^2[E - U(y)][E - U(y')]}} . \tag{C12}$$

In the last step we changed in each lead from the transverse eigenenergies to the effective angles by using the relationships $\sin\bar{\varphi} = \sqrt{\varepsilon_a/E}$, and $\sin\bar{\varphi}' = \sqrt{\varepsilon_b/E}$.

So far the partial derivatives in the prefactors D have been taken at fixed ε_a and ε_b (or $\bar{\varphi}$ and $\bar{\varphi}'$) and they incorporated the effect of the neighboring trajectories to a stationary one (for a given pair of incoming and outgoing modes). Now we are integrating over modes, and it is useful to express partial derivatives with respect to the effective angles $\bar{\varphi}$ and $\bar{\varphi}'$. For contributing (stationary) trajectories a fairly simple exercise in taking partial derivatives shows that

$$\left(\frac{\partial\bar{\varphi}'}{\partial y'}\right)_{\bar{\varphi}} = \frac{\sin\theta'\cos\theta'}{\sin\bar{\varphi}'\cos\bar{\varphi}'}\left(1 - \frac{U(y')}{E}\right)\left(\frac{\partial\varphi'}{\partial y'}\right)_{\varphi,\varepsilon_a,\varepsilon_b} \tag{C13}$$

Changing the integration variables from $(\bar{\varphi}, \bar{\varphi}')$ to (θ, y)

$$T_{\text{class}} = \frac{m v_F W_{\text{eff}}}{\pi \hbar} \int_{y_1(E)}^{y_2(E)} dy\, P(y) \int_{-\pi/2}^{\pi/2} d\theta\, P(\theta) f(y,\theta) \ . \tag{C14}$$

$f(y,\theta) = 1$ if the trajectory with initial conditions y, θ exits by the chosen outgoing lead and $f(y,\theta) = 0$ otherwise. v_F is the Fermi velocity at the middle of the wire $[v(y = 0)]$, $y_1(E)$ and $y_2(E)$ are the classical turning points at energy E, and the spatial and angular distributions are

$$\begin{aligned} P(y) &= \frac{1}{W_{\text{eff}}} \sqrt{1 - U(y)/E} \ , \\ P(\theta) &= \tfrac{1}{2} \cos\theta \ . \end{aligned} \tag{C15}$$

The effective width W_{eff} is defined by

$$W_{\text{eff}} = \int_{y_1(E)}^{y_2(E)} dy \sqrt{1 - U(y)/E} \tag{C16}$$

and corresponds to the width of a hard-wall lead that, at the Fermi energy E, has the same number of modes as in the present case. As in Eq. (B6) the prefactor of T_{class} is the number of occupied modes. The soft- and hard-wall cases have the same angular distribution $P(\theta)$ but differ in their spatial distribution $P(y)$.

[1] For reviews see *Nanostructure Physics and Fabrication*, edited by M. A. Reed and W. P. Kirk (Academic, New York, 1989) and C. W. J. Beenakker and H. van Houten in *Solid State Physics: Advances in Research and Applications*, edited by H. Ehrenreich and D. Turnbull (Academic, New York, 1991), Vol. 44, pp. 1–228.

[2] C. W. J. Beenakker and H. van Houten, Phys. Rev. Lett. **63**, 1857 (1989); in *Electronic Properties of Multilayers and Low-Dimensional Semiconductor Structures*, edited by J. M. Chamberlain, L. Eaves, and J. C. Portal (Plenum, New York, 1990).

[3] H. U. Baranger and A. D. Stone, Phys. Rev. Lett. **63**, 414 (1989).

[4] R. Landauer, IBM J. Res. Dev. **1**, 233 (1957); Z. Phys. B **68**, 217 (1987).

[5] M. Büttiker, Phys. Rev. Lett. **57**, 1761 (1986).

[6] E. N. Economou and C. M. Soukoulis, Phys. Rev. Lett. **46**, 618 (1981).

[7] D. S. Fisher and P. A. Lee, Phys. Rev. B **23**, 6851 (1981).

[8] A. D. Stone and A. Szafer, IBM J. Res. Dev. **32**, 384 (1988).

[9] H. U. Baranger and A. D. Stone, Phys. Rev. B **40**, 8169 (1989).

[10] M. L. Roukes, A. Scherer, S. J. Allen, Jr., H. G. Craighead, R. M. Ruthen, E. D. Beebe, and J. P. Harbison, Phys. Rev. Lett. **59**, 3011 (1987).

[11] C. J. B. Ford, T. J. Thornton, R. Newbury, M. Pepper, H. Ahmed, D. C. Peacock, D. A. Ritchie, J. E. F. Frost, and G. A. C. Jones, Phys. Rev. B **38**, 8518 (1988).

[12] G. Timp, H. U. Baranger, P. deVegvar, J. E. Cunningham, R. E. Howard, R. Behringer, and P. M. Mankiewich, Phys. Rev. Lett. **60**, 2081 (1988).

[13] C. W. J. Beenakker and H. van Houten, Phys. Rev. Lett. **60**, 2406 (1988).

[14] F. M. Peeters, Phys. Rev. Lett. **61**, 589 (1988).

[15] H. Akera and T. Ando, Phys. Rev. B **39**, 5508 (1989).

[16] D. G. Ravenhall, H. W. Wyld, and R. L. Schult, Phys. Rev. Lett. **62**, 1780 (1989); R. L. Schult, H. W. Wyld, and D. G. Ravenhall, Phys. Rev. B **41**, 12 760 (1990).

[17] G. Kirczenow, Solid State Commun. **71**, 469 (1989); Phys. Rev. Lett. **62**, 2993 (1989).

[18] H. U. Baranger and A. D. Stone, in *Science and Engineering of 1- and 0-Dimensional Semiconductors*, edited by S. P. Beaumont and C. M. Sotomayor-Torres (Plenum, New York, 1990), p. 121.

[19] In the calculation with weakly coupled voltage probes, the hopping matrix element connecting the voltage probes to the current channel is reduced by a factor of 100. In this situation, then, the current and voltage probes are not identical, so Eq. (3) is not valid and one must go back to Eq. (2) to derive an expression for R_H appropriate for this case.

[20] Y. Avishai and Y. B. Band, Phys. Rev. Lett. **62**, 2527 (1989).

[21] H. U. Baranger, Phys. Rev. B **42**, 11 479 (1990).

[22] C. J. B. Ford, S. Washburn, M. Büttiker, C. M. Knoedler, and J. M. Hong, Phys. Rev. Lett. **62**, 2724 (1989).

[23] A. M. Chang, T. Y. Chang, and H. U. Baranger, Phys. Rev. Lett. **63**, 1860 (1989).

[24] Y. Takagaki, K. Gamo, S. Namba, S. Ishida, S. Takaoka, K. Murase, K. Ishibashi, and Y. Aoyagi, Solid State Commun. **68**, 1051 (1988); Y. Takagaki, K. Gamo, S. Namba, S. Takaoka, K. Murase, and S. Ishida, *ibid.* **71**, 809 (1989); Y. Takagaki, Y. Kusumi, K. Gamo, K. Murase and S. Namba (unpublished); Y. Takagaki, K. Gamo, S. Namba, S. Takaoka, and K. Murase, Solid State Commun. **75**, 873 (1990).

[25] M. L. Roukes, T. J. Thornton, A. Scherer, and B. P. Van der Gaag, in *Electronic Properties of Multilayers and Low-Dimensional Structures*, edited by J. M. Chamberlain, L. Eaves, and J. C. Portal (Plenum, London, 1990).

[26] L. I. Glazman, G. B. Lesovik, D. E. Khmelnitskii, and R. I. Shekhter, Pis'ma Zh. Eksp. Teor. Fiz. **48**, 218 (1988) [JETP Lett. **48**, 238 (1988)].

[27] C. W. J. Beenakker and H. van Houten, Phys. Rev. B **39**, 10 445 (1989).

[28] Y. Imry, in *Nanostructure Physics and Fabrication*, edited by M. A. Reed and W. P. Kirk (Academic, New York, 1989), p. 379; A. Yacoby and Y. Imry, Phys. Rev. B **41**, 5341 (1990).

[29] L. W. Molenkamp, A. A. M. Staring, C. W. J. Beenakker, R. Eppenga, C. E. Timmering, J. G. Williamson, C. J. P. M. Harmans, and C. T. Foxon, Phys. Rev. B **41**, 1274 (1990).

[30] H. U. Baranger and A. D. Stone, Surf. Sci. **229**, 212 (1990).

[31] G. Timp, R. Behringer, S. Sampere, J. E. Cunningham, and R. E. Howard, in *Nanostructure Physics and Fabrication*, edited by M. A. Reed and W. P. Kirk (Academic, New York, 1989), p. 331.

[32] M. L. Roukes, A. Scherer, and B. P. Van der Gaag, Phys. Rev. Lett. **64**, 1154 (1990); M. L. Roukes, T. J. Thornton, A. Scherer, J. A. Simmons, B. P. Van der Gaag, and E. D. Beebe, in *Science and Engineering of 1- and 0-Dimensional Semiconductors* (Ref. 18).

[33] M. L. Roukes and O. L. Alerhand, Phys. Rev. Lett. **65**, 1651 (1990). While the main issues in this paper are the classical chaotic dynamics and the role of random scattering in the junction, the authors also address the nature of the bend resistance anomaly in the fully ballistic case. In this regard, Roukes and Alerhand argue that the peak in $R_B(B=0)$ near $R/W \approx 3$ results from a combination of *shadowing*, the lack of direct paths between adjacent leads for $R/W \geq 2.4$; *collimation*, the fact that particles which have scattered a few times in the injecting lead contribute substantially to the forward transmission; and *scrambling*, the increasing complexity of trajectories as R/W gets large. Shadowing suppresses the turning probability and hence enhances R_B; collimation enhances R_B by the simple forward-enhancement mechanism; and scrambling acts to equalize the transmission into the different leads, decreasing R_B. We point out that collimation may have other more subtle but equally important effects on the bend resistance in such structures, such as a suppression of the turning probability because the cone in momentum space of collimated injected particles does not overlap with the acceptance cone in momentum space of the collecting adjacent lead (Ref. 2). Such an effect would become important when the widening of the leads becomes sufficiently adiabatic which also occurs at about $R/W \approx 3$.

[34] R. Behringer, G. Timp, H. U. Baranger, and J. E. Cunningham, Phys. Rev. Lett. **66**, 930 (1991); see also T. Kakuta, Y. Takagaki, K. Gamo, S. Namba, S. Takaoka, and K. Murase, Phys. Rev. B **43**, 14 321 (1991).

[35] Q. Li and D. J. Thouless, Phys. Rev. Lett. **65**, 767 (1990).

[36] G. Kirczenow, Phys. Rev. B **38**, 10 958 (1988).

[37] O. Heinonen and P. L. Taylor, Phys. Rev. B **28**, 6119 (1983); **32**, 633 (1985).

[38] R. A. Jalabert, H. U. Baranger, and A. D. Stone, Phys. Rev. Lett. **65**, 2442 (1990).

[39] H. Akera and T. Ando, Phys. Rev. B **41**, 11 967 (1990).

[40] J. Sone and S. Ishizaka, in *Nanostructures: Fabrication and Physics (Extended Abstracts)*, edited by S. D. Berger, H. G. Craighead, D. Kern, and T. P. Smith III (Materials Research Society, Pittsburgh, 1990), p. 91.

[41] G. Kirczenow, Solid State Commun. **74**, 1051 (1990).

[42] L. Kouwenhoven (private communication); S. Washburn (private communication).

[43] See, for example, M. Büttiker, Phys. Rev. B **33**, 3020 (1986); S. Datta, *ibid.* **40**, 5830 (1989); S. Feng, Phys. Lett. A **143**, 400 (1990); A. Stern, Y. Aharonov, and Y. Imry, Phys. Rev. A **41**, 3436 (1990); G. Kirczenow (Ref. 41); J. L. D'Amato and H. M. Pastawski, Phys. Rev. B **41**, 7441 (1990); S. Hershfield, *ibid.* **43**, 11 586 (1991).

[44] C. S. Lent, Appl. Phys. Lett. **57**, 1678 (1990); T. Ohtsuki and Y. Ono, J. Phys. Soc. Jpn. **59**, 637 (1990), and references therein; M. J. McLennan and S. Datta, Phys. Rev. B **43**, 13 846 (1991).

[45] Y. Imry, in *Perspectives on Condensed Matter Physics*, edited by G. Grinstein and E. Mazenko (World Scientific, Singapore, 1986).

[46] P. A. Lee and D. S. Fisher, Phys. Rev. Lett. **47**, 882 (1981); D. J. Thouless and S. Kirkpatrick, J. Phys. C **14**, 235 (1981); A. MacKinnon, Z. Phys. B **59**, 385 (1985).

[47] A. Szafer, Ph.D. thesis, Yale University, 1990; A. M. Kriman, A. Szafer, A. D. Stone, and D. K. Ferry (unpublished).

[48] A. Messiah, *Quantum Mechanics* (Wiley, New York, 1958), pp. 825–828.

[49] J. M. Luttinger, Phys. Rev. **84**, 814 (1951); A. S. Alexandrov and H. Capellmann, Phys. Rev. Lett. **66**, 365 (1991).

[50] A. MacKinnon and B. Kramer, Phys. Rev. Lett. **47**, 1546 (1981).

[51] I. O. Kulik, A. N. Omel'yanchuk, and R. I. Shekter, Fiz. Nizk. Temp. **3**, 1543 (1977) [Sov. J. Low Temp. Phys. **3**, 740 (1977)]; A. G. M. Jansen, A. P. van Gelder, and P. Wyder, J. Phys. C **13**, 6073 (1980).

[52] M. C. Gutzwiller, *Chaos in Classical and Quantum Mechanics* (Springer-Verlag, Berlin, 1990), pp. 184–190 and 283–287; in *Chaos and Quantum Physics*, edited by M.-J. Giannoni, A. Voros, and J. Zinn-Justin (Elsevier, London, 1990), and references therein.

[53] R. A. Jalabert, Bull. Am. Phys. Soc. **36**, 743 (1991); H. U. Baranger, R. A. Jalabert, and A. D. Stone (unpublished).

[54] C. L. Kane, R. A. Serota, and P. A. Lee, Phys. Rev. B **37**, 6701 (1988).

[55] W. H. Press, B. P. Flannery, S. A. Teukolsky, and W. T. Vetterling, *Numerical Recipes* (Cambridge University Press, New York, 1990), pp. 70–73.

[56] The hard-wall classical simulations involve typically 10^6 particles for the resistance traces and 10^7 particles for the trajectory length analysis. The soft-wall classical simulations involve integrating a differential equation for each trajectory; we used half as many particles as in the hard-wall structures.

[57] C. W. J. Beenakker (private communication).

[58] See, e.g., *Chaos in Classical and Quantum Mechanics* (Ref. 52), pp. 149, 236, and 251.

[59] The scaling used in a soft-wall potential $U(y)$ is as follows. First, we retain the relation between our resistance scale and the experimental scale, namely, that one multiplies our scaled value by h/e^2 times the number of modes. Using the definition of Eq. (C16) for the effective width of the wire $W_{\rm eff}$, the resistance is scaled by $R_0 = (h/e^2)[\pi/k_F(0)W_{\rm eff}]$ (times $mv_F/\hbar k_F$ in the lattice case). Second, we require that the slope in the two-dimensional case be $2/\pi$. This is accomplished by using $W_{\rm eff}$ in the magnetic field scale, $B_0 = mcv_F(0)/eW_{\rm eff}$.

[60] For a nonzero magnetic field, the symmetry of the junction is essential in showing this result.

[61] In order to reconcile our view that the ballistic anomalies are caused by short paths with the data of Roukes and coworkers in Ref. 32, we suggest the following interpretation of their data. (1) Guiding of the particles around the corner at high magnetic field is less sensitive to disorder since it does not depend on collimation. Only backscattering degrades guiding; hence it is not surprising that guiding is less sensitive to disorder than quenching which depends on collimation and is sensitive to forward scattering. The greater sensitivity of quenching to disorder in no way implies that longer trajectories cause this effect than cause guiding. (2) The flared junction collimates only marginally. Thus R_H is very sensitive to disorder and only shows quenching at the highest density when the mean free path is largest. R_B decays as disorder increases, consistent with its ballistic origin. The enhancement of R_B substantially above the square-corner value indicates that some collimation is present, and the fact that R_B is substantial even when quenching has vanished is consistent with our results in Fig. 22. (3) Col-

limation is better established in the grossly flared junction because of the greater widening. Thus, a small region of inversion insensitive to density is present in R_H. R_B is sensitive to the density in this region which suggests that longer trajectories contribute to R_B than to R_H, as stated by Roukes and co-workers and in agreement with our trajectory length analysis in Fig. 10 (note that these trajectories are still short in terms of scrambling). (4) The structure in R_H for the straight junction is presumably caused by a completely different mechanism. A possibly related effect occurs in the quantum calculation of the concave cavity (Fig. 18) in which interference effects in the cavity are the cause. A small potential well in the junction region, enhanced perhaps by impurity effects, may be sufficient to cause this type of effect.

[62] P. A. Lee, A. D. Stone, and H. Fukuyama, Phys. Rev. B **35**, 1039 (1987), and references therein.

[63] The parameter values for the quantum calculations are as follows. (1) For the linearly widened and four-disk structures, $W = 18$ sites for which $E_1/V = 0.03$. The results for up to 10 subbands mentioned in the text use $W = 24$ sites. (2) For the concave cavity, $W = 24$ for which $E_1/V = 0.017$. (3) For the soft-wall structures, $W = 39$ in the junction at the maximum energy which corresponds to the threshold for the sixth or seventh mode. Writing $U = a_n x^n y^n / W^{2n}$, we use $a_2 = 29$, $a_4 = 430$, and $a_6 = 7700$ and match onto a y^n cross section at $x = W$. For these values, $E_1(n = 2) = 0.14$, $E_1(n = 4) = 0.062$, and $E_1(n = 6) = 0.046$. The widening of the wires is about a factor of 2 for the maximum energy used. Because the calculations are performed on a lattice, the dispersion relation is neither parabolic nor isotropic. The nonparabolicity is easily accounted for by distinguishing between $\hbar k_F$ and $m v_F$ in scaling the data. In contrast, distortion of the Fermi circle leads to preferential propagation in certain directions and must be avoided; for instance, a ballistic bend resistance of the wrong sign can occur. Our calculations are done for $k_x a < 1.4$ and $E_F/V < -2.4$ for which the maximum deviation of k_F (v_F) from the mean is 3% (7%).

[64] There is some energy dependence to the value of f: f decreases as the energy increases. This presumably occurs because faster particles see a less adiabatic potential, as argued in the Introduction. The range of f for our structures is approximately ± 0.05.

[55] For reviews see G. Bergmann, Phys. Rep. **107**, 1 (1984) and P. A. Lee and T. V. Ramakrishnan, Rev. Mod. Phys. **57**, 287 (1985).

[66] While the calculation in Appendix B is carried out for zero magnetic field, it can easily be generalized to include a magnetic field in the scattering region combined with the $B = 0$ injection conditions. Because of the $B = 0$ injection conditions, the continuum mode limit is the same as in Appendix B. If one fixes B/B_0 as the average over k, Eq. (B9), is performed, the paths which contribute to the semiclassical sum are independent of k, and one finds that the reduced action plus a term related to the enclosed area (see Ref. 38) must be equal for two paths to interfere. Because the sum over paths is discrete, as before, this condition is satisfied only if the two paths are the same, neglecting terms of order $1/N$ from exact symmetries. Thus, for fixed B/B_0, the simple classical expression is recovered for a continuum of modes and after an average over an infinite energy window.

[67] The mean free path is calculated numerically for a strip with a narrow disordered region through the Born approximation as in Ref. 21. For the values given here, the strip width is 36 sites, which corresponds to $3W$ for the $R/W = 4$ structure, $2W$ for the gradually widened structure, and twice the classical width at the highest energy for the soft-wall structure. (Note that L_D, the direct length, is approximately the same in these three structures.) The mean free path varies substantially with energy, by as much as a factor of 2; the values given result from averaging over energies for which 6–13 modes are contributing ($[-3.72, -2.72]$ in units of the hopping matrix element). In narrower strips 18 sites wide, the averaged mean free path is nearly the same (within 5%) but the energy variation is stronger.

[68] See, e.g., M. Büttiker, Phys. Rev. Lett. **65**, 2901 (1990).

[69] M. Hillery, R. F. O'Connell, M. O. Scully, and E. P. Wigner, Phys. Rep. **106**, 121 (1984).

[70] M. V. Berry, Proc. R. Soc. London Ser. A **423**, 219 (1989).

[71] E. J. Heller, Phys. Rev. Lett. **53**, 1515 (1984).

[72] A. Szafer and A. D. Stone, Phys. Rev. Lett. **62**, 300 (1989).

[73] H. U. Baranger, A. D. Stone, and D. P. DiVincenzo, Phys. Rev. B **37**, 6521 (1988).

[74] The continuum mode approximation is good up to order $1/N$. This can be easily seen from the semiclassical approximation to the real space form of the conductance (Refs. 9 and 53). This approach provides an alternative way to discuss the limiting procedures leading to the classical results.

[75] J.H. Hannay, in *Chaotic Behavior in Quantum Systems: Theory and Applications*, edited by G. Casati (Plenum, New York, 1983) p. 141.